HARVARD UNIVERSITY
Graduate School of Arts and Sciences

DISSERTATION ACCEPTANCE CERTIFICATE

The undersigned, appointed by the

Department of Physics

have examined a dissertation entitled

Theoretical Studies of Growth Processes and Electronic
   Properties of Nanostructures on Surfaces

presented by

Yina Mo

candidate for the degree of Doctor of Philosophy and hereby
certify that it is worthy of acceptance.

Signature _____

Typed name: Professor Efthimios Kaxiras, Chair

Signature _____

Typed name: Professor David Nelson

Signature _____

Typed name: Professor Michael Aziz

Date: May 18, 2007

Theoretical Studies of Growth Processes and Electronic Properties of Nanostructures on Surfaces

A dissertation presented by

Yina Mo

to

The Department of Physics
in partial fulfillment of the requirements
for the Degree of
Doctor of Philosophy
in the subject of

Physics

Harvard University
Cambridge, Massachusetts
May 2007

UMI Number: 3265045

INFORMATION TO USERS

The quality of this reproduction is dependent upon the quality of the copy
submitted. Broken or indistinct print, colored or poor quality illustrations and
photographs, print bleed-through, substandard margins, and improper
alignment can adversely affect reproduction.
    In the unlikely event that the author did not send a complete manuscript
and there are missing pages, these will be noted. Also, if unauthorized
copyright material had to be removed, a note will indicate the deletion.

UMI®

UMI Microform 3265045

Copyright 2007 by ProQuest Information and Learning Company.

All rights reserved. This microform edition is protected against

unauthorized copying under Title 17, United States Code.

ProQuest Information and Learning Company
300 North Zeeb Road
P.O. Box 1346
Ann Arbor, MI 48106-1346

Thesis advisor

Author

Efthimios Kaxiras

Yina Mo

Theoretical Studies of Growth Processes and Electronic Properties of Nanostructures on Surfaces

Abstract

Low dimensional nanostructures have been of particular interest because of their potential applications in both theoretical studies and industrial use. Although great efforts have been put into obtaining better understanding of the formation and properties of these materials, many questions still remain unanswered.

This thesis work has focused on theoretical studies of 1) the growth processes of magnetic nanowires on transition-metal surfaces, 2) the dynamics of pentacene thin-film growth and island structures on inert surfaces, and 3) our proposal of a new type of semiconducting nanotube.

In the first study, we elucidated a novel and intriguing kinetic pathway for the formation of Fe nanowires on the upper edge of a monatomic-layer-high step on Cu(111) using first-principles calculations. The identification of a hidden fundamental Fe basal line within the Cu steps prior to the formation of the apparent upper step edge Fe wire produces a totally different view of step-decorating wire structures and offers new possibilities for the study of the properties of these wires. Subsequent experiments with scanning tunneling microscopy unambiguously established the essential role of embedded Fe atoms as precursors to monatomic wire growth. A more general study of adatom behavior near transition-metal step edges illustrated a systematic trend in the adatom energetics and kinetics, resulted from the electronic

interactions between the adatom and the surfaces. This work opens the possibility of controlled manufacturing of one-dimensional nanowires. In the second study, we investigated pentacene thin-films on H-diamond, H-silica and OH-silica surfaces via force field molecular dynamics simulations. Pentacene island structures on these surfaces were identified and found to have a 90-degree rotation relative to the structure proposed by some experimental groups. Our work may facilitate the design and control of experimental pentacene thin-film growth, and thus the development of organic thin-film transistors. Finally, in our third study, we proposed a new type of structurally simple and energetically stable cyanide transition metal nanotube, based on the planar structure of $M(CN)2$, (M = Ni, Pd, Pt). These nanotubes have semiconducting character with large band gaps (2 - 3 eV), which are insensitive to the chirality and diameter. We have investigated the energetic, electronic, and mechanical properties of these materials in both planar and tubular forms through first-principles density functional calculations. These calculations reveal interesting multi-center bonding features that should lead to preferential growth of tubes of a particular chirality. The unique features of these nanotubes should make them capable of being mass-produced, which is one of the most significant shortcomings of semiconducting carbon nanotubes.

Contents

List of Figures

List of Tables

Citations to previously published work

1. *Semiconducting cyanide-transition-metal nanotubes*

   Y. Mo, and E. Kaxiras, accepted to Small (2007).

2. *Formation of monatomic Fe chains on vicinal Cu(111) surfaces: An atomistic view*

   J. Guo, Y. Mo, E. Kaxiras, Z. Zhang, and H. H. Weitering, Phys. Rev. B **73**, 193405 (2006).

3. *Kinetic pathway for the formation of Fe nanowires on stepped Cu(111) surfaces*

   Y. Mo, E. Kaxiras, and Z. Zhang, Phys. Rev. Lett. **94**, 155503 (2005).

4. *Sulfur point defects in crystalline and amorphous silicon*

   Y. Mo, M. Z. Bazant, and E. Kaxiras, Phys. Rev. B **70**, 205210 (2004).

5. *Step-edge barriers and nanowire growth on transition-metal surfaces*

   Y. Mo, E. Kaxiras, and Z. Zhang. Ready to submit.

6. *Phases of pentacene monolayers on H-saturated diamond and silica surfaces*

   Y. Mo, P. Maragakis and E. Kaxiras. In preparation.

Acknowledgments

First of all, I would like to thank my advisor Prof. Efthimios Kaxiras for taking me as his student and providing me with guidance. He led me into the field of computational physics and showed me the wonderland of physics. He is always patient with me and supports me with encouragement when I run into difficulties in my research. He is also someone I can talk to about life. Communication between us has always been built on mutual respect. I like him as a person and respect him professionally. I feel especially fortunate to have him as my advisor.

Secondly, I would like to thank my collaborator Dr. Zhenyu Zhang at Oak Ridge National Laboratory for guidance on two of my research projects. Zhenyu is an expert on surface science and introduced me into this field. I am impressed with his enthusiasm and knowledge. Zhenyu is a wonderful person and is a "big" friend to all of us Chinese students.

Thirdly, I would like to thank Prof. Aziz and Prof. Nelson for accepting the burden of serving on my committee.

I would also like to thank all the talented people around me that helped me with my research in numerous ways. The discussions I had with Prof. Gang Lu in the early days when I joined the group helped me dive into the field quickly. Prof. Wenguang Zhu technically supported the whole group. He is always available for questions. Discussions with his was always inspiring. Dr. Paul Maragakis introduced me to force field simulations, a field I was very interested in but otherwise would not be able to get into. Dr. Maria Fyta is always warm and helpful. She is not only a colleague but also a friend. Dr. Li Huang, Dr. Sheng Meng, and Dr. Weili Wang are coworkers that have made the life in office much more enjoyable.

Acknowledgments

Outside of physics, I am lucky to have Lan Hua, Christine Wang, and Dilini Pinnaduw as my best friends. Lan has made a mental home in New York for me and hosted and refreshed me every time I was out of energy. Christine is courageous and warm. With her, I have explored the life in Boston. Dilini was always there when I needed her. Together they made up the happy time of my Ph.D. life. I would always appreciate their friendship. I also thank Lars Grant for helping me prepare for my oral examination and listening to my boring lectures on Solid State Physics . Itay Yavin made the claim to be my brother, and he truly was one. Linjiao Luo and Jieping Fang gave me priceless help when my life was in trouble. Mason hosted a lot of weekend movies and made great cakes for every get-together.

I would like to say special thanks to Sheila Ferguson, who is always there not only solving numerous problems in the department, but also care about every student as a person.

I would also like to thank my parents who love me and support me regardless what I do and how much I achieve. They keep a permanent home for my mind.

Finally, I thank Daryl's company since the summer of 2005. His support has led me through the last stage of my Ph.D. study and given me courage and confidence to start a brand new career and pursue a life freely.

Dedicated to my father and mother.

xxvi

Chapter 1

Introduction

1.1 Overview

Since its first development by Hohenberg and Kohn in 1964 [1], Density Functional Theory (DFT) has found wide applications and great success in physics, chemistry, material science, electronics and bioscience. The once formidable problem of solving many-body Schrödinger equation became attackable. Despite the fact that approximations have to be introduced in the implementation of DFT in realistic systems, simulations have produced amazingly precise results on energetics and kinetics of systems that range from bulk materials to bio-molecules. With constant improvement of the theory and the development of powerful computers, the role of simulations within DFT has become more and more important in not only understanding experiments and phenomena, but also predicting and designing new materials and structures. In this chapter, a general review of DFT will be presented and the limitations of the theory will be discussed. I will also provide a brief introduction to the content of each chapter in this thesis.

1

1.2   The Schrödinger equation

The Schrödinger equation laid down the foundation for the quantum mechanical description of the physical world.

1.2.1   The Schrödinger equation for a solid

A complete description of a solid that consists of ions and interacting electrons with its total energy and electronic wave functions in its ground and excited states can be obtained by solving the Schrödinger equation. In many cases, the knowledge of the ground state is sufficient. In that case, the Schrödinger equation has the following form

$$\hat{H}\Psi(\{\mathbf{R_I}; \mathbf{r_i}\}) = E\Psi(\{\mathbf{R_I}; \mathbf{r_i}\}), \tag{1.1}$$

Where the Hamiltonian $\hat{H}$ has the form

$$\hat{H} = -\sum_i \frac{\hbar^2}{2m_e}\nabla^2_{\mathbf{r_i}} - \sum_I \frac{\hbar^2}{2M}\nabla^2_{\mathbf{R_I}} - \sum_{iI} \frac{Z_I e^2}{|\mathbf{R_I} - \mathbf{r_i}|} + \frac{1}{2}\sum_{ij(i\neq j)} \frac{e^2}{|\mathbf{r_i} - \mathbf{r_j}|} + \frac{1}{2}\sum_{IJ(I\neq J)} \frac{Z_I Z_J e^2}{|\mathbf{R_I} - \mathbf{R_J}|}. \tag{1.2}$$

In the above equations, $\hbar$ is Planck's constant divided by 2π; M_I is the mass of ion I; m_e is the mass of the electron; E is the energy of the system; $\Psi(\{\mathbf{R_I}; \mathbf{r_i}\})$ is the many-body wave function that describes the state of the system; $\{\mathbf{R}_I\}$ are the positions of the ions; and $\{\mathbf{r}_i\}$ are the variables describe the electrons.

The solution of Eq. 1.1 provides predictions of the electronic and geometric structure of a solid and thus is highly desirable. However, an exact analytical solution is available only for hydrogen atoms. Tremendous amount of effort has been put into

development of approximate solutions of Eq. 1.1. The very first step was made according to the Born-Oppenheimer approximation.

1.2.2 The Born-Oppenheimer approximation

Because of the large difference in mass between the electrons and the nuclei ($m_e \ll M_I$), and the fact that the forces on the particles are the same, the electrons respond essentially instantaneously to the motion of the nuclei. Thus the nuclei can be treated adiabatically, leading to a separation of the electronic and nuclear coordinates in the many-body wave function [2]:

$$\Psi(\{\mathbf{R_I}; \mathbf{r_i}\}) \longrightarrow \Psi_e(\mathbf{R_I})\Psi_{ion}(\mathbf{r_i}). \tag{1.3}$$

This adiabatic principle reduces the many-body problem to the solution of the dynamics of the electrons in some frozen-in configuration of the nuclei. In Eq. 1.1, the quantum mechanical term for the kinetic energy of the ions can be omitted, and the last term is simply a constant when the electron degrees of freedom are concerned. The Schrödinger equation describing the interacting electrons within the solid becomes

$$\hat{H}\Psi_e(\{\mathbf{r_i}\}) = E\Psi(\{\mathbf{r_i}\}), \tag{1.4}$$

where the Hamiltonian becomes

$$\hat{H} = -\sum_i \frac{\hbar^2}{2m_e}\nabla_{\mathbf{r_i}}^2 - \sum_{iI} \frac{Z_I e^2}{|\mathbf{R_I} - \mathbf{r_i}|} - \mathbf{r_i}| + \frac{1}{2}\sum_{ij(i\neq j)} \frac{e^2}{|\mathbf{r_i} - \mathbf{r_j}|}. \tag{1.5}$$

The energetic and electronic properties of a solid can be obtained by minimization of the energy E with respect to the electronic and ionic coordinates. Even with this simplification, the many-body problem remains formidable. The exchange and correlation effects among electrons are crucial to many phenomena such as superconductivity, but have been very difficult to describe. Considering the success that have been gained in the one-body problem, much effort has been made in developing one-electron picture of solids. In such approximations, the exchange and correlation effects between the electrons are taken into account in an average way. One example is the well-known Hartree approximation and the subsequent Hartree-Fock approximation [3]. Here we are to introduce an exact theory that allows total energy calculation to be performed accurately and efficiently under certain approximations when implemented, the Density Functional Theory.

1.3   The density functional theory

Density functional theory was developed by Hohenberg and Kohn [1] and Kohn and Sham [4]. The theory provided one simple method for describing the effects of exchange and correlation in an electron gas. It is proved that the total energy of an electron gas in the presence of a static external potential is a unique function of the electron density. The minimum value of the total energy functional is the ground state energy of the system, and the density that yields this minimum value is the exact single particle ground state density. This is a huge simplification considering that the many-body wave function of the system does not need to be specified. Further application of local approximation to DFT has brought great success to investigations of many types of materials and systems. Generally, total energy difference between

related structures can be believed to within a few percent and structural parameters to at least within a tenth of an Å. For details about DFT see [5, 6, 7, 8, 9].

1.3.1   The Kohn-Sham total energy functional

For a set of doubly occupied electronic states ϕ_i, from Eq. 1.5, the total energy of the system can be expressed as

$$E[\phi_i] = 2\sum_i \int \phi_i[-\frac{\hbar^2}{2m}]\nabla^2\phi_i d^3\mathbf{r} + \int V_{ion}(\mathbf{r})n(\mathbf{r})d^3\mathbf{r} + \frac{e^2}{2}\int \frac{n(\mathbf{r})n(\mathbf{r}')}{|\mathbf{r}-\mathbf{r}'|}d^3\mathbf{r}d^3\mathbf{r}' + E_{XC}[n(\mathbf{r})],$$

(1.6)

where V_{ion} is the static total electron-ion potential given by

$$V_{ion}(\mathbf{r}) = -\sum_I \frac{Z_I e^2}{|\mathbf{R_I} - \mathbf{r}|},$$

(1.7)

$n(\mathbf{r})$ is the electronic density given by

$$n(\mathbf{r}) = 2\sum_i |\phi_i(\mathbf{r})|^2,$$

(1.8)

and $E_{XC}[n(\mathbf{r})]$ is the exchange-correlation functional. It is the difference between the many body energy of an electronic system and the energy of the system calculated with Hartree approximation, which is the first three terms in Eq. 1.6. Eq. 1.6 is the so called Kohn-Sham total energy functional. Only the minimum value of this functional has physical meaning. At the minimum, the Kohn-Sham energy functional is equal to the ground state energy of electrons with ions at positions $\{\mathbf{R_I}\}$.

1.3.2 The Kohn-Sham equation

It is necessary to determine the set of wave functions ϕ_i that minimize the Kohn-Sham energy functional. These are given by the self-consistent solutions to the Kohn-Sham equations [4]

$$[-\frac{\hbar^2}{2m}\nabla^2 + V_{ion}(\mathbf{r}) + V_H(\mathbf{r}) + V_{XC}(\mathbf{r})]\phi_i(\mathbf{r}) = \varepsilon_i\phi_i(\mathbf{r}), \tag{1.9}$$

where ϕ_i is the wave function of electronic state i, ε_i is the Kohn-Sham eigenvalue, and V_H is the Hartree potential in the form

$$V_H(\mathbf{r}) = e^2 \int \frac{n(\mathbf{r}')}{|\mathbf{r} - \mathbf{r}'|}d^3\mathbf{r}'. \tag{1.10}$$

The exchange-correlation potential V_{XC} is given by

$$V_{XC}(\mathbf{r}) = \frac{\delta E_{XC}[n(\mathbf{r})]}{\delta n(\mathbf{r})}. \tag{1.11}$$

The Kohn-Sham equation presents one way to map the interacting many-electron system onto a system of noninteracting electrons under an effective potential due to all other electrons. If the exchange-correlation energy functional were known exactly, an exact exchange-correlation potential can be obtained by Eq. 1.11. Unfortunately, an exact $E_{XC}[n(\mathbf{r})]$ is not known. The Kohn-Sham equation needs to be solved self-consistently so that the occupied electronic states generate a charge density that produces the electronic potential that was used to construct the equation. The bulk of the work involved in a total energy calculation is the solution of sets of eigenvalue problems once an approximate expression for the exchange-correlation energy is given.

1.3.3 Local-density approximation

The most universally used approximation for the exchange-correlation energy of the electronic system is the local-density approximation (LDA) [4]. In LDA, the exchange-correlation energy of an electronic system is constructed by assuming that the exchange-correlation energy per electron $\varepsilon_{XC}(\mathbf{r})$ at a point $\mathbf{r}$ in the electron gas is equal to the exchange-correlation energy per electron in a homogeneous electron gas that has the same density as the electron gas at point $\mathbf{r}$. Thus

$$E_{XC}[n(\mathbf{r})] = \int \varepsilon_{XC}(\mathbf{r})n(\mathbf{r})d^3\mathbf{r}, \tag{1.12}$$

and

$$\frac{\delta E_{XC}[n(\mathbf{r})]}{\delta n(\mathbf{r})} = \frac{\partial[n(\mathbf{r})\varepsilon_{XC}(\mathbf{r})]}{\partial n(\mathbf{r})}, \tag{1.13}$$

with

$$\varepsilon_{XC}(\mathbf{r}) = \varepsilon_{XC}^{hom}[n(\mathbf{r})]. \tag{1.14}$$

The LDA approximation assumes that the exchange-correlation energy functional is purely local. It ignores corrections to the exchange-correlation energy at a point $\mathbf{r}$ due to nearby inhomogeneities in the electron density. Several parameterizations exist for the exchange-correlation energy of a homogeneous electron gas [4, 10, 11, 12, 13]. Considering the inexact nature of the approximation, it is remarkable that calculations performed using LDA have been so successful.

1.3.4 The band-gap problem within LDA

LDA within DFT usually provides good results for electronic states in the ground state of a system. However, it is well known that, for states of semiconductors and insulators, the LDA usually gives at most 2/3 of the experimental value. Errors of the order or larger than 50% are not uncommon [14, 15]. This band-gap problem originated from the fact that the Kohn-Sham eigenvalues are not the eigenvalues of the single-particle electron states, but rather the derivatives of the total energy with respect to the occupation numbers of these states [16]. The highest occupied eigenvalue in an atomic or molecular calculation is *nearly* the unrelaxed ionization energy for that system [17]. If one writes the one-electron spectrum given by DFT for an N-electron system as $\varepsilon_\lambda(N)$, the band gap ε_g^{DFT} obtained by the calculation is

$$\varepsilon_g^{DFT} = \varepsilon_{N+1}(N) - \varepsilon_N(N), \tag{1.15}$$

while the band gap ε_g^{exp} measured experimentally is

$$\varepsilon_g^{exp} = \varepsilon_{N+1}(N+1) - \varepsilon_N(N). \tag{1.16}$$

The difference between Eq. 1.15 and Eq. 1.16

$$\Delta_{gap} = \varepsilon_{N+1}(N+1) - \varepsilon_{N+1}(N) \tag{1.17}$$

gives rise to the error in the band-gap calculation. The physics is clear that the N host electrons cannot completely screen one additional electron even in the limit $N \to \infty$, because of the existence of the finite band-gap energy. The electronic ground state

is required to be changed [18]. Different approaches have been developed to correct the band gap error using electron self-energy calculations [19, 20, 21, 22, 23, 24] and generalized-density-functional theory [25, 26, 27, 28, 29].

1.4 Implementation of the density functional theory in calculations

While DFT solved the problem of describing electron-electron interactions, to solve Eq. 1.9 and thus obtain the information of the ground state of the system being considered, a few more important elements are still missing.

1.4.1 Pseudopotential approximation

The first element is the description of the electron-ion interactions. The pseudopotential theory was developed to solve this problem [30, 31, 32]. It is well-known that most physical properties of solids depend on the behavior of the valence electrons to a much greater extent than on the core electrons. The pseudopotential approximation exploits this by removing the core electrons and replacing them and the strong ionic potential by weaker pseudopotential that acts on a set of pseudo wave functions rather than the true valence wave functions. An ionic potential, valence wave function and the corresponding pseudopotential and pseudo wave function are illustrated schematically in Fig. 1 [9]. The valence wave functions oscillate rapidly in the region occupied by the core electrons due to the strong ionic potential in this region. These oscillations maintain the orthogonality between the core wave functions and the valence wave functions.
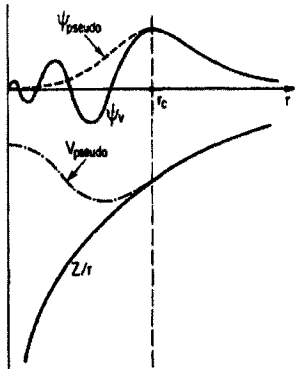
Fig. 1.1: Schematic illustration of all-electron (solid lines) and pseudoelectron (dashed lines) potentials and their corresponding wave functions. The radius at which all-electron and pseudoelectron values match is designated r_c [9].

The pseudo wave functions $\phi^{(v)}_{pseudo}(r)$ can be constructed to be nodeless inside the core (r smaller than the cutoff radius r_c) and match exactly the real atomic wave function beyond the core region ($r > r_c$), keeping $\phi^{(v)}_{pseudo}(r)$, $\mathrm{d}\phi^{(v)}_{pseudo}(r)/\mathrm{d}r$ and $\mathrm{d}^2\phi^{(v)}_{pseudo}(r)/\mathrm{d}r^2$ continuous at r_c. The corresponding pseudopotential is then produced by inverse the Schrödinger equation. A good pseudopotential should be finite and smooth near the origin, instead of having a $1/r$ singularity like the Coulomb potential. A more detailed discussion on choosing of pseudo wave functions and generating pseudopotentials can be found in [33].

1.4.2   Periodic supercells

Although it has been shown from the above discussion that the many-body problem can be mapped into effective single particle problem, there still remains the formidable task of handling an infinite number of non-interacting electrons moving in the static potential of an infinite number of nuclei or ions. In other words, since a wave function must be calculated for each of the infinite number of electrons in

the system, an infinite number of wave functions need to be calculated. At the same time, each of the wave function extends over the entire solid, the basis set required to expand it is infinite. These problems are overcome by performing calculations on periodic systems and applying Bloch's theorem to the electronic wave functions.

Bloch's theory states that in a periodic solid, each electronic wave function can be written as the product of a cell periodic part and a wavelike part [3].

$$\phi_i(\mathbf{r}) = \exp[i\mathbf{k} \cdot \mathbf{r}] f_i(\mathbf{r}).$$ (1.18)

The cell periodic part can be expanded by a basis set consisting of a discrete set of plane waves whose wave vectors are reciprocal lattice vectors of the crystal,

$$f_i(\mathbf{r}) = \sum_{\mathbf{G}} c_{i,\mathbf{G}} \exp[i\mathbf{G} \cdot \mathbf{r}],$$ (1.19)

where the reciprocal lattice vectors $\mathbf{G}$ are defined by $\mathbf{G} \cdot \mathbf{l} = 2\pi m$ for all $\mathbf{l}$ where $\mathbf{l}$ is the lattice vector of the crystal and m is an integer. Therefore each electronic wave function can be written as a sum of plane waves,

$$\phi_i(\mathbf{r}) = \sum_{\mathbf{G}} c_{i,\mathbf{k}+\mathbf{G}} \exp[i(\mathbf{k} + \mathbf{G}) \cdot \mathbf{r}]$$ (1.20)

The Bloch's theorem changes the problem of calculating an infinite number of electronic wave functions to calculating a finite number of electronic wave functions at an infinite number of $\mathbf{k}$ points. However, the electronic wave functions at $\mathbf{k}$ points that are very close will be almost identical. Thus it is possible to represent the electronic wave functions over a region of $\mathbf{k}$ space by the wave functions at a single $\mathbf{k}$ point. The electronic states at only a finite number of $\mathbf{k}$ points are required to

calculate the electronic potential and hence the total energy of the solid.

Methods have been developed to obtain very accurate approximations to the electronic potential and the contribution to the total energy from a filled electronic band by calculating the electronic states at special sets of **k** points in the Brillouin zone [34, 35, 36, 37]. Using these methods, one can obtain an accurate approximation for the electronic potential and the total energy of an insulator or semiconductor by calculating the electronic states at a very small number of **k** points. The electronic potential and total energy are more difficult to calculate if the system is metallic because a dense set of **k** points is required to define the Fermi surface precisely.

1.4.3 Computational procedures

The sequence of steps required to carry out a total energy calculation based on the above theories and approximations with conventional matrix diagonalization techniques is shown in Fig. 2. The procedure starts with an initial guess of the electronic wave functions, from which the electronic charge density, Hartree potential and the exchange-correlation potential can be calculated. Eq. 1.9 is solved at each **k** point to obtain the Kohn-Sham eigenstates. These eigenstates usually correspond to a set of wave functions that are different from the one originally guessed. New electronic potential is then taken to be a combination of the electronic potentials generated by the old and new wave functions and a third set of eigenstates are calculated. This process is repeated until the solutions are self-consistent.

The conventional way of solving Kohn-Sham equation uses plane waves as basis sets for the electronic wave functions and with Eq. 1.20 rewrites Eq. 1.9 into the form
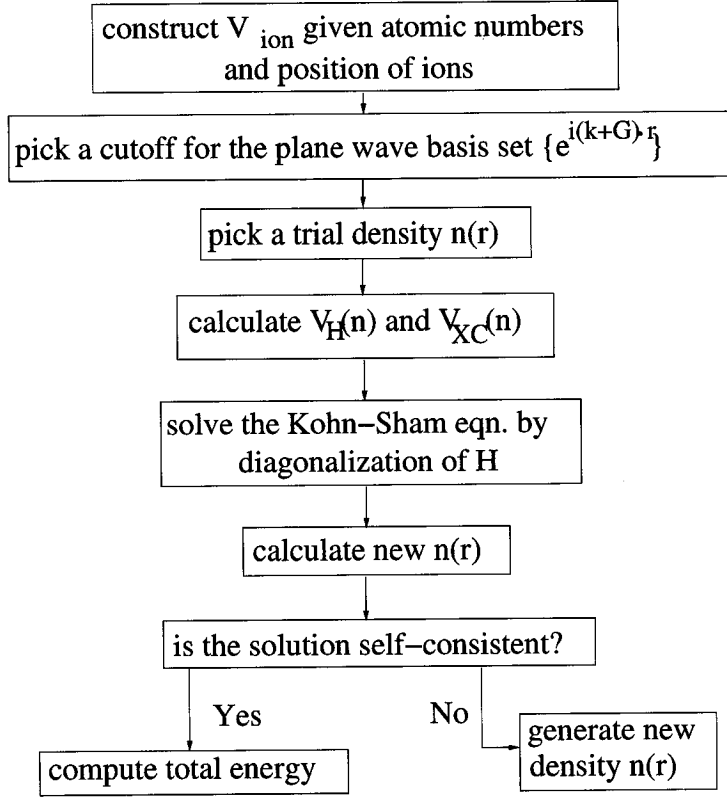
Fig. 1.2: Flow chart describing the computational procedure for the calculation of the total energy of a solid, using conventional matrix diagonalization [9].

$$\sum_{\mathbf{G}'} \hat{H} c_{i,\mathbf{k}+\mathbf{G}'} = \varepsilon_i c_{i,\mathbf{k}+\mathbf{G}'}, \tag{1.21}$$

where

$$\hat{H} = \frac{\hbar^2}{2m} |\mathbf{k} + \mathbf{G}|^2 \delta_{\mathbf{G}\mathbf{G}'} + V_{ion}(\mathbf{G} - \mathbf{G}') + V_H(\mathbf{G} - \mathbf{G}') + V_{XC}(\mathbf{G} - \mathbf{G}'). \tag{1.22}$$

At each interaction, $\hat{H}$ is diagonalized. The drawback of this method is computational too costly. Alternative methods have been developed to perform total

energy calculations with lower computational time and memory requirements and thus allow calculations on larger and more complex systems. One example is the Car-Parrinelo method in which the eigenvalue problems are solved with successively improving a trial wave function [38].

1.5   An overview of the present work

The success of the DFT has been clearly demonstrated in the the development and implementation of various robust DFT simulation packages, such as VASP [39], SIESTA [40] and ABINIT [41]. Over the years, the field of DFT simulation has developed two major branches: one continues with effort in methodology development to meet the increasing demands in studies of materials' transport properties[42], ferroelectric and magnetic properties [43, 44, 45], multiscale calculations of large systems [46, 47] and etc.; the other applies the methodologies in simulations and work on realistic problems to assist understanding phenomena and designing new materials and experiments.

The work presented in this thesis belongs to the latter category. Using DFT calculations, we have studied a variety of problems including 1) doping of crystalline and amorphous silicon for use in infrared sensors and solar cells; 2) one-dimensional (1D) magnetic nanowire formation on stepped surfaces for research on 1D physics and potential applications in sensors and nano-circuits; 3) a new type of semiconducting cyanide–transition-metal nanotubes with uniform electronic properties regardless of the diameter and chirality, which will facilitate its mass-production and use in industry; and 4) pentacene thin-film strictures and dynamics on silica surfaces for potential applications in organic thin-film transistors.

In chapter 2, I will discuss the sulfur defects in crystalline and amorphous silicon. This work is inspired by the experiments done in Prof. Mazur and Prof. Aziz groups at Harvard where they studied infrared absorption of sulfur doped silicon, using nanosecond and femtosecond laser melting[48, 49, 50, 51, 52]. Using first-principles calculation within DFT, we investigated the sulfur point defects in crystalline and amorphous silicon. Detailed energetic and electronic studies show that the sulfur atoms prefer two-coordinated sites in both situations and interprets the experimental results.

In chapter 3, I will present the study of kinetic processes of 1D wire formation on the stepped transition-metal surfaces. First part of the study focuses on the formation of Fe nanowires on the upper step edge of Cu(111) surfaces. The subject was originated from the long-standing puzzle of an experiment done in 1997 by J. Shen[53] where Fe nanowires were found to be formed on the upper step edge of the Cu(111) surfaces. We illustrated a two-phase wire formation procedure. The first step includes formation of an embedded Fe wire within the step, which is essential for the upper step edge wire formation but escaped experimental observation. This theoretical prediction was subsequently experimentally proved by the group of Prof. Weitering at University of Tennessee. The second part of the study is a generalization of the first part. Through studies of two sets of adatoms on Cu(111) and Pd(111) stepped surfaces, some simple trends in adatom behavior is revealed. These trends are found to related to the electronic interactions between the adatoms and the surfaces and could be used to facilitate 1D wire design and growth.

In chapter 4, a new cyanide–transition-metal nanotube is proposed. Using first-principles calculations, we investigated the energetic, electronic, and mechanical properties of the nanotube. We found that these nanotubes are semiconducting

with a large band gap 2 - 3 eV in spite of the diameter and chirality. The special features of these nanotubes made them feasible for mass-production, which is one of the most important shortcomings existing semiconducting carbon nanotubes have. Assisted with Dr. Jie Xiang, a scheme for experimental realization of the new tubes is also included in the discussion.

In chapter 5, pentacene thin-film structure and dynamics are studied using both the first-principles calculations within DFT and the force field molecular dynamics simulations. We investigated the bending of a single pentacene molecule, dynamics of pentacene molecules in vacuum, pentacene-pentacene and pentacene-substrate (silica) interactions, and pentacene islands on silica surfaces. We found that the pentacene mono-layer structure has a 90-degree rotation relative to the structure some experiments reported.

The appendices will cover two topics that are closely related to the subjects discussed in the previous chapters. Appendix A contains the notes on a tight binding band structure calculation on the $Pd(CN)_2$ sheet. The selection of orbitals is based on the DFT calculations done in Chapter 4. Appendix B presents the ongoing work on the Sn_2Se_6Pd mesostructures.

Simulation with DFT has provided a powerful tool to explore the world at an atomic level. It is playing a more and more important role in understanding and designing new materials, devices and etc. Research in the vast areas from engineering to hard condensed matter physics have benefited from its development.

Chapter 2

Sulfur point defects in crystalline and amorphous silicon
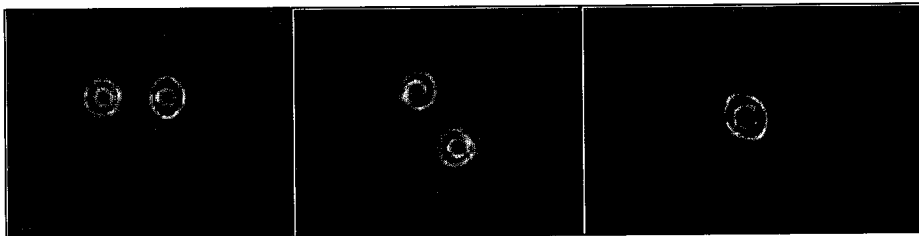
2.1 Overview

Si has been one of the best understood elements on the periodic table. It brought the booming of the semiconducting industry and made computers, cell-phones, ipods and all other electronic devices we use everyday available. Silicon is also the major material used in inorganic solar cells, which is believed to be one of the most promising alternative energy that can help relieve energy shortage within the next 50 years. Generally crystalline silicon brings best performance of the devices. However, the

17

cost of manufacturing bulk crystalline Si is very high. People have started using cheaper amorphous Si or Si thin-films, in which the efficiency is partially sacrificed to gain an overall better price.

With this world's increasing demand in energy supplies, the energy shortage problem becomes more and more critical. The current oil reservation can provide 32 years of supply at the current consumption rate. The global warming resulted from green house gases out of the petroleum industry further pushes people to look for alternative clean fuel cells and at the same time develop a zero-emission petroleum industry. Solar energy had caught people's attention long time ago. It has large storage and is clean. In places like Japan, Germany, and the US, more and more solar energy systems are being built and utilized. However, the whole industry did not take up a big share in the energy business as expected because of the high cost of building these systems.

The device that is used to convert solar energy into electricity is called a solar cell. The task of conversion is usually completed by semiconducting materials within the solar cell. The two essential processes involved are photogeneration of charge carriers (electrons or holes) and separation of the charge carriers to a conductive contact that will transmit electricity. More specifically, the first process is realized by doping and band-gap engineering of the semiconducting materials. Recent research work also demonstrated that certain semiconducting quantum dots can have multi-carrier generation from one photon absorption. Our work is related to the Si band-gap engineering to enhance silicon infrared absorption.

In this chapter present first-principles calculations for the behavior of sulfur point defects in crystalline and amorphous silicon structures. By introducing the sulfur point defects at various representative positions in the samples, including substitu-

tional and interstitial sites in the crystal and four-fold coordinated or mis-coordinated sites (dangling bond and floating bond sites) in the amorphous, we analyze the energetics in detail and determine the most stable structures. Two important conclusions we draw are: (a) in crystalline Si, the S defects form pairs in which the two S atoms are energetically bound but not covalently bonded; (b) in amorphous Si, they preferentially occupy three-fold coordinated sites, even when the starting configuration has higher coordination (four- or five-fold). The implications of these results for the electronic structure of sulfur-doped Si samples are also analyzed in the context of the present calculations.

2.2 Introduction

Silicon is an important technological material on which most of the semiconductor industry is based. Because of its importance, Si has been studied extensively, in particular as far as point defects are concerned, since it is the presence of such defects that render it useful as an electronic device material. The typical point defects involve the substitution of a Si atom by another element that can act either as an electron acceptor (positive dopant) or an electron donor (negative dopant). The common dopants involve elements that differ in valence from Si by only one electron, such as the positive dopants B and Al, or the negative dopants P and As; in these cases, the dopant atom provides a single carrier of positive (hole) or negative (electron) charge and the ion is located at a regular crystal site. More complicated situations can arise and can be of interest, from a technological as well as a fundamental point of view. One such case is that of group-VI atoms (chalcogens), like oxygen and sulfur, which in principle can provide two negative carriers when substituting for a Si atom.

However, the ability of these elements to form more complex structures with multiple bonds makes their behavior in the host Si crystal more difficult to understand.

Oxygen is an element that binds strongly to Si and is abundant in the atmosphere, so it is readily incorporated in a sample. The presence of oxygen atoms in a silicon crystal has received much attention. Single interstitial oxygen atoms are believed to be able to hop between the interstitial sites and oxygen dimers can diffuse even more freely [54, 55, 56, 57]. Sulfur has the same valence with oxygen and is in the same row of the Periodic Table with Si, so its incorporation in the Si crystal should be also quite favorable. It is natural to expect that substitutional S would induce less strain than O in the Si lattice, having a covalent radius of 1.04 Å, compared to silicon's 1.17 Å and to oxygen's 0.66 Å [33]. The behavior of S as a point defect in Si requires further clarification, both from the experimental and the theoretical point of view.

In this paper we study the behavior of sulfur point defects in Si, from the theoretical view point, using first-principles electronic structure calculations based on Density Functional Theory. Our results show that sulfur indeed behaves in some respects similarly to oxygen, but we also find some new bonding structures that are different from the oxygen doping cases. Previous theoretical work in chalcogen defects in silicon includes several studies similar in approach to what we pursue here [58, 59, 60]. Compared to these earlier studies, our calculations provide a much more detailed analysis of the behavior of sulfur atoms in the sample and lead to some unexpected conclusions that have not been found in any earlier work.

In addition to the studies in crystalline Si, we have undertaken theoretical studies of sulfur point defects in amorphous silicon, reported here for the first time to our knowledge. Amorphous silicon is a material of equal technological interest to crys-

talline silicon. It has wide applications in photovoltaic, where its electronic structure is of paramount importance.

The theoretical study of amorphous Si is complicated because there is no unique model structure. Typically, cells with disordered arrangements of atoms are generated by computer simulations, on which periodic or open boundary conditions are imposed. The models for amorphous Si involve coordination defects, that is, atoms that have coordination lower (three-fold) or higher (five-fold) than the normal four-fold coordination of covalently bonded Si atoms. The former type of defect is called a "dangling bond" defect, since the Si atoms are missing one of their regular covalent bonds, while the latter type of defect has been called the "floating bond" defect[61]. Experiments also support the presence of coordination defects in amorphous Si, although there remains some uncertainty as to the relative abundance of each type of defect. The presence of coordination defects leads to important electronic effects. The disorder of the network of atoms itself leads to localization of the electron states in amorphous silicon, which can be studied by electronic structure analysis [62] and identification of the band tail states [63]. Intrinsic defect states associated with dangling bonds and floating bonds have been contrasted [61] and analyzed in detail [64, 65, 66]. More recently, the energy landscape of amorphous silicon [67] and the energetics of hydrogen in amorphous silicon [68] have also been studied. The samples we have generated and studied involve structures with dangling bond and floating bond defects, as well as structures that have no coordination defects. In all of these, we have introduced sulfur atoms at judiciously chosen substitutional sites and studied in detail their electronic properties.

Another direct motivation for our study of sulfur atoms in crystalline and amorphous silicon samples comes from some recent experiments [69, 70], which exam-

ine optical properties, chemical composition and structure of silicon microstructures formed by femtosecond and nanosecond laser irradiation in the presence of SF_6. In these studies, below-band gap light absorption and photocurrent generation are observed [48, 49], which can be attributed to sulfur impurities in a microcrystalline surface layer [50]. In the sample formed by nanosecond laser irradiation, these features persist even after high temperature annealing [51], from which we infer that structures involving stable sulfur defects are formed. These intriguing experimental results raise the question of the nature of electronic states in amorphous Si and their possible differences or similarities to the corresponding states in crystalline Si.

The rest of this paper is arranged as follows: In section 2.3, we discuss the methodology employed for the first-principles electronic structure calculations, as well as the methods employed to produce and relax the amorphous samples. In section 2.4 we give the major results for sulfur point defects in crystalline Si. In section 2.5 we discuss properties of the amorphous Si which include or do not include intrinsic coordination defects, when sulfur atoms are substitutional or interstitial at representative Si sites. Finally, in section 2.6 we give our conclusions from the comparative study of sulfur defects in crystalline and amorphous silicon, and make contact with the recent experimental results of laser irradiation of S-doped Si samples.

2.3 Methodology

2.3.1 First-principles calculations

In the present paper, first-principles total energy calculations within Density Functional Theory (DFT) [1, 4] are employed to study the coordination, energy,

electronic and other properties of the pure and sulfur doped silicon samples. The DFT results reported here are based on the local density approximation (LDA) for the exchange and correlation functional [71, 72]. The calculations are carried out with the total-energy and molecular-dynamics computer code VASP [39], which employs a plane-wave basis. The default plane-wave energy cut-off for sulfur atoms, 197.79 eV, from the ultrasoft-pseudopotential database [73], is used for all calculations. The cell we use to model isolated point defects in crystalline Si consists of a $3 \times 3 \times 3$ supercell of the conventional cubic cell of bulk Si; this supercell contains 216 atoms. Similar cells were employed for the amorphous samples (see below). Because of the large supercells we used, only the Γ k-point is used to sample reciprocal space. The crystal silicon lattice constant determined with these computational parameters is 5.39 Å, which compares well to the experimental value of 5.43 Å. All atomic relaxations include relaxation of the supercell volume so that volume and symmetry are free to change. For static calculations, Gaussian smearing of width 0.00025 eV is used for the electronic states near the Fermi level. The criterion for convergence of the atomic relaxation was that residual forces on all atoms are smaller in magnitude than 0.01 eV/Å. One of the important properties we study is the coordination changes upon relaxation, especially those induced by the presence of the sulfur impurities. To define coordination, we consider atoms at a distance within 15% of the regular covalent bond in bulk crystalline Si to be related by bonds; in our calculations, this cutoff for bonded atoms turns out to be 2.70 Å.

2.3.2 Preparation of amorphous Si samples

For a realistic representation of the amorphous structure, a relatively large number of atoms must be included in the cell and the simulation must extend over

time scales that allow the structure to relax to a deep energy minimum. First-principles molecular dynamics (MD) simulations are numerically so intensive that they are limited to a short period of time ($\sim$ 10 ps) and a small number of atoms ($<$ 100) [38, 74]. To overcome this problem, various empirical interatomic potentials for Si have been developed and employed [75]. Luedtke and Landman [76, 77] tried to produce amorphous silicon structures by rapid quenching of a liquid using an empirical potential developed by Stillinger and Webwer [78]. Ishimaru, Munetoh and Motooka [79] generated amorphous networks from melted Si with various quenching rates by MD simulations employing the Tersoff potential [80]. Wooten, Winer and Weaire (WWW) introduced a "bond-switching" method for constructing samples with periodic boundary conditions, in which all atoms are exactly four-fold coordinated without any long range order [81]. The WWW method is capable of generating amorphous structures with very low strain and defect-free band gaps[82]. One drawback of this method is that it is not physical, in the sense that the local rearrangements of atoms which lead to the four-fold coordinated amorphous network do not mimic any physical process and could in fact be physically disallowed if the realistic energy cost for such moves were to be considered.

The computer generated models of amorphous Si are usually judged against experimental results to determine their reliability. The structural, dynamical and electronic properties of these structures agree reasonably well with experimental results [83, 84, 85].

In this chapter, we we create samples of bulk amorphous silicon (a-Si) by a standard and physically realistic method, that is, by quenching the liquid phase with explicit molecular dynamics using the environment dependent interaction potential (EDIP) [86]. We vary the conditions of quenching enough to produce a variety of

qualitatively different structural models. We then relax and evaluate these models using first-principles electronic structure methods, which provide a reliable and accurate description of the energetics.

High quality bulk samples of different sizes are prepared with the EDIP using periodic boundary conditions, while allowing the volume to vary at zero pressure. The first step is to create a well-equilibrated liquid by melting a perfect diamond crystal at a very high temperature (3000 K) for 50 ps and cooling it over 100 ps to 1500 K, where it is equilibrated for another 100 ps. Although this is near the bulk melting point, the short time and small system size prevent any nucleation of the crystal phase.

In finite samples in vacuum, surface curvature can further lower the melting point, e.g. to 1370 K for a nano-crystallite [87], but a flat, periodic interface between the liquid and an (already nucleated) crystal remains in equilibrium at the bulk melting point, T_c. Different, independent measurements have yielded the values, $T_c = 1500$ K [88], 1520 K [89], and 1530 K [89], which are consistent within simulation error. Note that these values are only 10% smaller than the experimental melting point of 1685 K, in spite of the fact that the potential was not fit to the melting point or any properties of the liquid [87].

Next, the sample is gently cooled over 1 ns to 1000 K through an abrupt first-order transition to the amorphous state, which occurs over roughly 100 ps near 1200 K (Simulations with flat amorphous-liquid interfaces yield a bulk melting point of $T_a = 1200$ K [88] or 1170 K [89]). The sample is then annealed at 1000 K for 2 ns, and cooled to zero temperature over another 2 ns. The sample can be somewhat further purified by heating it gradually back to 1000 K and repeating the 4 ns annealing/cooling cycle. Since the self-diffusion coefficient at 1000 K is 0.90

$\text{Å}^2/\text{ns}$ for the EDIP amorphous Si [88], the annealing cycles allow ample time for many structural re-arrangements at the scale of the atomic correlation length but insufficient time for diffusion across the entire sample, which would take 100 ns or 300 ns for $N = 64$ or $N = 216$, respectively, N being the number of atoms in the supercell.

In these simulations, a subtle and important size effect is observed: Decreasing the sample size (without changing the preparation steps) tends to improve the quality of the resulting amorphous phase, which is presumably due to the reduced relaxation time in smaller systems, perhaps aided by the enhanced effect of the periodic boundary conditions. As previously reported [87], large quenched samples ($N > 1000$) tend to have somewhat more than 5% coordination defects, always five-folded atoms or floating bonds in otherwise tetrahedral random network. Here we find that the 216-atom structures prepared according to the steps given above typically possess less than 10 isolated coordination defects (below 4%), while a 64-atom structure can be occasionally *completely free of defects*.

We have managed to create such a defect-free sample with 64 atoms, which we will take as representative of the ideal Continuous Random Network, as it applies to Si. Its thermodynamic [89] and elastic [90] properties have recently been calculated with EDIP. Further first principle relaxed ideal sample of bulk a-Si has features that are consistent with experimental estimates [87].

We will also investigate the properties of two other 216-atom samples, both of which contained coordination defects (the elastic properties of these samples are reported in Ref. [90]). The first sample, denoted as (a), is generated with EDIP by the liquid quench procedure. It has 8 floating bond defects (3.7%) with otherwise uniform four-folded coordination. One concern related to the liquid-quench method

of sample preparation by molecular dynamics is that, since the liquid has a higher average coordination than the amorphous phase, the resulting defective amorphous structures might have some memory of the liquid state. Although such structures should have physical relevance for ultra-rapid laser-melt amorphous Si [91], they might not reflect the typical defects found in other forms of amorphous Si [92].

To overcome these limitations of the liquid-quench simulation approach, we prepared one additional amorphous sample by imposing negative pressure and tensile strains, without artificially removing or manipulating any atoms. The sample is derived from an intermediate structure prepared by first applying a negative pressure of -100 GPa to bulk sample (a) at zero temperature, which causes the volume to expand by 10% through bond stretching, then annealing at 1100 K for 2 ns and then slowly cooling back to zero temperature, all the while maintaining constant volume to prevent collapse back to the original structure, and finally relaxing the volume at zero temperature until the sample returns to zero pressure. During the annealing step, atomic-scale voids (i.e. empty spherical cavities corresponding to at least two atomic volumes) are formed spontaneously to reduce the negative pressure caused by the enlarged volume. During the cooling step these tiny voids are quenched into the structure, which remains enlarged by roughly 10%, even after relaxed to zero pressure at zero temperature. Starting from this intermediate structure, the second amorphous Si sample with coordination defects, denoted as (b), is created by annealing the structure at 1100 K for 2 ns and then cooling, all at zero pressure. During the annealing step, the atoms are sufficiently mobile to annihilate all of the voids (thus reducing the excess volume and tensile strain), but there is not enough time for a complete relaxation of the volume. Sample (b) possesses a different set of coordination defects: 6 floating bonds and 1 dangling bond, which give a defect density

of 3.2%. These simulations show that the structure of amorphous Si can depend on the sample preparation history, as observed experimentally [92].

First-principles models of defective amorphous silicon are obtained from the 216-atom empirical bulk samples described above by complete structural relaxation, with the same computational parameters as for the crystal calculations. In order to have a larger sample without coordination defects that is not too different in size than the two 216-atom samples (so that the dopant density is comparable), we construct a 128-atom sample by repeating two 64-atom defect free cells along one direction and relaxing the structure again with the first-principles approach.

It turns out that the first-principles relaxations significantly changed the features of the empirically created samples; the coordination defects and energy per atom for the relaxed samples are given in Table 2.1. We call these relaxed samples A (obtained from the empirically created sample (a)), B (from sample (b)) and C (from the defect-free sample). C is still a defect-free sample with all atoms four-fold coordinated and bond lengths ranging from 2.27 Å to 2.49 Å. Its energy is 0.132 eV/atom higher than the energy of bulk crystalline Si. Although the samples A and B have different types of defects, they end up having very similar volumes and comparable total energies. Both have a total of six coordination defects (density 2.8%). These two samples have an energy per atom which is only slightly above that of the defect-free sample, by 0.135 eV/atom and 0.160 eV/atom higher, respectively, than bulk crystalline Si. These values are consistent with experimental expectations from bulk amorphous energy loss measurements. Also, a volume increase of about 1.0% fits well with the experimental data.

Sample	N_F	N_D	ΔE_0 (eV/atom)	$\Delta v/v_0$
A	5	1	0.135	1.0%
B	3	3	0.160	1.0%
C	0	0	0.132	2.7%

Table 2.1: Geometric and energetic features of the amorphous samples labeled A, B and C. N_F and N_D denote the number of floating bonds and dangling bonds, respectively. ΔE_0 is the energy difference between each sample and bulk crystalline Si, in eV/atom. $\Delta v/v_0$ is the percentage of volume change per atom compared to volume per atom in bulk crystalline Si.

2.4 Sulfur defects in crystalline Si

For the study of electronic states related to the presence of S dopants, we considered situations with the S atoms at substitutional lattice positions or at interstitial positions. The substitutional position is unique and will be denoted as S_S.

We considered a total of four different interstitial positions for the single S atom: the first three were high-symmetry positions that are typical of other interstitial atoms; they include the bond-center position, denoted as S_{BCI}, the hexagonal interstitial position which is situated at the geometric center of a hexagonal ring of Si atoms, denoted as S_{HI}, and the tetrahedral interstitial position which is situated at the geometric center of a tetrahedron defined by four Si atoms, denoted as S_{TI}. Our calculations show that the hexagonal or tetrahedral interstitial positions are higher in energy by 1.0 eV or 1.8 eV respectively, than the bond-center position. Accordingly, in the following we do not provide any more detailed discussions of these two cases. A fourth position for the interstitial S atoms, which turned out to be the lowest-energy one and is denoted as S_I, corresponds to placing the S atom on a plane that bisects a Si-Si bond, but not along the line joining the two Si atoms. When this structure is allowed to relax, the S atom assumes a buckled configuration, in which it

forms two bonds to Si atoms; this is actually similar to the preferred configuration of an interstitial O atom[54]. To verify the stability of the lowest energy configuration for the interstitial, S_I, we chose two other sites on the plane bisecting the Si-Si line along a bond and after relaxation we obtained a configuration with exactly the same geometric features and energy.

These calculations reveal that for an isolated S atom, the lowest energy configuration is the substitutional site. The tetrahedral interstitial site, S_{TI}, which has been considered before as a likely site[60] has a formation energy that is more than 3 eV higher than the substitutional case. Both these results agree well with earlier theoretical results [60]. The lowest energy configuration that we find for the interstitial, S_I, even though slightly higher than the energy of the substitutional site (by 0.3 eV), is worth further consideration. First, it is intriguing that the energy of this configuration is 0.95 eV lower than the bond-center interstitial configuration, S_{BCI}. The big energy difference between S_I and S_{BCI} is very different from the O case, in which these two configurations are almost degenerate in energy. Of course, there are also structural differences in the two off-center configurations for the S and the O interstitial atoms: specifically, in S_I we find a buckling angle of 122° for Si-S-Si, much smaller than the Si-O-Si buckling angle, which is about 160°; this can be attributed to the larger atomic size of the S atoms. In the buckled configuration, the S atom has two S-Si bonds at 2.11 Å each, slightly longer than in the bond-center configuration, S_{BCI}, at 2.07 Å. Second, the S atom is considerably farther away from the geometric bond-center than the O atom. As a result of this relaxation, the S atom has weak interactions with other Si atoms, although it is not covalently bonded to them. This may contribute to the big energy difference between S_{BCI} and S_I configurations for S, in contrast to the O case.

For a pair of S atoms in the crystalline supercell, we considered five different situations:

(a) The two S atoms taking the place of two adjacent Si atoms, denoted as S_{2S} and shown in Fig. 2.1(a).

(b) One S atom at the bond-center between two Si atoms and the second S atom at the closest center of two second nearest neighbored Si atoms, denoted as S_{I-NI} and shown in Fig. 2.1(b).

(c) Two S atoms at neighboring bond-centers between Si atoms, denoted as S_{2I} and shown in Fig. 2.1(c).

(d) We created a vacancy in the host Si lattice and placed the two S atoms in the middle of two edges of the tetrahedron centered at the vacancy site, denoted as S_{2I-V} and shown in Fig. 2.1(d).

(e) The two substitutional sites within the supercell that are farthest away.

The last situation corresponds energetically to two isolated S substitutional sites (it has the same formation energy per S atom as the single S atom in the supercell). Of the other configurations, the one with the lowest energy is S_{2S}, while S_{I-NI} and S_{2I} are about 0.9 eV per S atom higher in energy than it. Table 2.2 summarizes the results for these calculations.

One interesting consequence of these results is that S atoms in bulk Si bind in pairs to form the pair at nearest neighbor substitutional sites, which lowers the energy by 0.76 eV per S atom (1.53 eV for the pair), compared to isolated substitutional S atoms. The energy of configuration S_{2I-V}, which involves the formation of a Si vacancy, includes the vacancy formation energy cost, calculated to be 3.60 eV (this compares favorably with experimental results [93]). If this energy cost were not included, the formation energy of this configuration would be -5.57 eV per S atom,

(a)   (b)

(c)   (d)
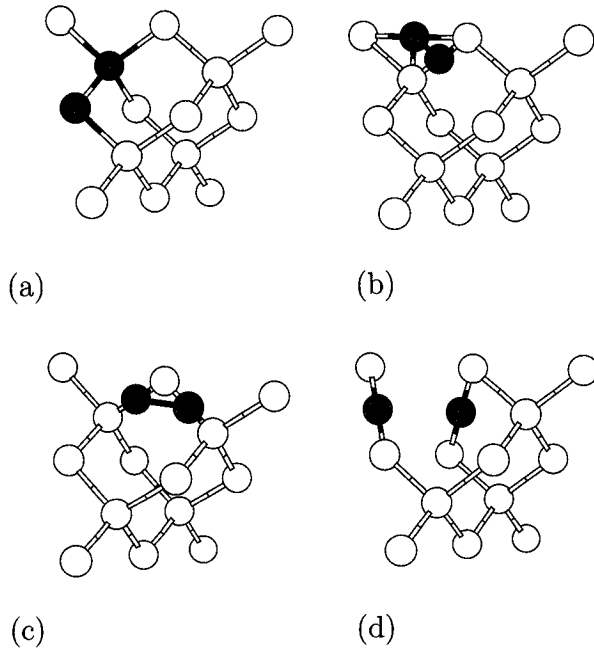
Fig. 2.1: Configurations considered for two S atoms in crystalline Si (the atomic relaxation is not shown): (a) at adjacent substitutional sites, S_{2S}, (b) at a bond center and an adjacent center of two second neighbor Si sites, S_{I-NI}, (c) at two neighboring bond centers, S_{2I}, (d) at the centers of opposite edges of a tetrahedron centered at a vacancy site, S_{2I-V} (see text for details). The grey spheres represent sulfur atoms and the white spheres silicon atoms.

which is larger than the formation energy of any of the other configurations that do not involve simultaneous creation of lattice defects like the vacancy. In other words, in a Si crystal where vacancies are abundant, the preferred configuration would be S_{2I-V}. However, this would not represent a thermodynamic equilibrium configuration, but a metastable state that can be formed if the vacancy concentration is prohibited from reaching equilibrium, by manipulating for instance the surface of the sample.

All structures containing S atoms have energy gaps that are comparable with that of the bulk. We note that these values are approximately half of the experimental

	E_f	$\Delta V/v_0$	ε_{gap}	ε_d	ε_F	Symmetry
S_S	−3.93	−0.08	0.56	0.24	0.25	T_d
S_{2S}	−4.69	−0.15	0.58	0.35	0.37	C_{3v}
S_I	−3.63	0.91	0.56	0.51	0.02	C_{1h}
S_{BCI}	−2.68	0.47	0.55	0.49	0.05	C_{3v}
S_{HI}	−1.78	0.61	0.54	0.35	0.35	C_{1h}
S_{TI}	−0.87	0.79	0.61	0.14	0.14	T_d
S_{2I-V}	−3.76	0.42	0.58	0.42, 0.57	0.02	C_{1h}

Table 2.2: Energetics, structural and electronic features of configurations with S impurities in crystalline Si. E_f is the formation energy (in eV) per S atom, assuming reservoirs to be bulk Si and isolated S atoms. $\Delta V/v_0$ is the percentage of total volume change relative to the volume v_0 per crystal Si atom ($v_0 = 19.574$ Å^3). ε_{gap} is the energy gap (in eV). ε_d and ε_F are the defect state level and the Fermi level relative to the valence band maximum (in eV). For crystalline Si, $\varepsilon_{gap} = 0.57$ and $\varepsilon_F = 0.00$ eV.

value, a well known deficiency of the theoretical framework employed here [22, 23, 24]. Except for cases S_I, S_{BCI} and S_{2I-V}, in which the S atoms are two-fold coordinated, all other S atoms introduce deep and filled defect states into the energy gap.

The S atoms at substitutional sites cause distortions, coordination changes and charge redistributions to their local environment, which are shown in Fig. 2.2 and Fig. 2.3. Some interesting features appear in the configurations involving two S atoms. Although the S atoms are energetically bound at nearest neighbor substitutional sites, they do not actually form a chemical bond among themselves. Instead, there is a geometric repulsion between them: in configuration S_{2S}, the S-S distance is 3.07 Å, compared to the bond length of 2.33 Å in bulk Si. Similarly, in configuration S_{2I-V}, which is the next lowest-energy configuration for the pair of S atoms, the S-S distance after relaxation is 2.85 Å, compared to 2.69 Å, the initial distance when the S atoms are placed at the mid-point sites between pairs of Si atoms adjacent to the vacancy site. The electronic charge density distributions shown in Fig. 2.3 confirm that there is no covalent bonding between the S atoms, since there is no
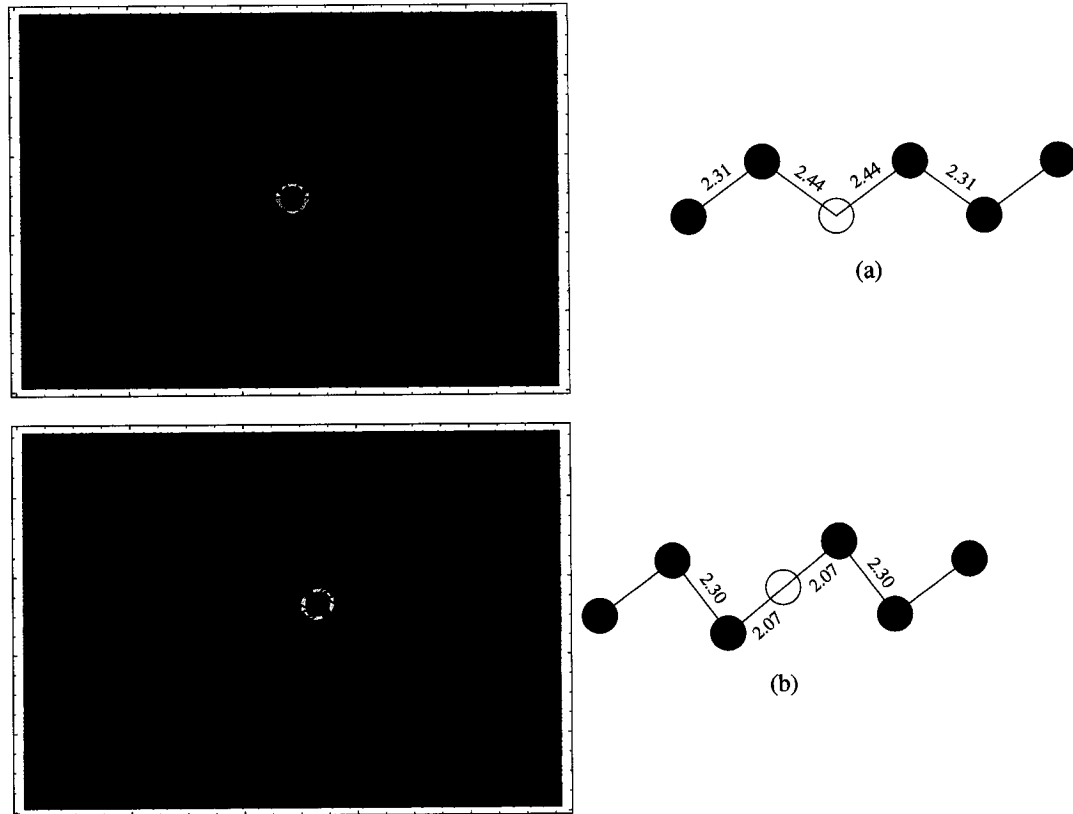
Fig. 2.2: Geometric structures and electronic charge densities of configurations (a) S$_S$ and (b) S$_I$ including atomic relaxation, on the (110) crystal plane. Filled circles represent Si atoms and open circles represent S atoms.

accumulation of valence charge in the region between the atoms, characteristic of a bond.

2.5 Sulfur defects in amorphous Si

In order to study the nature of doping of amorphous Si by S impurities, and to compare and contrast this to the behavior of crystalline Si, we introduced substitutional S atoms into the A and B amorphous Si samples and substitutional and
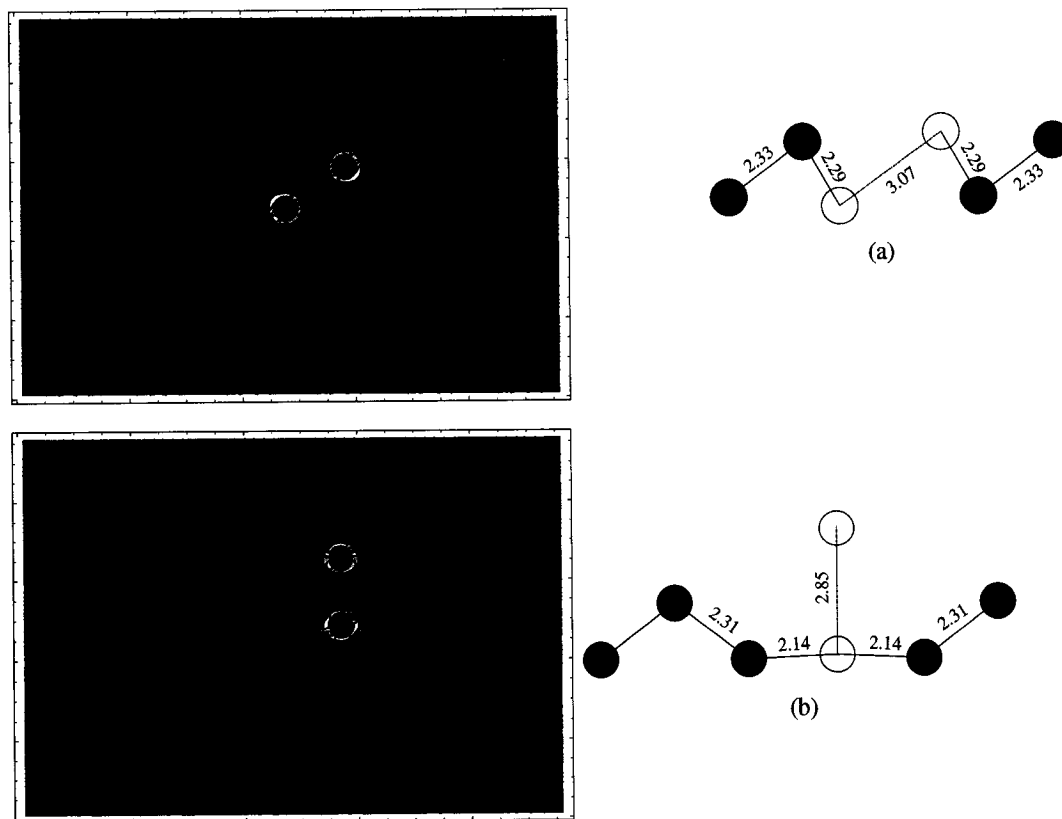
Fig. 2.3: Same as in Fig. 2.2 for the configurations. (a) S_{2S} and (b) S_{2I-V}.

interstitial S atoms into the C sample. The S atoms were placed at each one of the coordination defect sites, as well as at certain four-folded sites that are either very close to the defects or with a relatively long or relatively short average bond length. The energetic and geometric features of these structures are given in Table 2.3.

From Table 2.3, we see that the lowest formation energy corresponds to substitution of dangling bond defect sites. What is striking from this comparison is that a low formation energy is associated with low final coordination for the S atom (typically three-fold, and in one case even two-fold coordination), accompanied by a relatively short average bond length, in the range of 2.25 Å. Three-fold coordination

for the S atom is of course expected when it substitutes a three-fold coordinated Si atom (cases $D_1^{(B)}$, $D_2^{(B)}$, $D_3^{(B)}$), but it is also found for cases when it substitutes a four-fold (cases $T_1^{(A)}$, $T_2^{(A)}$, $T_5^{(B)}$), or even a five-fold coordinated Si atom (cases $F_1^{(B)}$, $F_2^{(B)}$, $F_3^{(A)}$ $F_4^{(A)}$, $F_6^{(A)}$, $F_8^{(A)}$). In all these cases, when the average bond length is in the neighborhood of 2.20-2.25 Å and the formation energies are lower than −5.20 eV; notice that the sum of covalent radii for Si and S is 2.21 Å. In contrast to this, when the average bond length exceeds 2.30 Å the formation energy is around −5 eV or higher. The only exception to this general trend is case $T_1^{(A)}$, which has three-fold final coordination and low formation energy, but relatively long average bond at 2.32 Å. The fact that the trend is not obeyed in all cases is a reflection of the diversity of local environments in amorphous Si; specifically, the local environment of a particular site may not make it feasible for the S dopant atom to achieve both its preferred coordination and its optimal bond length. This is probably the situation in case $T_1^{(A)}$.

What is surprising about the tendency of S atoms to form three-fold coordination, especially in the cases when the original configuration had four-fold or five-fold coordination, is that covalent bonds are eliminated (at least one in each case). Even in case $D_4^{(A)}$, where the final configuration involves a two-fold coordinated S atom, one covalent bond is eliminated relative to the initial configuration and the formation energy is still very low (−6.06 eV). Incidentally, this is also the configuration with the lowest average bond length for S, at 2.17 Å.

The striking preference of S atom to form three-fold coordinated structures, even when starting from a floating bond or a four-fold coordinated site, should have important implications in the electronic behavior of this dopant as well. Unfortunately, in the amorphous samples with several coordination defects there is no gap even

in the undoped case, so it is rather difficult to decipher the effect of the dopant from that of other defects, especially since the S dopant leads to significant atomic relaxation which is accompanied by shifts in many electronic states. For these reasons, we have not attempted to examine in more detail the electronic structure of the doped amorphous samples A and B. Instead, in order to understand better the electronic effects of S doping in amorphous Si, we turn our attention to sample C, which has only four-fold coordinated sites to begin with, but also has a clear gap in the electronic spectrum.

In sample C, we chose eight different substitutional sites to introduce the S dopant atom: one with the longest average bond length, referred to as $T_6^{(C)}$, one with the shortest average bond length, referred to as $T_{13}^{(C)}$, and six with their average bond length very close to the average bond length in the entire sample, listed from $T_7^{(C)}$ to $T_{12}^{(C)}$. Another three sites were chosen, in which the S atoms are placed in the middle of relatively long Si-Si bonds, referred to as $I_1^{(C)}$, $I_2^{(C)}$ and $I_3^{(C)}$. The nature of these sites has a rough analogy to the interstitial sites in crystalline Si, although the nature of the amorphous network is such that it makes the term interstitial rather ill defined. Nevertheless, we employ this term here to make the comparison more direct. In Table 2.4 we include the results of these calculations, in what concerns both energetics and geometric arrangements, as well as electronic structure features.

Of all the samples, the interstitial S atoms have the lowest formation energies. There are no distinguishable defect states introduced in the original band gap of sample C by these defects. The three sites we tried have relatively long bond lengths that are between 2.40 Å and 2.50 Å; there are fewer than 10% of such bonds in the entire sample. The amorphous network has enough structural flexibility to accommodate these additional S atoms without major coordination changes farther from

the defect site, with the adjacent Si atoms remaining four-fold coordinated. As a check, we also considered another interstitial site, at the center of Si-Si bond with a relatively short bond length. It turns out that the local structure in this case changed significantly, and the S atom ended up three-fold coordinated with a much higher formation energy.

Of all the substitutional cases, except for cases $T_6^{(C)}$ and $T_{13}^{(C)}$, all other S atoms end up with three-folded coordination. In fact, case $T_{13}^{(C)}$ is not much different because, even though by our strict definition of coordination it has four nearest neighbors, three of those are at distances around 2.25 Å and the fourth is much farther away at 2.49 Å. In case $T_6^{(C)}$, the S atom is two-fold coordinated, having broken two of the bonds that the Si atom had at the same site.

Judging from these results, we can infer that essentially in all cases, the substitutional S atom will end up in a three-fold coordinated site. Looking at the electronic properties of these samples, we find that the Fermi energies are shifted up by about 0.5 eV, compared to the original Fermi level for the pure sample C. Each of them has a doubly filled defect state in gap. Detailed analysis by projecting electronic wave functions of the sample onto s, p and d spherical harmonics centered at the positions of the ions, shows that these gap states are mainly localized on the neighboring Si atom that is has the longest bond length from the substitutional S atom. These observations fit well with the model built by R. A. Street for substitutional defects in amorphous silicon [94], in the context of which we analyze next the behavior of the S dopants.

According to Mott's N-8 rule, a neutral S atom would have to form two covalent bonds and be in state S_2^0. This strict rule forbids substitutional doping in amorphous semiconductors. But experimental results show that low level doping actually does

occur in amorphous semiconductors. In our case, as in [50], the doping level of S is about 0.5%. Street[94] relaxed the 8-N rule by allowing the doping atoms to be ionized. This model, applied to our results yields the following picture: by losing one electron, the S atom turns into a three-fold coordinated state, S_3^+, while at the same time a neighboring Si atom accepts the electron and forms a three-folded coordinated dangling bond state D^- (referred to as compensating state[94]). The antibonding state of S_3^+ is empty but the D^- state in the gap is filled. This is why the position of the Fermi level in these cases is shifted up by about 0.5 eV. From Table 2.4, a higher shift of the Fermi level corresponds to a higher formation energy. It is also clear that high level of doping is not possible because the Fermi level can only shift up to the lowest conduction band.

When there is not enough room for complete relaxation, as in case $T_{13}^{(C)}$, where the Si atom had the smallest average bond length in the original configuration at 2.30 Å, the S atom may be in a nominally four-fold coordination but actually with only three close neighbors. In this case a S_4^0 state is formed. Two extra electrons that are not in bonds will occupy the antibonding state. This is why the Fermi level of this configuration is shifted up by about 1.0 eV, and ends up just below the conduction band and higher than the deep gap states associated with D^-.

We discuss last the S substitutional case labeled $T_6^{(C)}$, in which the S atom is two-fold coordinated. In this case there is no shift in the Fermi level and the defect state below the conduction band is empty. This configuration also corresponds to relatively low formation energy. This raises the question of whether volume restrictions lead to creation of a majority of three-fold coordinated sites for S, as opposed to two-fold coordinated sites that seem to be a more natural state for this impurity. In order to address this question, we examined carefully the bond lengths of the three S-Si

bonds for each three-fold coordinated S atoms and found that, unlike the situation in $T_{13}^{(C)}$, these lengths have mostly very close values. There is no obvious trend of breaking any one of them. Thus we conclude that the electronic properties must be playing a more important role. In order to revert from the S_3^+ state back to the S_2^0 state, it requires transferring one electron back to the S atom while breaking a S-Si bond and creating a new D^- state in the adjacent Si atom whose bond to S is broken. However, this coordination for the Si neighbor is forbidden by the 8-N rule. Thus, although the two-fold coordinated state for the S dopant would be preferred, because of the initial coordination number and the restrictions imposed by the 8-N rule, three-fold coordination is the most likely outcome.

The same argument can be applied to the preceding results of S dopants in the amorphous samples A and B. Although it is hard to make a similar detailed analysis because of the existence of intrinsic defects in these two samples, the same explanation for the overwhelming three-fold coordination of the S dopant atoms should still be valid.

2.6   Conclusions

Our study of S doping of crystalline and amorphous Si samples has revealed a number of unexpected results, which we summarize here. In crystalline Si, we find that the substitutional position for the single S dopant atom is preferred. An interstitial S atom with a buckling angle 122° has an energy 0.3 eV higher than the substitutional one but is 0.95 eV lower than a bond-center S atom without buckling. Two S dopant atoms form a nearest-neighbor substitutional pair which has an energy lower than the two isolated substitutional S atoms by 1.53 eV, even

though the two S atoms in the pair are not bonded covalently and each one is three-fold coordinated. In coordination-defect-free amorphous Si, we found that interstitial two-fold coordinated S atoms have the lowest formation energy. Substitutional S atoms, in both the coordination-defect-free sample and the defective samples, tend to form structures of mostly three-fold coordination. This is expected when the original Si site is a dangling bond coordination defect, but it is also true when the original site is four-fold or even five-fold coordinated (a floating bond defect). Exceptions occur in special cases, when the local environment allows the substitutional S atom to break one or two bonds and become two-fold coordinated, while the neighboring Si atoms relax without introducing a high energy cost. Thus, we conclude that under equilibrium conditions the overwhelming majority of substituional S atoms will be three-fold coordinated, either by forming substitutional pairs in crystalline Si, or by substituting Si atoms in the most common sites (four-fold coordinated or dangling bonds) in amorphous Si, a conclusion supported by a detailed analysis of the electronic properties.

We can now use the results of this study of S point defects in crystalline and amorphous Si to interpret the experimental findings related to the so called "black Si"[51]. In preparing these samples, the experimenters used nanosecond (ns) laser and femtosecond (fs) laser irradiation. The ns-irradiated structure has very little disorder while the fs-irradiated sample is covered by a disordered nanocrystalline surface layer. An amorphous layer is created on both samples, in which S atoms are incorporated. These S atoms, according to our study, will mostly be two-fold or three-fold coordinated. The presence of intrinsic coordination defects (dangling and floating bonds) in the amorphous layers makes the samples light absorbing (black). On the other hand, ion-implantation would most likely result in interstitial (e.g. bond

center) S defects that bring in shallow empty states near the conduction bands. These states will not affect the light-absorption spectrum much. After annealing, the ns-irradiated sample reverts to crystalline structure and S atoms are forced to be three-fold or four-fold coordinated in the lowest energy substitutional positions. These S atoms lead to defect-induced occupied gap states. Thus, the ns-irradiated sample remains light-absorbing, although the absorption of light is lowered compared to the sample before annealing. The fs-irradiated sample is highly disordered. Annealing leads to elimination of some of its intrinsic defects and rearrange S atoms, but not complete crystallization. According to the estimation of Roorda and W. C. Sinke, the remaining defect concentration in a-Si is about 1%[95]. During annealing, we expect the S atoms to saturate these defects and become two-fold coordinated themselves (Like cases $D_4^{(A)}$, $I_1^{(C)}$, $I_2^{(C)}$ and $I_3^{(C)}$). Thus a clean band gap is recovered in the fs-formed sample and the silicon is transparent again.

Finally, our study affords some theoretical predictions about the behavior of S-doped Si, under equilibrium conditions: In crystalline silicon samples, the S atoms will be in substitutional sites and create occupied deep gap states. The transparent silicon will turn into black. In amorphous silicon, the S atoms will be in interstitial sites and saturate the intrinsic defects of the a-Si samples. With a proper S doping rate (comparative to the defect rate), a defective a-Si black sample will turn into transparent.

Following this detailed analysis of the geometric and electronic structure of *equilibrium* configurations for S dopants in crystalline and amorphous Si, it would be of great interest to study the *kinetics* of S incorporation in bulk Si to determine whether or not kinetic barriers play an important role in what is actually observed experimentally.

2.7 Acknowledgments

This work is done in collaboraion with Martin Bazant and Efthimios Kaxiras. The authors thank Professor M. Aziz, Dr. Zhenyu Zhang and Dr. Gang Lu for many helpful discussions. The work of E. Kaxiras is in part supported by the Nanoscale Science and Engineering Center of Harvard University, which is funded by the National Science Foundation.

Site	E_f	$\Delta V/v_0$	$\bar{b}_i$	C_f	$\bar{b}_f$
$D_1^{(B)}$	-6.55	0.41	2.31	3	2.24
$D_2^{(B)}$	-6.29	0.55	2.33	3	2.26
$D_3^{(B)}$	-6.25	0.36	2.32	3	2.27
$D_4^{(A)}$	-6.06	-0.08	2.41	2	2.17
$F_1^{(B)}$	-5.96	0.55	2.48	3	2.27
$F_2^{(B)}$	-5.30	0.25	2.45	3	2.25
$F_3^{(A)}$	-5.26	-0.36	2.42	3	2.24
$F_4^{(A)}$	-4.99	-0.44	2.45	3	2.35
$F_5^{(B)}$	-4.95	0.20	2.45	4	2.34
$F_6^{(A)}$	-4.83	-0.26	2.46	3	2.32
$F_7^{(A)}$	-4.34	-0.44	2.42	4	2.39
$F_8^{(A)}$	-4.05	-0.04	2.51	3	2.39
$T_1^{(A)}$	-5.81	-0.25	2.43	3	2.32
$T_2^{(A)}$	-5.50	-0.05	2.39	3	2.26
$T_3^{(B)}$	-5.09	0.17	2.28	4	2.33
$T_4^{(A)}$	-4.89	-0.58	2.28	4	2.30
$T_5^{(B)}$	-4.63	0.49	2.42	3	2.35

Table 2.3: Energetic and geometric features of S point defects in amorphous Si samples. D, F and T stand for dangling-bond, floating-bond and tetrahedral sites, where the substitutional S atoms are introduced; the superscript in each case denotes the sample (A, B and C, as described in the text). E_f (given in eV) is the formation energy, taking the ideal a-Si sample C as the reservoir for the Si atoms and the isolated S atoms for the S reservoir. The different cases are ordered in increasing formation energy. $\Delta V/v_0$ is the change in total volume of the sample upon the substitution, normalized to the crystalline atomic volume v_0. C_f is the final coordination of the S atom (the initial coordination of the Si atom being determined by the site identity, D, F or T) and $\bar{b}_i, \bar{b}_f$ are the initial and final average bond lengths of the site.

Site	E_f	$\bar{b}_i$	C_f	$\bar{b}_f$	ε_{gap}	ε_d	ε_F
$I_1^{(C)}$	-5.14	2.44	2	2.14	0.96	—	0.02
$I_2^{(C)}$	-5.03	2.48	2	2.14	1.05	—	0.03
$I_3^{(C)}$	-5.01	2.48	2	2.14	1.03	—	0.01
$T_6^{(C)}$	-4.56	2.39	2	2.17	1.10	0.91	0.01
$T_7^{(C)}$	-4.74	2.31	3	2.26	0.95	0.34	0.34
$T_8^{(C)}$	-4.35	2.38	3	2.27	1.05	0.36	0.38
$T_9^{(C)}$	-4.15	2.33	3	2.23	1.08	0.47	0.49
$T_{10}^{(C)}$	-3.85	2.33	3	2.28	1.06	0.80	0.83
$T_{11}^{(C)}$	-3.63	2.34	3	2.30	1.04	0.49	0.49
$T_{12}^{(C)}$	-3.52	2.35	3	2.31	1.07	0.60	0.62
$T_{13}^{(C)}$	-3.89	2.30	4	2.32	1.07	0.89	0.91

Table 2.4: Energetics, geometric features and electronic structure of S substitutional and interstitial dopants in amorphous Si sample C. The meaning of symbols is the same as in Table 2.3. $\bar{b}_i$ for interstitial cases denotes the Si-Si bond length, in between of which the S atom is put into. And $\bar{b}_f$ in these cases denotes the average bond length of S atom after relaxation. ε_d is the position of the dopant state in the gap relative to the valence band maximum and ε_F is the position of the Fermi level. The energy gap of the pure amorphous Si sample is 1.05 eV and its Fermi level is at 0.01 eV.

Chapter 3

One-dimensional nanowires on stepped transition-metal surfaces
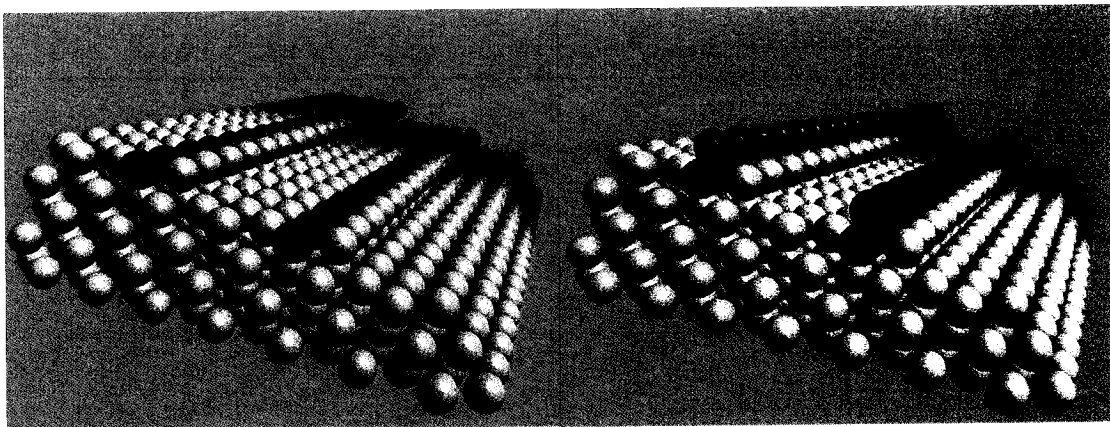
3.1 Overview

Surface science started a second boom with the development of nano-science. It serves as a perfect template for nanowires, nanotubes, nanodots and thin-films growth. The combination of the surfaces and the nanostructures makes interesting

46

physics. Understanding of the interesting phenomena in these systems also assists reaching the ultimate goal of applications in industry.

Generally the growth problems on surfaces can be categorized into two: catalyst-assisted and self-assembled growth. The work in this chapter falls into the second category. Literally, "self-assemble" means assemble without guidance or management of from an outside source. This method is of particular interest because of several reasons. First of all, it is beautiful and resembles nature. From all scales of molecules to the galaxies, self-assembly is taking place everywhere in nature. The picture it provides is simple and neat. Second, self-assembly is widely used in industry because it is highly reproducible and free of contamination from other unwanted elements.

Simply governed by the adatom-surface interactions, many the self-assembled structures demonstrate amazing order on surfaces. Zero-dimensional nanodots, one-dimensional nanowires and nanotubes, two-dimensional monolayer thin-films have all been realized on different surfaces. Magnetic and electronic properties of these structures have been intensively studied both experimentally and theoretically. More recently, some structures grown on strained surfaces have been found with desired properties that could not be obtained on normal surfaces. New excitements are constantly coming and there are many to explore.

Growth processes can be experimentally monitored by various techniques and equipments, such as diffractions and scanning probe microscopes. identification of the growth processes facilitates the understanding of the physical structures of the nano-materials on surfaces, which eventually decide the properties of these systems. With the decreasing sizes of the nanostructures, a resolution at atomic scale is required. Unfortunately, the "eye" of the equipments usually cannot catch every single atom and sometimes will even provide misleading information. Simulation fills the gap

between single atom behavior to observed nanostructure and its properties.

In this chapter, I will focus on the growth processes of nanowires on stepped transition-metal surfaces. In section 2, a long standing puzzle of formation of upper-step-edge Fe nanowires on Cu(111) surfaces will be solved through illustrations of the kinetic pathway of this formation. Following this, in the second section, a subsequent experiment has been carried out and clearly identified the two steps within the pathway. Scanning tunneling microscope simulations further confirm the experimental observations. In the last section, we generalize the study to step-edge behavior of two sets of adatoms on Cu(111) and Pd(111) surfaces. We hope that this study provide some insights into the problems of nanostructure growth on stepped transition-metal surfaces.

3.2 Kinetic pathway for the formation of Fe nanowires on stepped Cu(111) surfaces

We report the discovery of a novel kinetic pathway for the formation of one-dimensional Fe nanowires of single atom width, on stepped Cu(111) surfaces. This pathway, identified through extensive total-energy calculations within density functional theory, establishes that the stable structure involves a row of Fe atoms on the *upper* edge of a step. The formation of the surface wire is preceded by facile incorporation of an initial row of Fe atoms into the surface layer at one lateral lattice constant away from the step edge, which then acts as an attractor for the second, exposed row of atoms. The resulting wire structure provides a natural interpretation of existing experimental results. We also explore the applicability of this mechanism in formation of other related systems.

3.2.1 Introduction

One-dimensional (1D) electron systems are expected to possess many unconventional physical properties, most notably non-Fermi liquid behavior [96]. Unambiguous confirmation of such properties has been sparse, largely because of the difficulty in obtaining truly 1D electron systems [97, 98]. Among various approaches to overcome the formation bottleneck, growth of quantum wires through decoration of surface steps has received intensive attention [99]. Example systems include metallic wires on semiconducting[100, 101] or insulating substrates[102], and magnetic wires on nonmagnetic metal substrates[53, 103, 104, 105, 106]. The former class of quantum wires serves as testing ground for electrical transport in quasi-1D systems; the latter offers opportunities to study magnetism and spin transport in 1D systems.

In recent experimental studies of magnetic wires on stepped metal surfaces, most of the wires were found to form at the lower edge of monatomic-layer-high steps[104, 105, 106]. This prevailing feature is not too surprising, because an adatom of a given magnetic element typically prefers to occupy a stable adsorption site located at the lower edge of a step, thereby leading to the nucleation and growth of a wire along the lower step edge. In light of this general trend, the experimental observation that Fe wires of varying widths are formed at the *upper* step edges on a vicinal Cu(111) surface[53] was rather surprising. Because of the intriguing magnetic properties of these Fe wires, the initial observation stimulated an extensive line of experimental and theoretical studies aimed at explaining the microscopic origin of the magnetic properties [107, 108, 109]. In essentially all these previous studies, the magnetic properties were explored for given static Fe wire structures. It remains a mystery why such Fe wires prefer to form at the upper edges of steps, and what are the kinetic mechanisms that lead to their formation.

3.2.2 Results

In this section, we resolve this long-standing puzzle by revealing the kinetic mechanism involved in the formation of Fe wires at the upper edges of steps on the Cu(111) surface. Using extensive total-energy calculations within density functional theory (DFT), we find that an Fe wire at the upper edge, with an *apparent*(visible to STM images) width as narrow as one atom, is already energetically more stable than the corresponding structure at the lower edge of the step, but only under the condition that another row of Fe atoms be incorporated underneath the exposed row. The kinetic pathway for the formation of such a novel wire structure involves two phases. First, a row of Fe atoms are incorporated into the upper terrace, one lateral lattice constant away from the step edge. This is the energetically preferred and kinetically accessible final configuration whether the Fe adatoms approach the step from the upper or from the lower terrace. Subsequently, additional Fe adatoms diffusing on the terrace are strongly attracted to the buried basal wire, thereby forming an atomic wire exposed at the upper edge. We discuss this central finding in comparison with existing experiments. We also attempt to rationalize the preference of the two-phase kinetic pathway based on generic qualitative arguments, and support these arguments by examining related systems.

The DFT results reported here are obtained with the VASP code [39], using the Perdew-Wang 1991 version of the generalized gradient approximation (PW91-GGA)[110]. The default plane-wave cutoffs for different elements from the GGA ultrasoft-pseudopotential database[73] are adopted in the calculations. The Fermi-level smearing approach of Methfessel and Paxton[36] is employed for the electronic states near the Fermi level, with a Gaussian width of 0.2 eV. Optimized atomic geometries are achieved when the forces on all the unconstrained atoms are smaller

in magnitude than 0.01 eV/Å. The bulk Cu lattice constant determined with these computational parameters is 3.645 Å, which compares well with the experimental value of 3.63 Å. The nudged elastic band method (NEB)[111], followed by spline interpolation, is employed to determine the transition state pathways and energy barriers.

There are two types of steps on Cu(111), referred to as A and B, with the former having lower formation energy [112]. Experimentally, Fe wires have been observed to form on the upper edges of both types of steps[113]. Hence, in the present study we focus our attention on growth of Fe wires on A-type steps. Following Ref.[114], we model the stepped Cu surface by a slab miscut along the (322) direction, consisting of (111) terraces of width five lateral lattice constants separated by type A steps of monatomic height. The slab used in the calculations contains seven layers and a total of 96 Cu atoms in the periodic supercell. The bottom three layers are fixed at their respective bulk positions during the relaxation. A $2 \times 2 \times 1$ mesh in the Brillouin Zone of the supercell is used to sample the reciprocal space. The vacuum region separating slabs is equivalent to 11.5 Å.

We first study the interaction of a single Fe adatom with the stepped surface. Our calculations show that the preferred adsorption site of an Fe adatom is always the fcc site, whether it is in the central region of a terrace or in the immediate vicinity of the step. In contrast, the activation energy barrier encountered by the adatom when it moves on the surface can differ significantly in the two regions. For terrace diffusion, the preferred mechanism is via direct hopping, with an activation energy barrier of 0.025 eV. When reaching a step from the upper edge [Fig. 3.1(a)], an Fe adatom would have to overcome a barrier of 1.00 eV if it were to climb down by direct hopping over the step edge [Fig. 3.1, $A_1 \rightarrow B_1$]. A naive interpretation of this
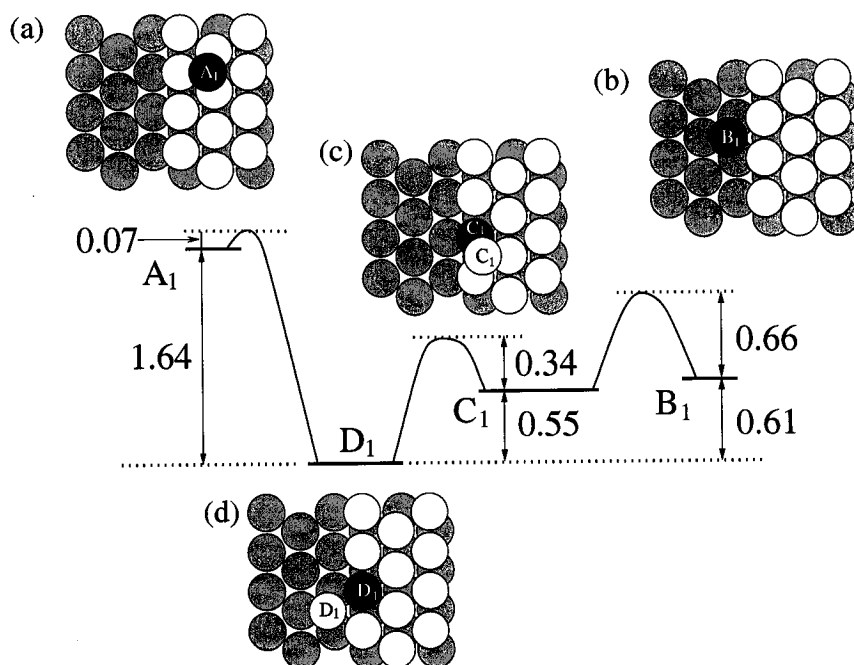
Fig. 3.1: Top view of the surface model employed in the calculations, showing the first phase of Fe wire formation. The white and gray circles represent Cu atoms in the first and second layers, respectively; the black circles represent Fe atoms. (a) Initial configuration of an Fe adatom reaching the step from the upper terrace. (b) Initial configuration of an Fe adatom reaching the step from the lower terrace. (c) Intermediate state of the Cu-Fe assisted exchange as the state B_1 converts to the final state D_1 in (d), which is also the stable final configuration from A_1 after place exchange. The relative energies and the activation barriers (in eV) connecting the different configurations are indicated next to vertical arrows.

result suggests that the high energy barrier for downward motion of Fe adatoms over the step edge would offer an explanation for the formation of Fe wires at the upper step edges of the Cu(111) surface. But the real physical situation is more intricate, and thereby more challenging. The Fe adatom, instead of hopping down against the high energy barrier, can easily be embedded into the Cu layer through an exchange process [Fig. 3.1, $A_1 \rightarrow D_1$], with an energy barrier of only 0.07 eV. Furthermore, the Cu atom displaced by the Fe adatom in the exchange process prefers to stay at the lower edge of the step, adjacent to the embedded Fe atom, because it would have

to overcome a high activation barrier of about 0.9 eV in order to reach the nearest hcp site away from the step edge.

The above discussion establishes how an Fe adatom approaching the step from the upper terrace will end up embedded in the step edge. Fe adatoms can also approach a step from the lower terrace. It is therefore necessary to examine the optimal final configuration for this situation. Here, we find that the Fe atom switches position with a Cu atom at the step edge, through a slightly more complex motion involving an intermediate state C_1. The Fe atom is first incorporated into the step by displacing a Cu atom upward onto an hcp site at the upper step edge [Fig. 3.1(c)], a process which has an activation barrier of 0.66 eV [Fig. 3.1, $B_1 \rightarrow C_1$]; subsequently, the displaced Cu atom hops off the step directly to the lower terrace, a process with an activation barrier of 0.34 eV [Fig. 3.1, $C_1 \rightarrow D_1$]; we refer to this motion as the "assisted exchange" process. Thus, independent of the direction in which the Fe adatom approaches the step edge, there is a unique stable final configuration, shown in Fig. 3.1(d).

A second Fe atom feels even more comfortable embedding in the step next to the first one with the total energy 2.52 eV lower than sitting on the upper edge of the step. Additional Fe atoms approaching the step edge will undergo the same processes, leading to a row of Fe atoms embedded in the Cu step, one lateral lattice constant away from the step edge. This embedded row of Fe atoms has so far escaped experimental detection. However, our study shows that it is an essential part of wire growth.

We next consider the deposition of additional Fe atoms on the surface containing mixed Fe-Cu steps. The likely configurations are shown in Fig. 3.2. Again, an Fe adatom can approach the mixed step from either the upper or lower terrace.

From the upper terrace, configuration A_2 is easily reached, which is energetically stable because of the attraction of the Fe adatom to the basal Fe wire. In contrast, configuration B_2, reached by an Fe adatom approaching from the lower terrace, is energetically very unstable. In analogy to the processes shown in Fig. 3.1, the high energy configuration B_2 will convert into A_2 via two intermediate states C_2 and D_2. Configuration C_2 is reached via a place exchange process, with the Fe adatom taking the place of an edge Cu atom, and the Cu atom displaced up to reside on top of three Fe atoms. Configuration D_2 is reached when the atop Cu atom climbs down the Fe-Cu mixed step. Finally, the $D_2 \rightarrow A_2$ transition is realized via a second assisted process. Based on the relative energies shown in Fig. 3.2, and the detailed calculations for the first phase [Fig. 3.1], we surmise that the kinetic barriers encountered in the overall $B_2 \rightarrow A_2$ transition are all relatively small (up to a few tenths of eV). Therefore, additional deposition of Fe on the surface naturally leads to the growth of an Fe wire on top of the Fe basal wire, with an *apparent* width of only one atom. Further growth of Fe will widen the width of the wire, but the narrowest stable Fe wire is a true one-atom-wide structure residing at the upper edge of the mixed Fe-Cu step.

3.2.3 Discussions

So far we have identified a two-phase kinetic pathway for the formation of an Fe wire at the upper edge of a step on a Cu(111) surface. Next, we attempt to rationalize the preference of the two-phase kinetic pathway for this system based on qualitative considerations of bond strength, bond length, and crystalline structure.

First, the preference of the various motions shown in Figs. 3.1 and 3.2 is tied to the inequality chain in the Fe-Fe, Fe-Cu, and Cu-Cu bond strengths: $U_{Cu-Cu} <$ $U_{Cu-Fe} < U_{Fe-Fe}$, deduced from the melting temperatures $T_m(Fe) = 1811K \gg$
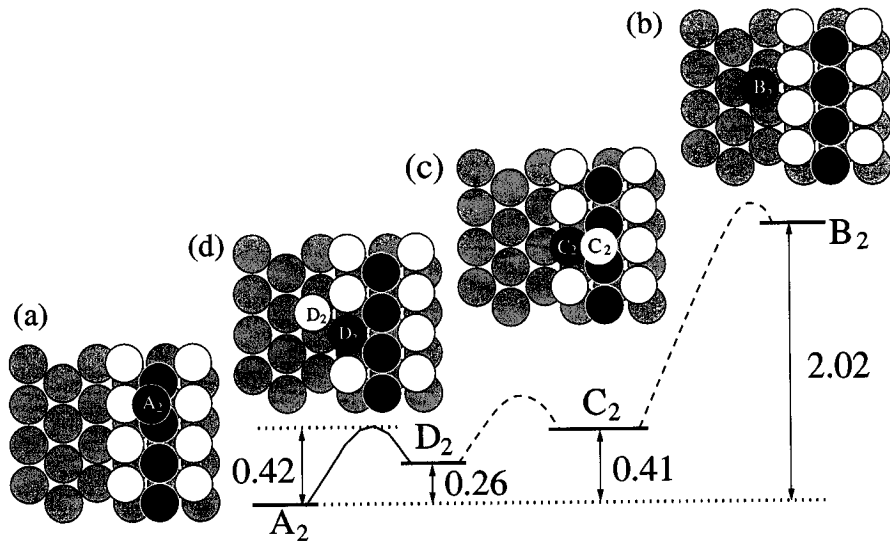
Fig. 3.2: Top view of the second phase of the two-phase kinetic pathway for Fe wire formation on the stepped Cu(111) surface, together with the energy levels and activation barriers(in eV) for different configurations. Dashed lines indicate energies not explicitly calculated. (a) and (b) show the initial configurations reached when an Fe adatom approaches the Fe-Cu mixed step from the upper and lower terrace, respectively. Configuration A_2 is energetically most stable, because of the strong attraction by the buried Fe wire. Configuration B_2 is energetically very unstable, and will convert to configuration A_2 via two intermediate configurations shown in (c) and (d).

$T_m(Cu) = 1358K$. Compared with direct hopping, the exchange processes have lower activation energies because they involve interruption of fewer of the stronger Cu-Fe or Fe-Fe bonds [115].

On the other hand, consideration of pure bond strength alone is insufficient in explaining the structural selection in phase two. Here, both the bond length and the intrinsic crystal structure come into play. This is because of the different nature of the configurations involved in the two phases: The first phase involves Fe *adatoms* on a Cu substrate, dealing with the behavior of individual Fe atoms with a surrounding Cu host. The second phase, with the involvement of the Fe atoms *embedded* in the Cu substrate, deals with Fe atoms in an environment more akin to the crystal structure of

bulk Fe. In the $<011>$ direction of the Cu(111) surface, the nearest Cu-Cu distance is 2.56 Å, while in bcc Fe the nearest Fe-Fe distance in the $<111>$ direction is 2.48 Å. Therefore, the embedded Fe row is only minimally strained by the fcc structure of the Cu substrate. In order for the Fe atoms to regain an environment closer to their preferred bcc crystalline structure, incoming Fe atoms in phase two choose to stay on the upper edge of the step. This avoids undergoing either more embedding of the Fe atoms, which would lead to an extended Fe structure in fcc geometry, or direct hoppings, which would not promote growth of a bcc-like Fe crystal.

To explore the applicability of this two-phase kinetic process to other systems, and in particular, to justify the physical considerations involved in the second phase of the wire formation, we next examine the behavior of Co and W atoms on the same stepped Cu(111) surface.

Because Fe, Co, and W have the same bond strength inequalities when growing on Cu, we expect that the exchange pathways similar to those shown in Fig. 1 should also take place for Co or W, leading to the formation of a row of atoms embedded into the Cu substrate, one lateral lattice constant away from the step edge (phase one). But different expectations from the Fe case arise in phase two. The Co crystal has a hexagonal structure. Its densely packed (0001) surface has exactly the same hexagonal configuration as the (111) surface layer of the Cu substrate. The Co nearest neighbor distance on the (0001) surface is 2.51 Å, which enables the buried Co line to be accommodated at the regular lattice sites of the fcc Cu substrate even better than Fe. Furthermore, additional Co atoms should also be embedded into the Cu substrate as an extension of the Co structure in the hexagonal geometry, thereby doubling the width of the buried Co wire. W, like Fe, prefers a bcc structure, but its nearest neighbor distance in the $<111>$ direction is 2.74 Å, much larger than the
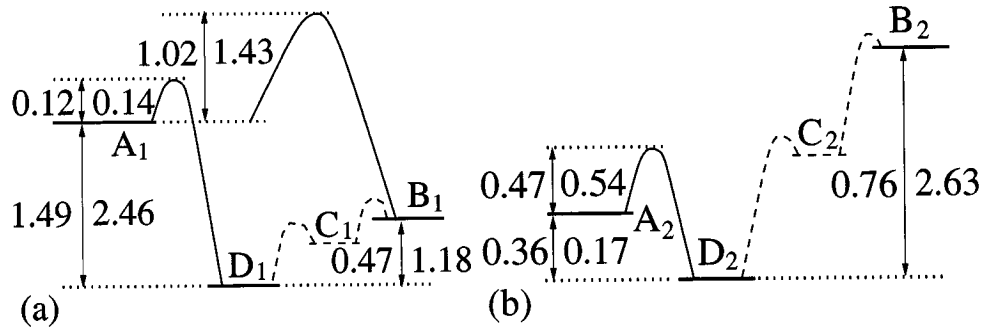
Fig. 3.3: Relative energies and activation energy barriers (in eV) of configurations involved in (a) phase one and (b) phase two of the kinetic pathway for Co (numbers to the left of vertical arrows) and W (numbers to the right). Dashed lines indicate energies not explicitly calculated.

corresponding distance of 2.56 Å for Cu. Therefore, when a row of W atoms are embedded into the Cu substrate, we expect the relaxation of the ensuing strain to lead to buckling of the W row, which would then spoil its alignment with the <111> direction. Additional incoming W atoms should follow the structure of this buckled basal line.

As shown in Fig. 3.3, our detailed calculations confirm these qualitative expectations. In the first phase, when approaching the step from the upper edge as shown in Fig. 3.1(a), both the Co and the W adatom will undergo the exchange pathway to reach the final state D_1. For the initial configuration B_1, which involves a Co or W adatom approaching from the lower terrace, the final state D_1 has a much lower energy (0.47 eV for Co and 1.18 eV for W), ensuring that it is the final stable configuration that can be reached via (assisted) exchange. However, the presence of a basal line in the Cu substrate does not guarantee the formation of a stable wire on top. A detailed examination shows that the embedded Co row is nicely confined in the substrate while the W row buckles to partially recover the bcc structure in

the <011> direction. When additional Co or W adatoms approach the mixed step from the upper edge, they continue to embed into the step via place exchanges. Such processes favor the stabilization of the hexagonal structure of Co or the bcc structure of W. Based on these results, we conclude that the same type of wire as for the Fe case is unlikely to form for either Co or W. Instead, a Co atom wire, sitting on top of two buried rows of Co, is favored, while the case of W is more complex because of buckling.

Finally, we did most of the calculations again with a $3 \times 3 \times 1$ k-point mesh and found that our results are convergent. Furthermore, a nine-layer substrate is used for configurations A_1 and C_1. Results are not changed. For configurations A_2 and B_2, we have also carried out spin-polarized calculations with all-electron methods [116]. These results are shown in Table ?? and they do not alter the central conclusions of the spin-averaged calculations. Spin-polarized calculations may slightly change the detailed configurations of the top wire, but for the kinetic processes and the 1D wires we have focused on, our original calculations give reliable conclusions. Therefore, we expect that growth experiments with carefully controlled Fe coverages should observe the initial burying of the Fe rows, and the subsequent formation of Fe wires of single atom width. Furthermore, our findings suggest the need for a reexamination of conclusions from previous studies of the magnetic properties of Fe wires that have overlooked the necessary existence of the Fe basal line.

3.2.4 Conclusion

In conclusion, our extensive theoretical study of the kinetics of Fe adatoms on the Cu(111) stepped surfaces provides the missing kinetic picture of how Fe nanowires are formed. A hidden Fe basal line under the exposed wire has been identified. The

	2 × 2 × 1k, 6 layers	3 × 3 × 1k, 6 layers	2 × 2 × 1k, 9 layers
B_I - A_I	-1.02	-1.07	—
D_I - A_I	-1.61	-1.62	-1.72
$A_I \to B_I$	1.00	1.11	—
$A_I \to D_I$	0.07	0.05	—

Table 3.1: Results from convergence calculations with more k-points and thicker layers. The configurations A_I - D_I are as shown in Fig. 3.1. Minus means the energy difference, and $\to$ means the energy cost of migration from one configuration to the other. Energies are in unit of eV.

underlying physical reasons for the kinetic pathway are also corroborated by the results of additional calculations for Co and W.

3.2.5   Acknowledgments

This work is done in collaboration with Efthimios Kaxiras and Zhenyu Zhang. We thank Dr. Wenguang Zhu and Dr. Yu Jia for technical helps, and Dr. Jian Shen for helpful discussions related to the experiments. This work was partly supported by NSF (Institute for Theory of Advanced Materials in Information Technology, Grant DMR-0325218, and Grant DMR-0306239), and by ORNL, managed by UT-Battelle, LLC, for the U.S. Department of Energy under Contract No. DE-AC05-00OR22725. The calculations were performed at ORNL's Center for Computational Sciences.

3.3   Formation of monatomic Fe chains on vicinal Cu(111) surfaces: an atomistic view

Uniform arrays of monatomic Fe chains are realized on a vicinal Cu(111) surface with a regular step array. Deposited Fe atoms are first embedded into the

flat Cu(111) terrace at precisely one-atom distance away from the *upper* edge of a monatomic surface step. The resulting Fe wires, in turn, serve as one-dimensional nucleation lines for the formation of monatomic Fe chains along the upper edges of the steps. The present results, obtained by scanning tunneling microscopy (STM) and interpreted with first-principles calculations, unambiguously establish the essential role of embedded Fe atoms as precursor to monatomic wire growth. The Fe wires present an ideal testing ground for exploring ferromagnetism in the one-dimensional limit.

3.3.1 Introduction

Nature, unfortunately, rarely provides us with true 1D model systems. A very intuitive approach toward creating a *quasi* 1D system is to use a stepped surface as a template for atom wire growth. The basic idea is that lattice sites along a step edge are far more reactive than those on top of a flat terrace. Hence, deposited atoms should preferentially adsorb at the step edge, leading to nucleation and growth of an atom chain on the lower terrace, along the step edge. Indeed, quasi 1D metallic atom chains have been fabricated on *e.g.* vicinal silicon surfaces but the metal atoms are generally incorporated into the terraces, not at the step edges, and often form complex surface reconstructions [117, 118, 121]. Step edge decoration appears a more viable approach for metal substrates [53, 105, 122, 123]. For instance, highly uniform monatomic Co chains have been realized via step edge decoration of Pt(997) [122].

The growth of Fe on Cu(111) is a notable exception to the prevailing picture of step edge decoration on metal surfaces. Here, contrary to intuitive expectations, Fe nucleates and grows along the *upper* edges of monatomic steps on vicinal Cu(111) [53, 124] leading to the formation of irregular stripes that are single-monolayer high and

several atoms wide. Since this initial observation, an intensive effort has been devoted toward understanding the surprising occurrence of long-range ferromagnetism in such quasi 1D systems [107, 108, 125, 126], but to date the major limitation has been the lack of knowledge on the precise atomic structure as well as the formation mechanism of the Fe wires.

Very recently, density functional theory (DFT) calculations indicated a novel kinetic pathway toward the formation of single-atom-wide Fe wires on a stepped Cu(111) surface [127]. It was predicted that Fe atoms should be incorporated into the upper terrace via an intricate exchange process. In this process, Cu step edge atoms are initially displaced by the incoming Fe atoms but remain located at the lower edge of the step. This is the energetically preferred and kinetically most accessible configuration, regardless of whether the Fe adatom approaches the step edge from the upper or lower terrace. Accordingly, the embedded Fe atoms are located one lattice constant away from the step edge. It was furthermore predicted that embedded Fe atom will capture other diffusing adatoms, thus providing an elegant explanation for the upper step edge decoration seen in experiment. It should be noted, however, that the experiments employed a rather high coverage of Fe [53, 124]. Consequently, the embedded or hidden Fe wire, if present, would have escaped experimental detection. A convincing demonstration of the existence of the embedded atom wire is indispensable for achieving microscopic understanding of the 1D ferromagnetism from first-principles.

3.3.2 Experimental results

In this Letter, we report on the first experimental realization of monatomic Fe chains on a vicinal Cu(111) substrate. Detailed STM investigations not only confirm

the theoretically predicted [127] pathway involving the initial embedding and subsequent trapping of atop Fe atoms, but also elucidate a remarkable wire uniformity that only appears to be affected by the terrace size distribution of the vicinal substrate. The results represent a significant advance from a growth science perspective, leading to near perfect control of shape and uniformity. Furthermore, the highly ordered monatomic Fe wires in a non-magnetic matrix as achieved here in principle provide an ideal testing ground for exploring magnetism in the 1D limit.

Experiments were performed in an Omicron ultra high vacuum variable temperature STM. We used a nominally flat Cu(111) crystal and a vicinal Cu(111) substrate having a miscut by $4°$ toward $[11\bar{2}]$ direction. The crystals were cleaned in situ by repeated cycles of Ne^+-ion sputtering and annealing at $\sim 500°C$. The cleanliness of the surfaces was confirmed by low-energy electron diffraction and STM. Fe atoms were dosed onto a cold substrate (120 K) using an e-beam evaporator. The Fe flux was stabilized at ~ 0.05 monolayer per minute (ML/min). Following the Fe deposition, the sample slowly warmed to room temperature (RT) and was subsequently transferred onto a variable temperature STM stage.

Figure 3.4 shows a nominally flat Cu(111) surface with monatomic steps decorated by Fe. The Fe atoms line up along the upper edge of the step, forming continuous Fe nanowires with a rather uniform thickness. At low coverage, Fe atoms all nucleate along the upper step edge, forming a line of Fe atoms which protrude ~ 2 Å above the upper terrace, as shown by the line profile in Fig. 3.4 (a). The Cu(111) terraces are atomically flat and there is no sign of Fe nucleation on the terraces. With increasing coverage, the Fe wires along the step edge continue to grow to a height of about ~ 5 Å, after which Fe also starts to nucleate on the terraces, as shown in Fig. 3.4 (b). Evidently, there is a reasonably broad coverage window where Fe atoms
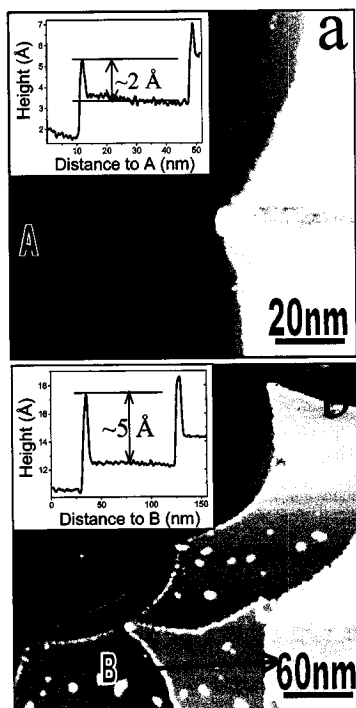
Fig. 3.4: STM images of Fe on Cu(111) with different nominal coverages (a) 0.03 ML and (b) 0.10 ML. The inset shows the line profiles of the nanowires across the step edges as indicated in the topographic images (by J. Guo and H. H. Weitering).

exclusively nucleate along the step edge. This indicates the possibility of growing atomic Fe wires along the step edges in a highly controlled manner.

Next, we explore the feasibility of creating long and straight nanowires along the edges of a vicinal crystal. Fig. 3.5 (a) shows an STM image of the clean vicinal substrate. The line profile indicates monatomic steps ($\sim$2.08Å) with sufficiently regular spacing between the steps. The average terrace width is $\sim$ 3 nm ($\sim$ 14 terrace atoms), consistent with the nominal miscut angle of 4 degrees. The imaging noise at the step edges originates from the fast kink diffusion on Cu(111) at RT [128]. Fig. 3.5 (b) shows a derivative image of the vicinal Cu(111) surface after depositing $\sim$0.07 ML of Fe. The image reveals a set of parallel, ultra thin Fe nanowires with
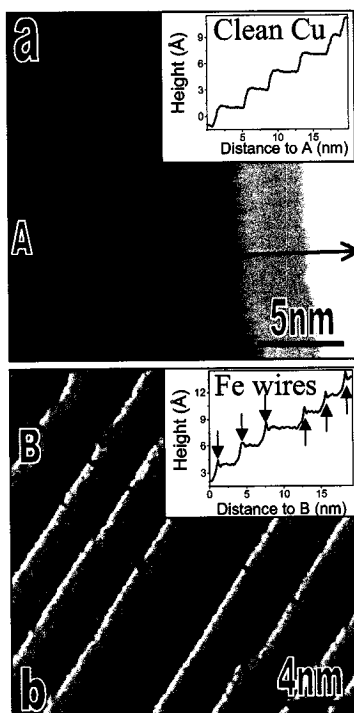
Fig. 3.5: STM images (+30 mV/10 nA) of (a) clean vicinal Cu(111) surface at RT and (b) a Fe nanowire array on the vicinal Cu(111) surface at 60 K. The image in (b) is the first derivative of the topographic image. Insets (both from original images): line profiles showing the existence of monatomic steps on the surface. Arrows in (b) point toward small spikes in the step profile and indicate the presence of embedded Fe atom wires along the upper edges of the steps. (by J. Guo and H. H. Weitering)

uniform thickness, orientation, and separation (~3 nm). The presence of Fe is also confirmed by the step line profiles, which consistently show a spike at the upper edge of every step; this spike is absent on the clean surface. From these line profiles, we can estimate the height and width of the atom wires: they are about ~4 Å wide and protrude about ~0.4 Å above the upper terrace. The image contrast is not only influenced by the local topography and electronic structure of the steps, but also by the shape of the W tip, especially at the step edges since the step height of W is comparable to that of Cu along the [111] direction (2.7 Å for W and 2.1 Å for Cu).

Considering the fact that these protruding features are heavily convoluted by the structure and electronic structure of the STM tip, it is likely that these wires are indeed single atom wires. In particular, the $\sim$0.4 Å protrusion of such wires strongly suggests that they are embedded into the upper edge.

The formation mechanism of these atop wires can be elucidated by tracing the configuration from the very initial stage. Fig. 3.6 (a) is a close-up atomic resolution image of the Fe decorated step edge, recorded at RT. The atomic resolution on the terrace allows us to precisely indicate the location of the Cu atom rows in the line profile of the step. The Cu rows are indicated by the vertical grid lines in the line profile diagram. The step edge appears rather blurred; the width of this blurred region is about two atom rows, as indicated by the shaded bar in the line profile diagram. Such blurring at a step edge is not unusual and could be due to the combined effects of tip shape, scanning, and/or kink diffusion. Attempts to obtain sharper images at low temperature were not successful. The region of bright contrast, presumably indicating the location of the Fe atoms [129], is clearly displaced away from the actual step edge. A visual inspection of the bright region in the topographic image may suggest that it is two atom rows wide. The line profile in Fig. 3 (a), however, does show a distinct maximum at a location that is approximately two atomic distances away from the blurred step edge region. Its height protrudes at most 0.3 Å above the upper terrace [130]. Atoms that are located right at the step edge (*i.e.*, indicated as the first row in the line profile diagram), appear to be at exactly the same height level as the Cu atoms on the flat upper terrace, suggesting that they are Cu atoms. The 0.3 Å protrusion in the second row is too small for an atop adsorbate. Instead, these observations [see also Fig. 3.5 (b)] are fully consistent with the possibility of an embedded Fe atom, located at one atom distances away

from the step edge. However, since the contrast in STM contains both geometrical and electronic contributions, and specifically contributions from the modified charge density near a step edge, we must verify the origin of the contrast, as done below based on first-principles calculations.
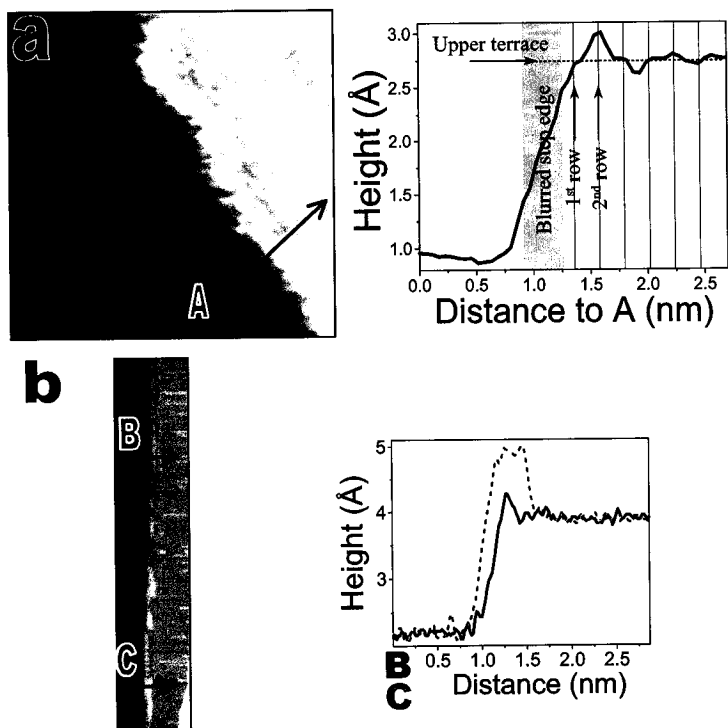
Fig. 3.6: (a) Close-up view STM image (7 nm × 7 nm,+1 V/5 nA) of a decorated Cu(111) step. The line profile on the right is an average of 10 line scans at different locations across the step edge. The vertical grid lines indicate the locations of the atoms in the upper terrace. The shaded zone corresponds to the blurred region in the STM topographic image. (b) STM image (4 nm × 20 nm, +1 V/3 nA) of the decorated step edge for higher Fe coverage. Additional Fe atoms are attached to the upper edge of the step, thus enhancing the vertical corrugation. Line profiles B and C correspond to embedded Fe and atop Fe, respectively. (by J. Guo and H. H. Weitering)

Figure 3.6 (b) shows an image of a decorated step edge at a coverage slightly higher ($\sim$0.10 ML) than that of Fig. 3.5 (b). The thickness and height of the wires is no longer uniform. The line profiles clearly distinguish between embedded Fe atoms (line profile along B) and atop Fe atoms (line profile along C). These observations

are fully consistent with a scenario where the embedded Fe atoms trap additional atoms, which nucleate into an atop wire or an attached nanowire.

3.3.3 Theoretical STM simulations and discussions

In order to elucidate the nature of the step edge contrast, we simulated the STM images and line profiles using DFT for different step geometries. The DFT results are obtained with the VASP code [39], using the Perdew-Wang 1991 version of the generalized gradient approximation (PW91-GGA) [110]. Computational details and convergence checks are the same as those in Ref. [127]. For the STM image simulations, we used the Tersoff Hamann method [131] for a 6-layer Cu slab with 144 atoms. Each terrace is 4x4 atoms in size. The bottom three layers are fixed at their respective bulk positions during the relaxation. A $4 \times 2 \times 1$ mesh in the Brillouin zone of the supercell is used to sample the reciprocal space. The vacuum region separating slabs is equal to 10 Å.

Simulated STM images of the decorated step edges for the three step geometries considered in Ref. [127] are shown in Figs. 3.7(a-c). To further determine whether the Fe wire is truly embedded away from the step edge, we also simulated the STM image for Fe atom locations at the lower edge of the step [Fig. 3.7 (d)]. The clean Cu step shown in Fig. 3.5 (a), the "buried"wire in Fig. 3.6 (a), and the "attached"wire in Fig. 3.6 (b) are nicely reproduced in Figs. 3.7 (a-c), respectively. On the other hand, the distinction between Figs. 3.7 (b) and (d) requires special consideration. In both cases, there is a clear charge density protrusion at the location of the Fe atoms. However, compared to Fig. 3.7 (d), Fig. 3.7 (b) shows a small shoulder left to the Fe row, due to the presence of a Cu atom at the lower edge of the step. This shoulder is apparent in the line scan shown in Fig. 3.6 (a). Also, the pronounced dip

Distance perpendicular to the step (nm)
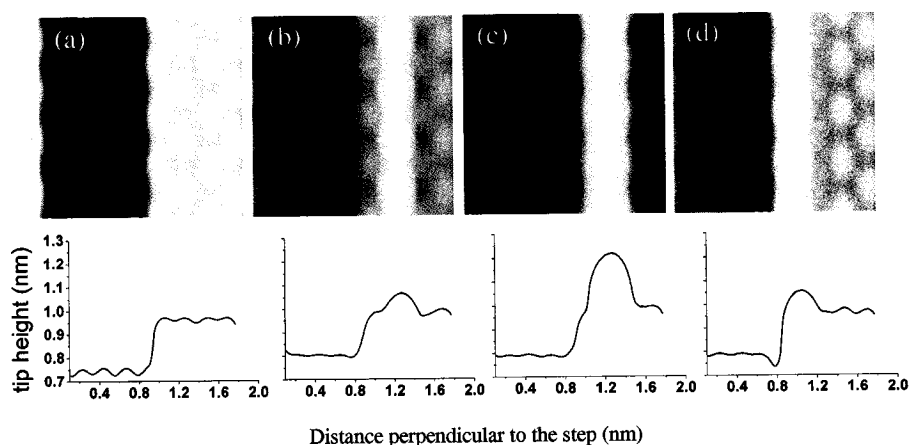
Fig. 3.7: Upper panel: simulated STM images for (a) a Cu(111) step, (b) a Cu(111) step with one row of Fe atoms embedded one lattice constant away from the step edge, (c) same as (b) except for the addition of an atop Fe wire, and (d) a Cu(111) step with one row of Fe atoms terminating the step. Lower panel: averaged tip height profiles for the corresponding configurations shown in the upper panels. These profiles are plotted along the direction perpendicular to the step and are averaged over 70 different line scans.

in the charge density contour at the location of the lower step edge in Fig. 3.7(d) is not present either in Fig. 3.7(b) or in experiment. The combined experimental and theoretical results thus overwhelmingly support the picture of initial embedding and subsequent attachment of monatomic Fe wires.

As an indication of the general nature of this new and intriguing growth concept, we have carried out first-principles calculations on the energetics and kinetics of different types of metal adatoms (Co, Cu, and Zn) on vicinal Cu(111) with the monatomic Fe wires embedded one lattice constant away from the step edges. We find that the atop position is at least a local energy minimum, regardless of the type of the adatoms. In particular, it is energetically most favorable for Co to reside on top of the embedded Fe wires, thereby opening the possibility of forming a well-ordered Co-Fe wire. Therefore, the Cu(111) stepped surfaces containing embedded Fe wires can be used as ideal templates for tailoring metal alloy wires with tunable

chemical compositions and potentially intriguing magnetic and transport properties.

Before closing, we note that the enhanced stability of the embedded monatomic Fe wires might be attributed to the passivation and protection of the otherwise more reactive Fe atoms by the outer lines of Cu atoms. Specifically, the mechanism of embedding and passivation during the formation of the first Fe wire can be viewed as the 1D analog of related processes in 2D, in which an Fe or Co layer grown on Cu(100) is buried by an inert Cu layer upon annealing [132, 133, 134]. Precisely how the passivation modifies the magnetic properties of the embedded Fe wire remains a challenging issue for future studies.

It is also worthy of attention that under the same experimental conditions, the Fe wire formation processes take place even at very rough steps, which clearly indicates that the shape of the steps is not playing a role in the wire formation; instead the interaction between the Fe adatoms and the close packed Cu(111) surface is essential, as will be seen in the next section's study. Fig. 3.8 is an STM image of an Fe nanowire (in bright yellow) wandering along the rugged step edges.

3.3.4 Conclusions

In summary, arrays of monatomic Fe chains have been realized using a vicinal Cu(111) surface with a regular step array. Detailed STM investigations aided by DFT calculations firmly establish the initial embedding of Fe into the upper terrace and the subsequent trapping of atop Fe atoms, resulting in the formation of long atom wires along the upper edges of the steps. The atom wires are remarkably uniform and in principle present an ideal testing ground for exploring one-dimensional magnetism from first principles.
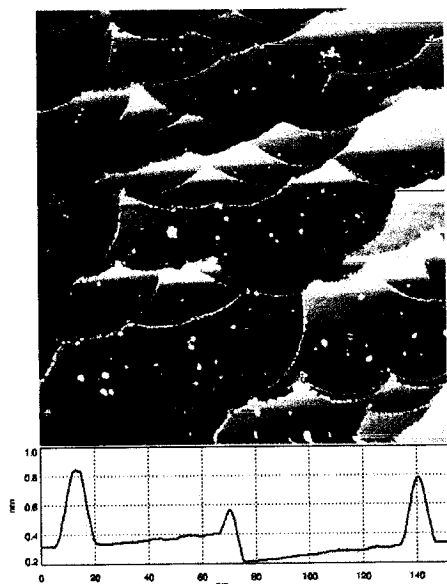
Fig. 3.8: STM image of Fe nanowires on clean Cu(111) surfaces with irregular steps. The size of the image in reality is 500 nm × 500 nm. The bright yellow shows where the Fe atoms are. (by J. Guo and H. H. Weitering)

3.3.5 Acknowledgments

3.4   Step-edge barriers and nanowire growth on transition-metal surfaces

The activation barriers for adatom motion on terraces and across steps play an essential role in determining the growth morphology of surfaces. We consider a series of adatoms on representative transition metal surfaces and demonstrate, through extensive first-principles calculations, a clear correlation between the step-edge barriers and the the relative adatom-vs.-substrate electronic shell filling. An approximate linear relation links the adatom surface binding energy to the hopping energy barrier. Our results form the basis for predicting, through simple rules, the character of surface growth in low-dimensional hetero-epitaxial systems such as nanowires.

3.4.1   Introduction

Epitaxial growth continues to attract great interest as an effective approach for producing nanostructures with desired properties [135, 136, 137]. A variation on the general theme of epitaxy is the formation of self-assembled nanowires at step edges where strikingly self-regulated growth is observed [53, 103, 104, 105, 106]. These nanowires, composed of atoms different than the substrate (hetero-epitaxial), represent an attractive realization of the long sought one-dimensional, atom-wide structures, that can serve as a template for fundamental studies of electronic and magnetic behavior in low dimensional systems. The key parameter that controls the nature of this growth is the difference between the activation energy barrier for diffusion along the terrace, ε_t, and diffusion across a step edge, ε_{se}, the so-called Ehrlich-Schwoebel (ES) barrier [138, 139]: $\varepsilon_{ES} = \varepsilon_{se} - \varepsilon_t$ (see Fig. 3.9). A small or non-existent ES bar-

rier favors layer by layer growth, while a large one leads initially to two-dimensional fractal islands and later to three-dimensional island growth. While these notions are well established and describe satisfactorily homo-epitaxial growth [140], a far more complex picture emerges in the case of hetero-epitaxial nanowires.

Adatoms on surfaces can migrate from the upper to the lower side of a step through either a hopping or an exchange process [141, 142] (see Fig. 3.9). The step-edge activation energy is the lower of the two energy barriers corresponding to hopping or exchange. Accordingly, the ES barrier in different cases may originate from different processes. In *homo*-epitaxial growth, either process leads to the same surface morphology after the adatom has diffused from the upper to the lower side of the step. In the case of *hetero*-epitaxial growth, the two processes result in different configurations: the hopping process places the hetero-adatom at a site of the lower step edge, protruding from the step (Fig. 3.9(B)); the exchange leaves the hetero-adatom at the step edge and a substrate atom protrudes onto the lower side of the step (Fig. 3.9(C)). Therefore, the value of the ES barrier alone does not fully describe the relevant physical processes; the mechanism for diffusion across the step edge must also be identified. Repeated hopping or exchange events will lead to either a row of atoms decorating the lower step edge [104], or a wire embedded within the step, one atom away from the step edge [143]. Both processes produce stable, one-dimensional, atom-wide wires that are well suited for the study of low-dimensional physics. It is, however, not possible to predict from simple considerations which process dominates and why.
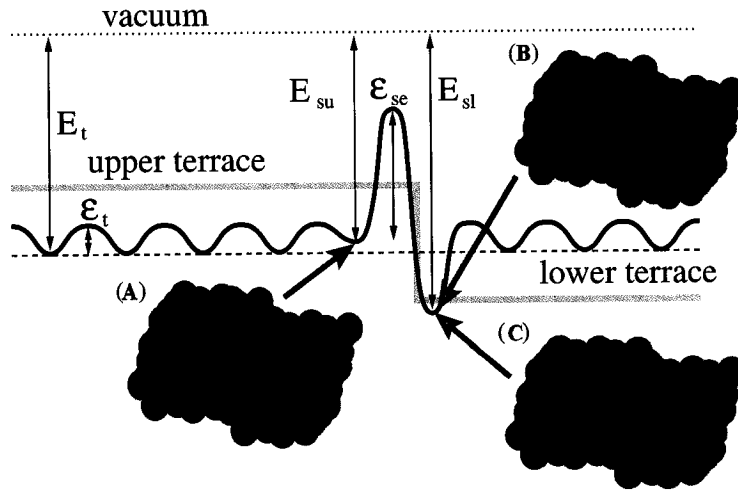
Fig. 3.9: Energetics and atomic structures for adatom (green sphere) motion across a surface step: (A) is the initial configuration with adatom at the upper side of the step; (B) and (C) are final configurations from a hopping and an exchange process. The relevant binding energies (E_t, E_{su}, E_{sl}) and energy barriers $\varepsilon_{se}, \varepsilon_t$ are also indicated (see text).

3.4.2 Results

In this Letter we study theoretically the nature of ES barriers on stepped transition-metal surfaces through systematic investigation of the energetics (total energies and binding energies) and kinetics (terrace diffusion barriers, step-edge hopping and exchange barriers). We considered two sets of adatoms on two stepped transition-metal surfaces: Fe, Co, Cu, and Zn adatoms on the Cu(111) surface, and Rh, Pd, and Ag adatoms on the Pd(111) surface. We chose these systems for two reasons: First, the Cu and Pd (111) surfaces are close-packed and have electronic densities that resemble a two-dimensional free-electron system with the steps acting as the prototypical one-dimensional defects. Second, the adatoms in each case are elements in the same row of the periodic table as the substrate atoms, thus of similar size, which minimizes strain effects. This set up is designed to bring out electronic effects in systems that

are close to simple, idealized models (like the jellium surface), but at the same time are realistic since some of them have been studied experimentally.

We find that the ES barriers are only slightly different from the corresponding step-edge barriers, because the terrace diffusion barriers for all systems we studied are much smaller than the step-edge barriers. We also find that the step-edge barriers display simple trends and are correlated with the electronic structure of the adatoms in reference to the substrate atoms. We provide evidence that hopping barriers scale roughly linearly with binding energies of the adatoms on the terraces. These results constitute a useful guide for designing and controlling the growth of self-assembled nanostructures on surfaces, using simple rules based on intuitive arguments.

Our investigation is based on first-principles calculations in the context of density functional theory, employing VASP [39] with the generalized gradient approximation (GGA) [110] for exchange-correlation effects and ultrasoft pseudopotentials to represent the atomic cores [73]. The Fermi-level smearing approach of Methfessel and Paxton [36] is used for the electronic states near the Fermi level, with a Gaussian width of 0.2 eV. We use the nudged elastic band method (NEB) [111], followed by spline interpolation, to determine the diffusion pathways and energy barriers. We model the stepped surfaces by a slab miscut along the (322) direction, consisting of (111) terraces of width five lateral lattice constants separated by A-type steps of monatomic height [114] (we expect trends to be similar on B-type steps). Computational parameters where chosen to ensure that all quantities of interest are well converged and accurate [144].

We turn next to the discussion of diffusion barriers for specific cases. The preferred adsorption sites of the adatoms on the stepped Cu(111) and Pd(111) surfaces are the fcc sites, whether they are in the central region of the terrace or in the imme-

diate vicinity of the step, either on the upper side (Fig. 3.9(A)) or in the lower side after hopping (Fig. 3.9(B)) or exchange (Fig. 3.9(C)). We will take configuration (A) as the reference state for relative energies. The energy of configurations (B) and (C) relative to that of (A) for the various systems we considered, and the corresponding hopping and exchange barriers are presented in Fig. 3.10.
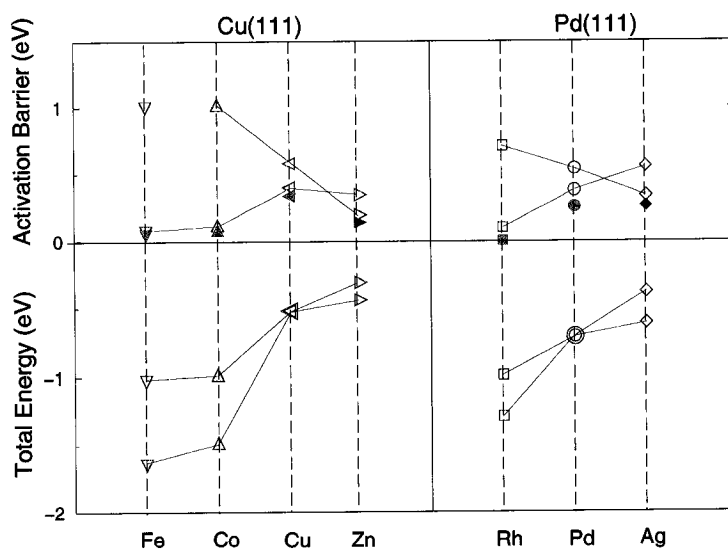
Fig. 3.10: Lower panel: total energy E_B, E_C of configurations (B)–red open symbols, and (C)–blue open symbols, relative to that of (A). Upper panel: energy barriers ε_{hop} for hopping from (A) to (B)–red open symbols, and ε_{ex} for exchange from (A) to (C)–blue open symbols. The filled symbols are the corresponding ES barriers in each case (the lowest of the hopping or exchange barriers minus the terrace diffusion barrier).

Certain clear trends emerge from these results. First, for all adatoms on Cu(111) or Pd(111), configurations (B) and (C) have lower energies than (A) and thus are more stable. On each substrate, the magnitudes of E_B and E_C decrease with increasing atomic number of the adatom (left to right in Fig. 3.10). For adatoms to the left of the substrate element $E_C < E_B$, indicating that (C) is the most stable configuration; for adatoms to the right of the substrate element the reverse is true, that is, $E_B < E_C$, with (B) being the most stable configuration. The activation

substrate	Cu(111)				Pd(111)		
adatom	Fe	Co	Cu	Zn	Rh	Pd	Ag
ε_t	0.03	0.04	0.06	0.05	0.10	0.12	0.08
ε_{ES}	0.05	0.08	0.34	0.14	0.00	0.26	0.26
Mechanism	exc	exc	exc	hop	exc	exc	hop

Table 3.2: The values (in eV) of terrace diffusion barrier ε_t and ES barrier ε_{ES} for different adatoms on Cu(111) stepped surface and Pd(111) surface; the preferred mechanism for step-down motion (exc: exchange, hop: hopping) is also identified in each case.

energy barriers show that the most stable configurations can be easily reached since they involve small barriers. For both substrates, the direct hopping barriers from (A) to (B) (ε_{hop}) decrease with increasing atomic number of the adatom, while the exchange barriers from (A) to (C) (ε_{ex}) increase. Comparing the relative magnitudes of the hopping and exchange barriers for each adatom, we find that for adatoms to the left of (including) the substrate element, $\varepsilon_{ex} < \varepsilon_{hop}$, namely the exchange process is preferred; for adatoms to the right of the substrate element, ε_{hop} is smaller, that is, the hopping process is preferred. The values of ES barriers, ε_{ES} are all relatively small (less than 0.5 eV, see Table 3.2).

To elucidate the origin of the trends revealed above, we analyze the electronic interactions between the adatoms and the substrates by examining charge transfer effects that characterize the adatom/substrate binding strength. This is defined as the charge density difference between the system with the adatom on the one hand, and that consisting of the substrate alone (with the same structure as when the adatom is present) and the isolated adatom, on the other. The results are shown in Fig. 3, on a plane that contains the adatom and its nearest neighbor substrate atoms at the step. As is evident from this figure, electronic charge accumulates between the adatom and its nearest-neighbor substrate atoms; this is typically interpreted as

evidence of bonding between these atoms. The strength of these bonds, measured by the amount of charge transfer, follows the same trend as the energy barriers for hopping. This is a sensible result, since hopping down from the upper to the lower side of the step edge breaks the "bonds" (in a general sense) between the adatoms and their nearest-neighbor substrate atoms. The stronger these bonds are, the larger the energy cost to break them, or equivalently, the larger the hopping energy barrier.
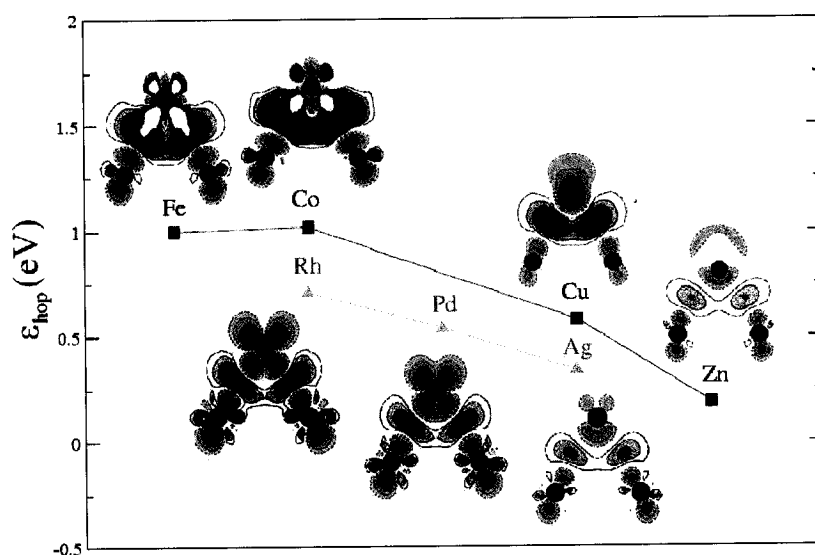
Fig. 3.11: Charge transfer between the adatom and its nearest neighbors for the Cu(111) (upper curve and contours) and Pd(111) (lower) substrates. Red and blue contours correspond to accumulation and depletion of electronic charge, respectively. The points indicate the values of the hopping energy barrier (lines are guides to the eye).

The trend in bonding strength revealed by the charge transfer analysis can also be used to interpret the trends in total energies and in exchange barriers. The adatom should prefer the embedded configuration (C) (see Fig. 3.9) when bonding to substrate atoms is strong, but should favor configuration (B) when bonding is weak. This is consistent with the total energy differences we have found: For adatoms to the left of the substrate element, which show strong bonding to substrate atoms, E_C

$< E_B$, while for adatoms to the right of the substrate element which show weaker bonding, $E_B < E_C$. Note that for adatoms which are the same as the substrate atoms $E_B = E_C$ by definition; the charge transfer in this case can be used as the reference point for defining the strength of adatom-substrate bonding relative to that between substrate atoms. Finally, the barrier for exchange for those adatoms that are strongly bonded to the substrate atoms should be smaller than for those that are weakly bonded, because exchange involves maintaining of the adatom-substrate interaction and breaking of the interaction between the substrate atoms. Equivalently, the hopping process should show opposite trends relative to the exchange process according to the variation of the adatom-substrate bond strength. These features are reproduced by the results of Fig. 3.11. The picture of hopping and exchange barriers and of relative energies is consistent with a simplified bond counting approach[146], emerging here from detailed analysis of the electronic structure calculations rather than from empirical considerations.

Additional insight can be gained by considering the relation between the step-edge hopping barriers and the adatom terrace binding energies, defined as the total energy difference between the isolated adatom and a clean surface on the one hand, and the adatom at its equilibrium configuration on the substrate on the other. For each adatom and substrate, we considered separately the hopping barrier from the upper to the lower step edge (step down motion) and the reverse process (step up motion). The results of these calculations are shown in Fig. 3.12. In all cases, the energy barrier for hopping scales with the terrace binding energy, and to a reasonable approximation the relation is linear. This is consistent with the preceding analysis which was based on the strength of adatom-substrate bonding as revealed by charge transfer effects. What is intriguing is that the relation between hopping energy
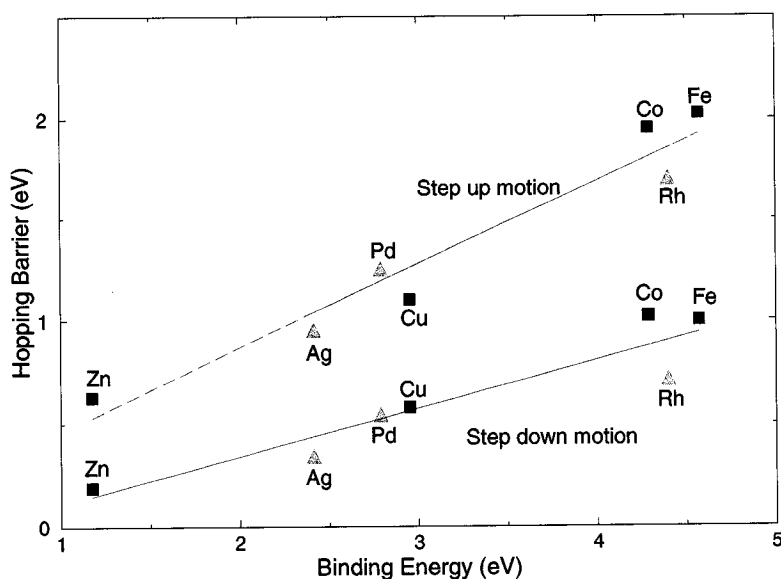
Fig. 3.12: Step edge activation barriers as a function of adatom binding energies for the various adatoms at the upper step edge hopping down (step down motion) and at the lower step edge hoping up (step up motion), for the Cu(111) and Pd(111) substrates. Lines are linear fits to the calculated values shown by points; Purple square and orange triangle symbols represent events on Cu(111) and Pd(111) stepped surfaces, respectively.

barriers and adatom binding energy is linear, and that the slope is roughly the same for the two substrates (all results are approximately captured by the same line). The slopes are different for the two different processes, ~ 0.23 for step down motion and ~ 0.41 for step up motion. Similar linear relations were found for terrace diffusion of non-metal atoms and molecules on transition-metal surfaces [147]. We do not find the same linear relation between the terrace diffusion barriers and binding energies here, most likely because the terrace diffusion barriers on the close packed (111) surfaces are so small.

The linear relation in Fig. 3.12 generally cannot be extrapolated to other elements that are not located in the vicinity of the substrate element in the periodic table. Extensive calculations for W, Al, and Ga adatoms on the same stepped

Cu(111) substrate show that barriers for step down motion and the terrace binding energies for these elements do not fit the simple linear relation for the Fe, Co, Cu and Zn adatoms. This is not surprising, since for elements that are distant from the substrate element, effects of different nature than those considered here, for instance strain, can play an important role. However, a more extended study that takes into account such effects may also reveal simple relations between hopping energy barriers and adatom binding energies.

3.4.3 Discussions

One direct application of this study is to facilitate designing of low-dimensional nanostructure growth on stepped surfaces. For the adatoms and substrates we considered, knowing the adatom terrace binding energy, which can be experimentally measured, allows the estimation of the step edge hopping barrier, and consequently the prediction of the adatom step edge behaviors. Systems (adatom plus substrate) of similar nature should fit in the picture that Fig. 4 presents and extended knowledge that may assist experimental surface growth could be obtained. When generalized to the situation that more adatoms are approaching the step edge, following the process the first adatom takes, nanowires decorating the steps, either at the lower step edge (the result of hopping) or embedded in the step (the result of exchange), will be formed. In fact, the Fe embedded wire on Cu(111), belonging to the latter category, has been recently realized experimentally [143]. We also predict that under control, growth of Co embedded wire should be feasible. Furthermore, these single wire decorated new substrate may provide template for alloy wire growth when a third type of adatoms are deposited subsequently.

3.4.4 Conclusion

In conclusion, we studied the behavior of adatoms at step edges on the Cu(111) and Pd(111) surfaces. Well defined trends were found in adatom step edge hopping barriers and exchange barriers which can be readily interpreted in terms of the electronic interactions between the adatom and the substrate. We find that for a set adatoms on the same substrate, the magnitude of step edge hopping barriers relative to the terrace binding energies can be described by a simple linear relation. Our study elucidates the mechanisms of low dimensional wire formation on stepped surfaces. We hope that these results can assist designing and manufacturing of low-dimensional (alloy) wires with interesting electronic and magnetic properties.

3.5 Acknowledgments

Chapter 4

Semiconducting Cyanide–Transition-metal Nanotubes

82
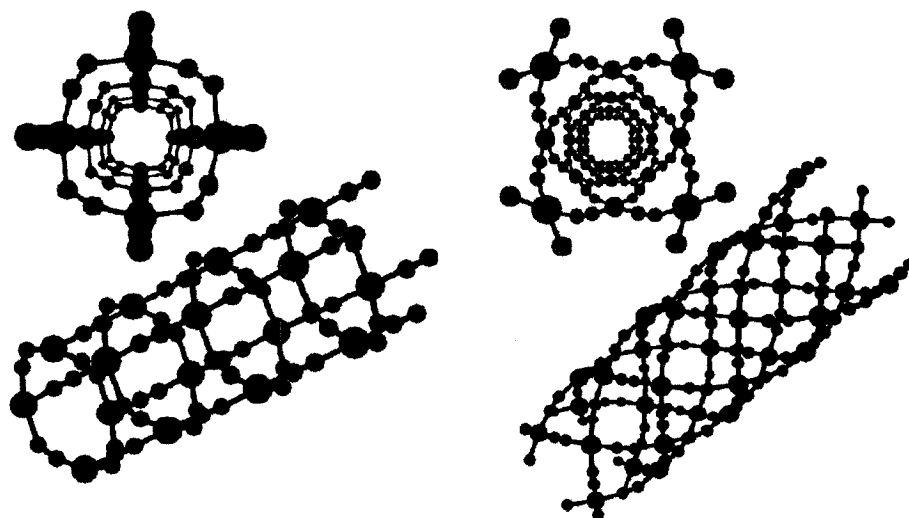
4.1 Overview

The official discovery of carbon nanotubes in 1991 started a new page in the field of nanotechnology. This new form of an old material, graphene, raised wide interests of the whole world. The amazing features these nanotubes made them promising materials in numerous applications. First of all, carbon nanotubes are one-dimensional systems. It provides a rare opportunity for experimental research on one-dimensional systems. Secondly, their mechanical property is unexpctly good: the material is stronger than diamond but much easier to obtain; compared to materials composed of other elements, it is very light weighted. This feature makes the carbon nanotubes ideal building blocks for devices working at extreme conditions, like space crafts. Thirdly, carbon nanotubes can either be metallic or semiconducting. The transport property of a carbon nanotube in theory should be super with extremely high conductivity, which would find its application in nano-electronic-devices. The semiconducting nanotubes can potentially be used in transistors. The size of these tubes convinced people that their application in the semiconducting industry would upgrade the whole field. The possibility of hydrogen storage, drug delivery, DNA sequencing with carbon nanotubes have been explored as well. The realization of this third aspect application of carbon nanotubes have been the most attractive and guided the majority of effort in research.

However, after more than 25 years of research, we still have not seen carbon nanotubes being used much in industry. The society has mostly agreed that using carbon nanotubes for hydrogen storage is most likely a science fiction. The validity of other applications in semiconducting and pharmaceutical industries is still pending. The problem lies in the fact that these applications are all making use of the electronic properties of the carbon nanotubes, which is decided by the symmetry of the tubes

and uncontrollable during manufacturing. The inability to mass-produce carbon nanotubes with uniform electronic properties holds them back in the laboratories.

People seek the solutions to the problem in two ways. One concentrates on looking for experimental techniques that can selectively, and repeatedly produce carbon nanotubes with one particular electronic property. The other search for alternative materials that resemble carbon nanotubes in structure and properties but are easier in manufacturing. Progress has been made in both directions; but in the latter it has been more successful since there has been more free space for development. Researchers have been redirected to understand more about nanowires and designing and generating new nanotubes.

In this chapter, we propose a new type of structurally simple and energetically stable cyanide–transition-metal nanotubes, based on the planar structure of $M(CN)_2$, (M = Ni, Pd, Pt). These nanotubes have semiconducting character with large band gap ($\sim 2 - 3$ eV) which is insensitive to chirality and diameter. We study the energetic, electronic, and mechanical properties of these materials in both planar and tubular forms through first-principles density functional theory calculations. The calculations reveal interesting multi-center bonding features which should lead to preferential growth of tubes of a particular chirality. These intrinsically semiconducting nanotubes can be readily p-doped or n-doped, which makes them good candidates for nanoscale elements in electronic devices.

The special role the four-coordinated Pd atoms played in the center of a square inspired us to inspect the structure of the $SnSe_4Pd/Sn_2Se_6Pd$ pore structure. These nanopores have been experimentally realized. They were reported to have hexagonal structures consisting of honeycomb arrays of parallel pore tunnels. Their high surface areas would allow separation of solutes and assist chemical catalytic processes

and reactions. However, the structures of these nanopores remain mystery. Some preliminary results on our investigation of the problem will be shown in Appendix.

4.2 Introduction

The discovery of carbon nanotubes (CNTs) [148] has given birth to an entire field devoted to the study of these one-dimensional (1D) nano-scale structures that exhibit extraordinary properties and promise for applications. For instance, single wall carbon nanotubes have been reported to show Luttinger liquid behavior [149] and proximity-induced superconductivity [150]. The electronic properties of a carbon nanotube are fully determined by its chirality and can range from metallic to semiconducting. Control of the nanotube chirality and diameter during growth is difficult and presents a major obstacle to mass production of nanotubes with desired properties. To overcome this limitation, boron-nitride nanotubes (BNTs), which have properties less sensitive to chirality, were proposed theoretically [151] and later realized experimentally [152].

In this chapter we propose a new type of structurally simple and energetically stable nanotubes consisting of transition metals and cyanide units. In order to examine the structural and electronic properties of the cyanide compounds and nanotubes, we employ density functional theory (DFT) as implemented in VASP [39, 153, 154], with computational parameters that ensure high accuracy[155]. We find that the cyanide–transition-metal nanotubes are semiconductors with large band gaps ($\sim 2 - 3$ eV), and that their chirality affects the electronic band gap only marginally. The nature of bonding in these systems suggests that tubes of a particular chirality will be energetically more stable, leading to a natural self-selection of tubes with well-defined
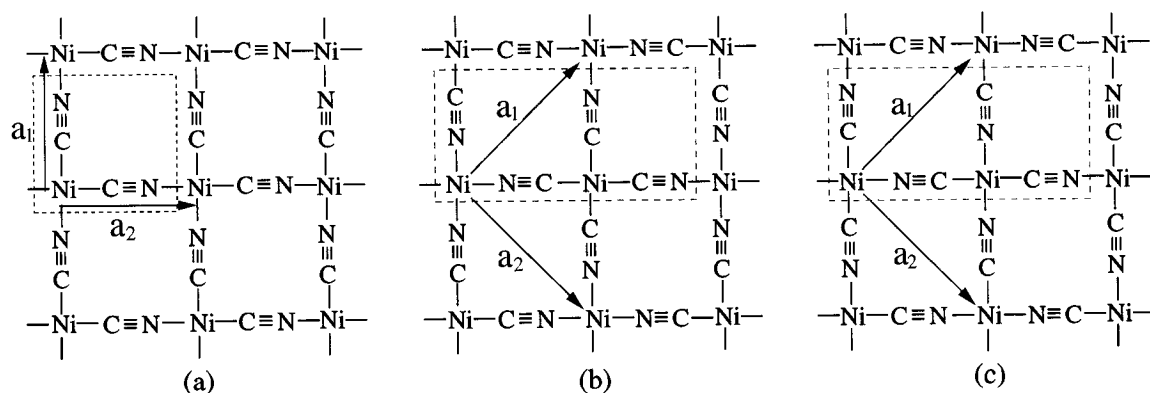
Fig. 4.1: The three types of Ni(CN)$_2$ sheet (the Ni atoms can be replaced by Pd or Pt atoms for Pd(CN)$_2$ or Pt(CN)$_2$ sheet) with the corresponding primitive lattice vectors a_1, a_2, and atomic basis (enclosed within the red dashed lines).

electronic properties.

The cyanide compounds we consider are composed of the transition metals Ni, Pd or Pt in their 2+ oxidation state and the cyanide base (CN)$^-$. The simplest possible structure consisting of these structural units, suggested by Pauling[156], is shown in Fig. 4.1(a); we refer to this as structure I. The unit cell contains one metal atom and two CN units. Each metal atom is surrounded by two C and two N atoms, with the two C atoms being second neighbors (similarly for the two N atoms). There are two other ways of arranging the atoms in the Ab initio calculations square planar lattice, but with larger unit cells. In the first, shown in Fig. 4.1(b) and called IIa, there are two metal atoms and four CN units in each unit cell, with one metal atom surrounded by four C atoms and the other by four N atoms. In the second, shown in Fig. 4.1(c) and called IIb, also containing two metal atoms and four CN units in the unit cell, each metal atom is surrounded by two C and two N atoms and the pattern is rotated by 90° in neighboring metal sites; the two C neighbors of a given metal atom are not second but third nearest neighbors (similarly for the two

N atoms); the second neighbors are C and N atoms belonging to different CN units. In all structures, the metal and CN units are linked by strong covalent bonds while the inter-planar interactions are weaker, of van der Waals type. Of these, the type IIa $Ni(CN)_2$ planar structure was experimentally reported more than a century ago [157], formed in ammonia solution; its structure has been studied in detail [158].

4.3 Results and discussions

4.3.1 Structural features

Our DFT calculations indicate that structure I, although to our knowledge not yet reported experimentally, is the lowest energy one: in the case of Ni, structure IIa has higher energy than structure I by 0.07 eV per $Ni(CN)_2$ unit; structure IIb has higher energy than structure I by 0.17 eV per $Ni(CN)_2$ unit. The detailed information is provided in Fig. 4.2. When the Ni atoms are replaced by Pd atoms to produce $Pd(CN)_2$ structures, the same situations takes place where structure I has the the lowest total energy among the three. This information is illustrated in Fig. 4.3. Thus, structure I is the thermodynamically stable one, although its formation under hydrothermal conditions in ammonia solution may have been kinetically inhibited. Using modern synthetic methods, it should be possible to form structure I by gas phase reactions. A possible reaction sequence is indicated in Fig. 4.4.

The synthesis starts by using chelating agents to clamp two of the possible bonds of each Ni atom in its square planar coordination, leaving the remaining two free to react. The product of this initial step in the reaction process is shown schematically as the initial configuration in Fig. 4.4. Next, the cyanide bases $(CN)^-$ are added.
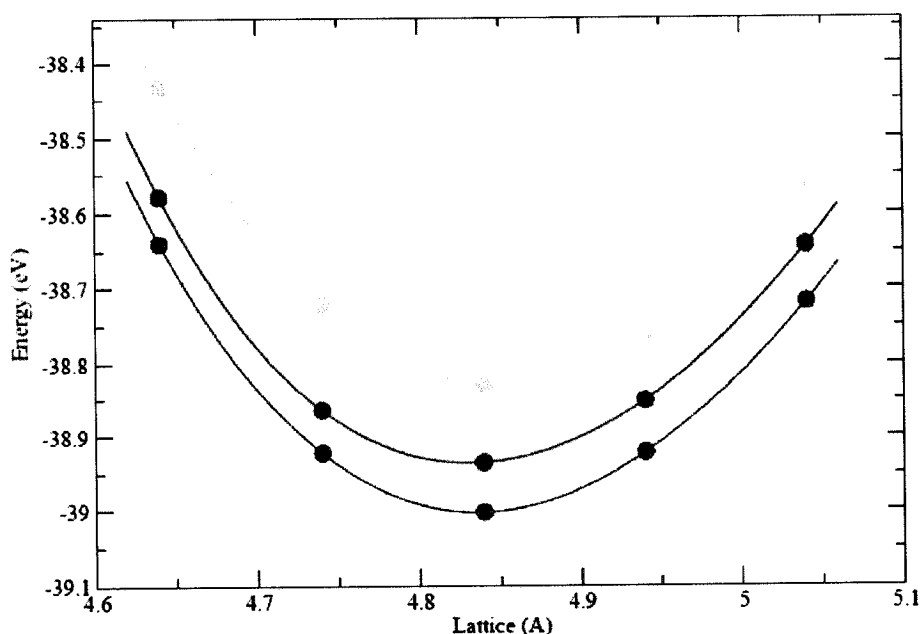
Fig. 4.2: The total energy for three Ni(CN)$_2$ structures shown in Fig.4.1 plotted as a function of $|a_1|$, the length of the lattice constant in Fig. 4.1(a). The yellow curve corresponds to structure IIb; the green curve corresponds to structure IIa; and the red curve corresponds to structure I.

These bases react in gas-phase with the clamped Ni atoms and three possible products, shown in Fig. 4.4 after step (1). The chelating agent is Ab initio calculations removed (step (2)) and the Ni(CN)$_2$ molecules are free to react with each other (step (3)) to form larger units, eventually growing to become the extended planar structure (step (4)). During this last step in the reaction, the lowest energy structure I (Fig. 1(a)) should be naturally chosen, although structures IIa and IIb or even structures with less order could be formed from a mixture of the three structural units produced by step (2) of the reaction path. Our calculations show that the electronic properties of the three planar structures are very similar, indicating that disorder will not affect the electronic behavior significantly. If a planar structure can be formed, the same synthetic procedure could lead to formation of nanotubes, as is the case for the CNTs
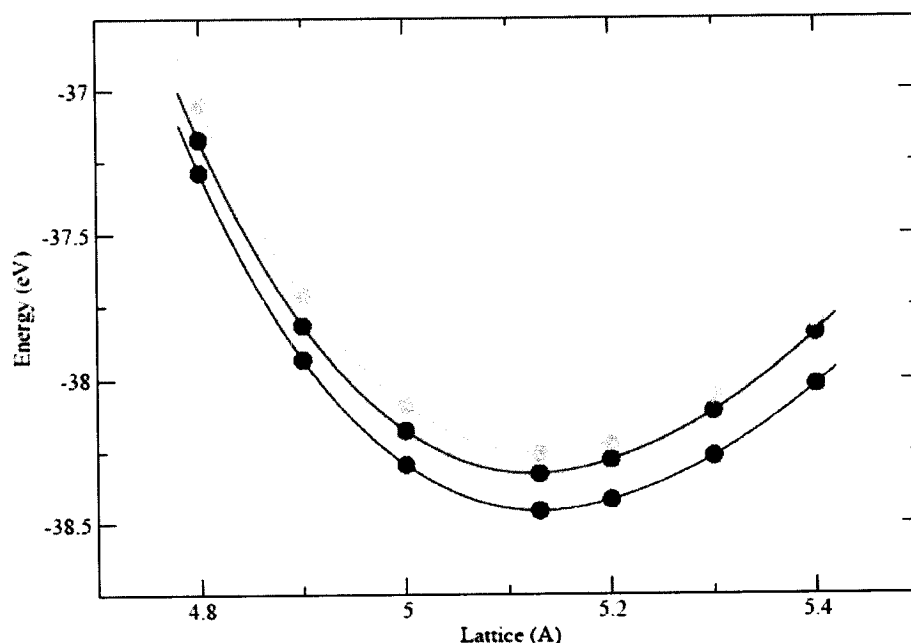
Fig. 4.3: The total energy for three $Pd(CN)_2$ structures shown in Fig.4.1, plotted as a function of $|a_1|$, the length of the lattice constant in Fig. 4.1(a). The yellow curve corresponds to structure IIb; the green curve corresponds to structure IIa; and the red curve corresponds to structure I.

and BNTs. Accordingly, in the following we concentrate mainly on the properties of planar and tubular structures based on structure I. Future discussion illustrating the similarities in electronic properties of structure I and IIa further proves that the stable electronic properties of these materials we will focus on is insensitive to the structures.

The square lattice structure of the cyanide sheet has lower symmetry than the hexagonal structure of a single graphite sheet (graphene), which effectively reduces the possible ways of rolling it into tubes. We will concentrate on the three simplest types of tubes (see Fig. 4.5): the (n,0) tubes, corresponding to rolling the sheet along one of the lattice vector directions, and the (n,n) or (n,n̄) tubes, corresponding to rolling the sheet along the two diagonal directions of the unit cell. Notice that
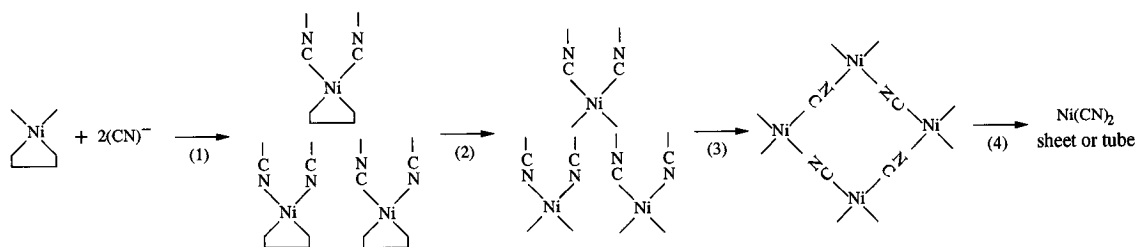
Fig. 4.4: Gas-phase synthesis of Ni(CN)$_2$ sheet and nanotubes. See text for the details of the four steps in the process.

the two diagonal directions are not equivalent: the (n,n) tubes correspond to cross-sections involving a metal atom bonded to one C and one N atom, whereas the (n,n̄) tubes correspond to cross-sections involving a metal atom bonded to two atoms of the same type (both C or both N, depending on where the cross-section is taken). Two examples (the (4,0) and (4,4̄) nanotubes) are shown in Fig. 4.5. A general chirality (n,m) is also in principle allowed, but the stability of such tubes may be inhibited by the complexity of bonding between the metal atoms and the cyanide units.

4.3.2 Electronic features

We consider next the electronic properties of the cyanide sheets and nanotubes. We find that the band structures of the sheets with different metal elements are very similar. When the sheets are rolled into 1D structures, the overall band structure features remain similar to those of the corresponding sheet structure, aside from the folding of the 2D Brillouin Zone (BZ) of the sheet to the 1D zone of the tube. Accordingly, we present here only a detailed analysis on the band structure and bonding features of the Ni(CN)$_2$ sheet, which is representative of all other cyanide planar and tubular structures.
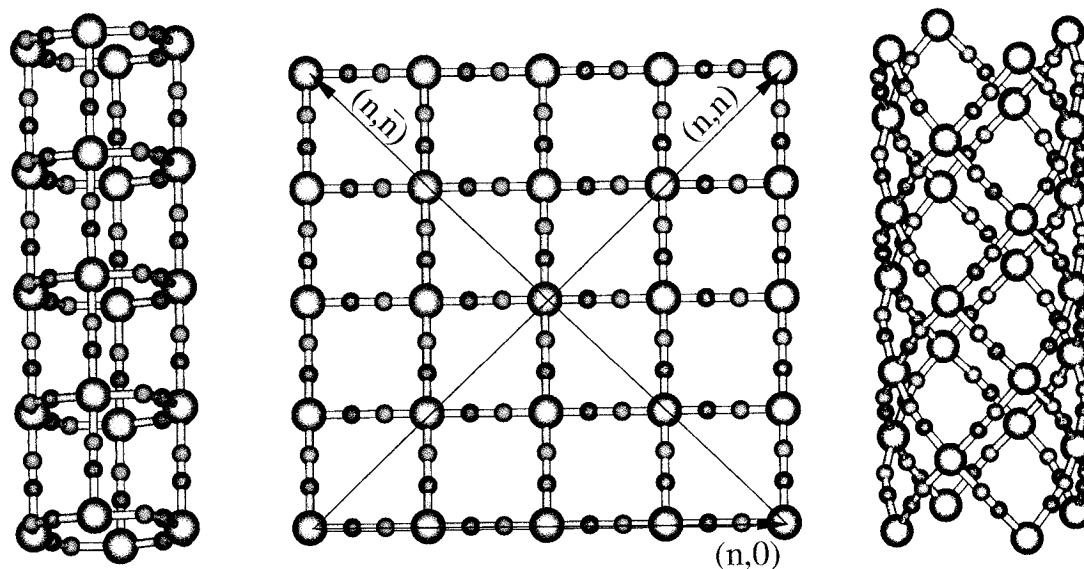
Fig. 4.5: Top view of the sheet (center, a 4 × 4 area) and the (4,0) (left) and (4,4̄) (right) nanotubes based on structure I. Diagonal and horizontal red arrows indicate the (n,0), (n,n), and (n,n̄) tube-rolling directions. (yellow spheres = metal, blue spheres = N, yellow spheres = C)

In Fig. 4.6, we show the band structure (left) and the wave function magnitude (right) of various bands at Γ, the BZ center. There are fourteen filled bands. The lowest two correspond to C-N σ bonds and their energy lies below the range shown in Fig. 4.6. The band structure shown contains the other twelve filled bands and three of the conduction bands. The band gap (2 eV) is indirect, between Γ and the high symmetry point M. Of the fifteen bands shown, four are denoted by open circles (bands 7–10, unlabeled in Fig. 4.6), lying in the range between −2 to −4 eV; these states correspond to four C-N bonds of pure π character, which, together with the C-N σ bonds, form the triple bond between these two atoms of the cyanide unit. The remaining eleven bands are denoted by filled circles and correspond to bonds involving both s and p orbitals of C and N as well as d orbitals from the metal atoms. We classify these bands into three categories:

(a) Bands 3 – 6 lie in the energy range −4 to −9 eV and correspond to N-N (band 3) and C-C (band 5) interactions, and to N-Ni-N (band 4) and C-Ni-C (band 6) bonds. All of these interactions have σ character; the last two are 3-center bonds.

(b) Bands 11 – 13, lie in the energy range −2 to 0 eV, and correspond to multiple center bonds of π character: band 11 involves all five atoms in the unit cell (a 5-center bond), band 12 involves the two N atoms and the Ni atom (a 3-center bond) and band 13 involves the two C atoms and the Ni atom (another 3-center bond). Band 14 corresponds to a non-bonding state of Ni of $d_{3z^2-r^2}$ character; this last band is the highest occupied one and exhibits no dispersion, since it does not involve interaction with any of the other orbitals.

(c) The remaining three bands are unoccupied, and correspond to the anti-bonding combinations of states that were already encountered in the valence manifold, as is evident from the wave function features.

The band structure described above can be accurately reproduced by a tight-binding scheme with a minimal basis consisting of the four sp orbitals of C, the four sp orbitals of N and the five d orbitals of Ni. A detailed interpretation of the character of the bands is provided in Table 4.1. The participation of d orbitals introduces two groups of interesting multi-center interactions: the relatively weak 5-center π interactions (bands 11,12,13), and the considerably stronger 3-center σ interactions (bands 4 and 6). Interrupting or distorting these interactions would incur large energy costs. Based on this observation we predict that the (n,n) and (n,n̄) diagonal tubes will have lower energy than the (n,0) square tubes because rolling the sheet along the diagonal direction introduces smaller distortion to the 3-center σ interactions. For short, finite tubes, the issue of interruption of interactions at the end of the tube will also be important. In this case, we expect the (n,n̄) type to be
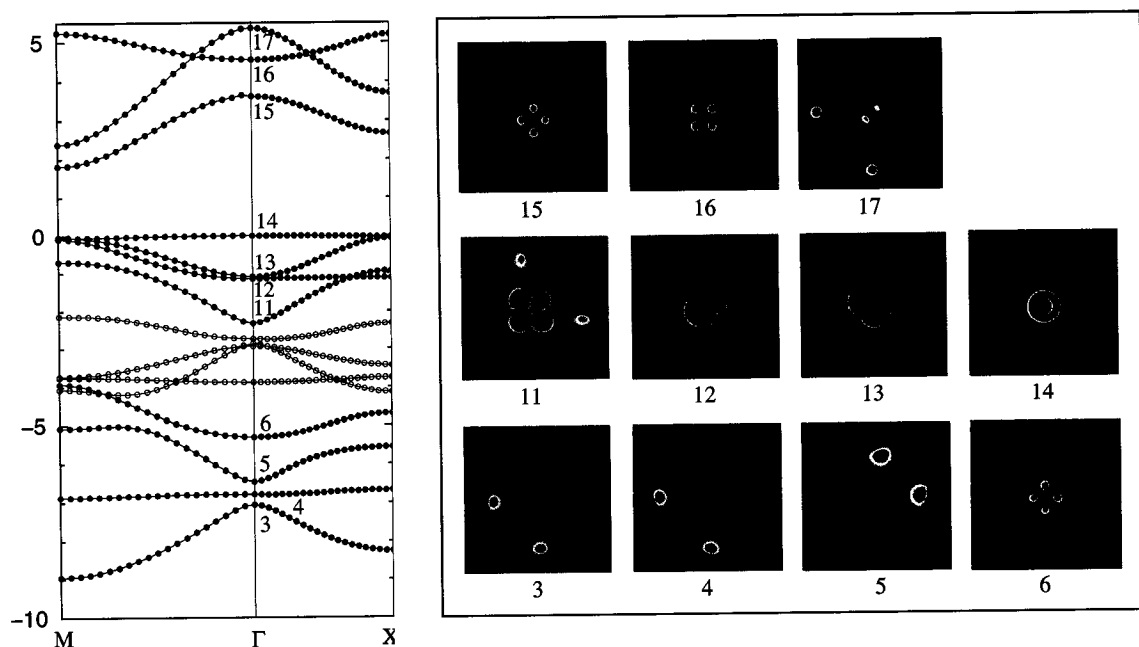
Fig. 4.6: **Left**: Band structure of the $Ni(CN)_2$ sheet; the Fermi level is at the highest occupied band. **Right**: plots of $|\psi_i(\mathbf{r})|^2$ for the wave function at Γ that include significant contributions from Ni d orbitals (see text).

the preferred structure for the following reasons: termination along $(n,0)$ eliminates two σ interactions and two π interactions and distorts the remaining 3-center σ interaction significantly; termination along (n,n) eliminates four σ interactions and four π interactions; termination along $(n,\bar{n})$ eliminates only one σ interaction and two π interactions.

At this point, let us pay a revisit to the three structures illustrated in Fig. 4.1 from an electronic point of view. Fig. 4.7 and 4.8 show the band structures of $Ni(CN)_2$ I and IIa structures and $Pd(CN)_2$ I and IIa structures, respectively. The band structures are calculated with two units of $M(CN)_2$ pairs, which is the unit cell of structure IIa. As is readily shown on these figures, structure I and IIa of both materials share the same features in bands. The major difference comes from the

n	Ni orbitals	C,N orbitals	character
17	$(d_{yz} + d_{zx})$	$-[\gamma(p_z^{C_1} - p_z^{C_2}) - \delta(p_z^{N_1} - p_z^{N_2})]$	anti-bonding
16	d_{xy}	$-[\alpha(p_y^{C_1} + p_x^{C_2}) - \beta(p_y^{N_1} + p_x^{N_2})]$	anti-bonding
15	$d_{x^2-y^2}$	$-[(s^{C_1} - p_x^{C_1}) - (s^{C_2} - p_y^{C_2})]$	anti-bonding
14	$d_{r^2-3z^2}$		non-bonding
13	$(d_{yz} - d_{zx})$	$+[\delta(p_z^{C_1} - p_z^{C_2}) + \gamma(p_z^{N_1} - p_z^{N_2})]$	$C_{1,2}$–Ni–$N_{1,2}$ (π)
12	$(d_{yz} + d_{zx})$	$+[\gamma(p_z^{C_1} + p_z^{C_2}) - \delta(p_z^{N_1} + p_z^{N_2})]$	$C_{1,2}$–Ni–$N_{1,2}$ (π)
11	d_{xy}	$+[\alpha(p_y^{C_1} + p_x^{C_2}) - \beta(p_y^{N_1} + p_x^{N_2})]$	$C_{1,2}$–Ni–$N_{1,2}$ (π)
6	$d_{x^2-y^2}$	$+\epsilon[(s^{C_1} - p_x^{C_1}) - (s^{C_2} - p_y^{C_2})]$	C_1–Ni–C_2 (σ)
5		$(s^{C_1} - p_x^{C_1}) + (s^{C_2} - p_y^{C_2})$	C_1–C_2 (σ)
4	$d_{x^2-y^2}$	$+\epsilon[(s^{N_1} + p_x^{N_1}) - (s^{N_2} + p_y^{N_2})]$	N_1–Ni–N_2 (σ)
3		$(s^{N_1} + p_x^{N_1}) + (s^{N_2} + p_y^{N_2})$	N_1–N_2 (σ)

Table 4.1: Interpretation of electronic states at Γ, in terms of transition metal d orbitals and C, N s and p orbitals (see text for details). σ and π stand for the character of the interactions; $\alpha - \epsilon$ are coefficients that determine the weight of each orbital in the electronic state (an overall normalization factor is omitted).

some minor relative shifts of the bands. The characteristics of the band gaps, top valence bands and bottom conduction bands are largely kept. Notice that structure I always has the largest band gap, which is another sign indicating that it is the more stable structure of the two.

To support our qualitative analysis of the stability of cyanide nanotubes which was based on the strength of bonds between atoms, we have performed extensive total energy calculations for the $Pd(CN)_2$ sheet and nanotubes; the results are shown in Table 4.2. From these results, we find that the infinite (4,4) and (4,$\bar{4}$) nanotubes have an energy 0.43 eV per $Pd(CN)_2$ unit lower than that of the (4,0) tubes, consistent with our analysis. Furthermore, we find that all three $Pd(CN)_2$ nanotubes are semiconductors with indirect gaps ranging from 2.1 to 2.8 eV. Compared to the sheet structure, the band gap closes by 0.83 eV for the (4,0) tubes, and by 0.12 eV for both the (4,4) and (4,$\bar{4}$) tubes, which correspond to decreases of 28% and 4%, respectively,

band structure for (I)   band structure for (IIa)
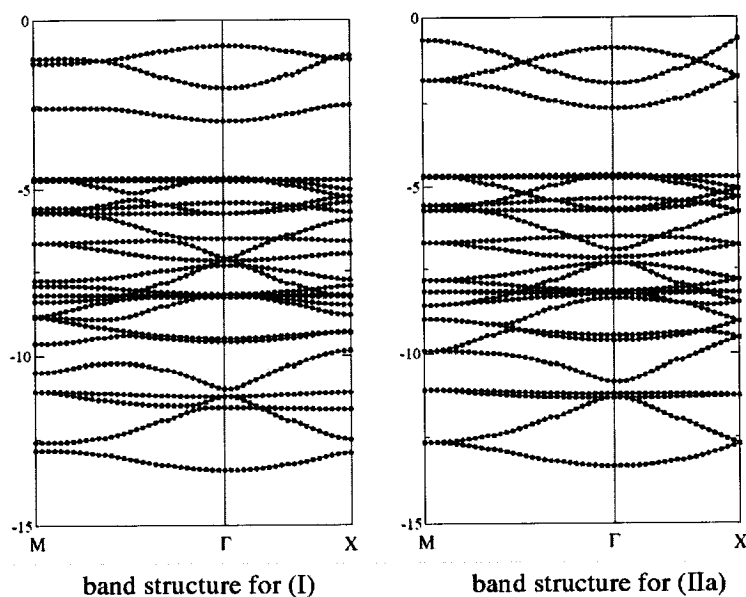
Fig. 4.7: The comparison of band structures of Ni(CN)$_2$ sheet as shown in Fig. 4.1(a) and (b).

from the band gap of the sheet. Notice that the band gap of these three nanotubes increases with the diameter, but is always smaller than the band gap of the sheet. This feature is consistent with previous studies of MoS$_2$ nanotubes [159]. This is further confirmed by additional calculations on (5,0) and (6,0) Pd(CN)$_2$ nanotubes. We find that the band gaps of the fully relaxed (5,0) and (6,0) tubes are 2.66 eV and 2.56 eV, respectively. Both are larger than that of (4,0) tubes and smaller than that of the sheet. It is also interesting to note that the (4,4) and (4,$\bar{4}$) tubes, which have diameters larger than the diameter of the (5,0) tube but smaller than that of the (6,0) tube, have larger band gaps than the square tubes. Considering that the $n = 4$ nanotubes are those with the smallest possible diameter, we conclude that cyanide nanotubes have relatively stable band gaps and uniform electronic properties. This is an essential element for practical applications. Compared to our cyanide nanotubes, the band gaps of BNTs exhibit considerably larger relative variation with

band structure for (I)   band structure for (IIa)
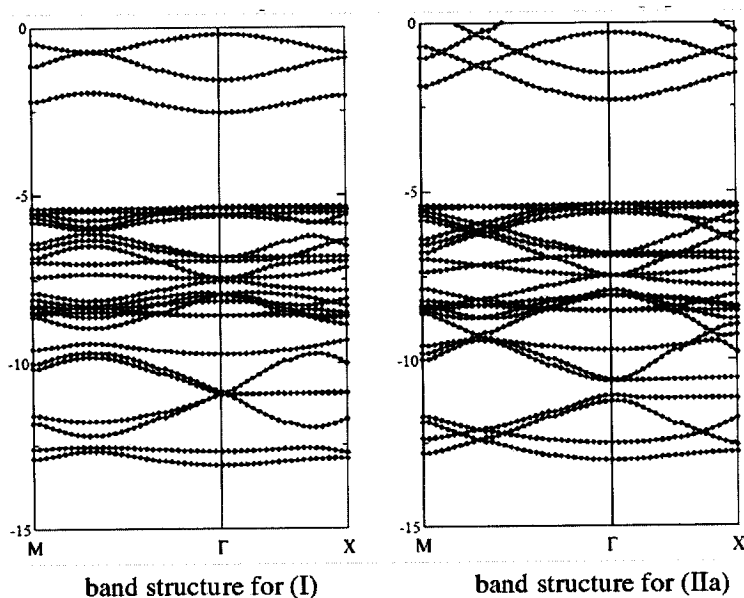
Fig. 4.8: The comparison of band structures of $Pd(CN)_2$ sheet as shown in Fig. 4.1(a) and (b).

the tube diameter while for CNTs the relative band gap variation is even larger and the character of the system can easily change from semiconducting to metallic as a function of diameter and chirality changes.

4.3.3 Mechanical properties

We next consider the mechanical properties of the cyanide nanotubes. A quantitative description of the elasticity of the tubes requires a calculation of Young's modulus, which involves specifying a wall thickness for the tubes. To our knowledge, there have been different standards on how this quantity should be defined for nanotubes [160, 161, 162]. Both the interlayer separation in the corresponding layered material (graphite for CNTs, [160]) and the average optimized intertube distance in periodic arrangements [162] have been used as measures of the tube wall thickness.

Experimentally it has also been difficult to provide a precise value of Young's modulus for nanotubes [163, 164, 165, 166]. Previous theoretically and experimentally determined values of Young's modulus fall within a range around 1 TPa for CNTs and around 0.8 TPa for BNTs [167]. Recent experimental and theoretical work has provided a more comprehensive picture of the mechanical properties of various nanotubes [168, 169, 170]. For the cyanide nanotubes, we use the intertube distance as the thickness of the tubes. To obtain this value, we considered a periodic arrangement of nanotubes on a hexagonal lattice in the plane perpendicular to their axis: in the optimal configuration, obtained from energy minimization, the intertube distance for the (4,0) nanotubes is 4.4 Å, for the (4,4) nanotubes 4.0 Å, and for the (4,$\bar{4}$) nanotubes 3.7 Å. The intertube interactions are weak (van der Waals type), and the energy in the periodic arrangement is lower than for isolated nanotubes by 0.1 eV for the (4,0) nanotubes, and by 0.01 eV for the (4,4) and the (4,$\bar{4}$) nanotubes per unit cell. Structural parameters for the three types of nanotubes in the isolated and crystalline arrangement are summarized in Table 4.2. In general, the intertube interactions do not alter their structure or electronic properties.

Young's modulus values listed in Table 4.2 for the cyanide–transition-metal nanotubes are more than one order of magnitude smaller than those of the CNTs and the BNTs reported in the literature. This is due to the fact that the cyanide nanotubes have much larger open spaces between rows of bonded atoms, providing additional room for atomic relaxation when stress is applied, in contrast to the CNTs and BNTs where the very compact arrangement of atoms leaves little room for relaxation. The value of Young's modulus for the (4,$\bar{4}$) tubes is twice as large as that of the (4,4) tubes. This is due to the nature of the 3-center σ bonds around the metal atom (M): the stretching of the (4,$\bar{4}$) tubes along the (n,n) direction, due to distortion brought

	sheet	(4, 0) tube	(4, 4̄) tube	(4, 4) tube
ΔE (eV)	0.00	0.56 [0.46]	0.13 [0.12]	0.13 [0.12]
ε_{gap} (eV)	2.96	2.13 [2.12]	2.83 [2.69]	2.82 [2.68]
Pd–N (Å)	2.03	2.05 [2.06]	2.04 [2.03]	2.04 [2.03]
Pd–C (Å)	1.94	1.94 [1.94]	1.94 [1.94]	1.94 [1.94]
C–N (Å)	1.17	1.17 [1.17]	1.17 [1.17]	1.17 [1.17]
D (Å)		7.08 [7.04]	8.95 [8.92]	9.07 [9.09]
d (Å)		[4.43]	[4.00]	[3.73]
Y (TPa)		0.23 [0.24]	0.06 [0.05]	0.03 [0.04]

Table 4.2: Structural and electronic properties of the $Pd(CN)_2$ sheet and nanotubes: ΔE is the energy difference of the tubes relative to the sheet per $Pd(CN)_2$ unit; ε_{gap} is the electronic band gap; Pd–N, Pd–C and C–N are the distances between pairs of atoms; D is the tube diameter; d is the inter-tube distance; Y is Young's modulus. The numbers in square brackets correspond to values in the periodic arrangement of tubes, those without brackets to isolated tubes. The bond lengths of the (4,0) nanotube in the directions parallel and perpendicular to the axis are the same to within 0.01 Å.

by the wrapping of the sheet into a tube, distorts both the C-M-C and the N-M-N σ bonds, while the same operation on the (4,4) tubes along the (n,n̄) direction helps to relax the distortions of those bonds, accounting for the large difference in the response of the two types of tubes to external stress. This fact also supports our prediction that among the cyanide nanotubes with finite length, those of (n,n̄) type are likely to be the most stable.

4.4 Conclusions

Cyanide–transition-metal nanotubes could prove useful because of their structure-independent electronic structure as a function of size and chirality. By proposing and studying these tubes, we hope that this special property could be used for large scale semiconducting nanotube production and facilitate the use of these nanostructures

as key elements in electronic device applications. It is also straightforward to produce doped nanotubes, at least in principle. Specifically, by introducing in sufficient concentration acetylene (C_2H_2) instead of cyanide (HCN) at the second step of gas phase synthesis, some CC units will be incorporated in the tube in place of the CN units, producing p-doped structures. By analogy, if N_2 molecules were to be introduced at the second step of the gas phase synthesis under the right conditions some CN units will be replaced by NN units, giving rise to n-doped structures; however, due to the exceptional stability of the N_2 molecule it may be significantly more difficult to produce n-doped tubes than p-doped tubes. Moreover, these tubes could also be easily functionalized because of the presence of several types of atoms, and in particular the metal elements that can react more readily than the fully bonded C and N atoms. As our preceding analysis showed, both the valence band maximum and the conduction band minimum of the cyanide tubes have components from the d orbitals of the Pd atom. In particular, the highest occupied band corresponds to a pure $d_{3z^2-r^2}$ orbital, with lobes pointing out of the plane. This orbital would be available for interaction with orbitals of adsorbate atoms. Thus doping of these semiconducting tubes may produce interesting variations of their electronic properties.

In conclusion, we have proposed a new type of nanotubes based on transition metals and cyanide units. All the tubes we have examined are semiconductors regardless of their chirality. Variations of electronic band gaps with chirality are much smaller than in other types of nanotubes, like the common carbon or boron nitride nanotubes. The interesting nature of bonds in these systems, some involving more than two atoms, will play an important role in selecting the structure of the most stable tubes. In our study, the (n, n̄) tubes were found to be the most stable, which we suggest may be dominant in experimental growth of cyanide tubes. Although

mechanically not as stiff as CNTs and BNTs, we expect these tubes to be reasonably strong. They may also serve as efficient hydrogen-storage devices due to the presence of the metal atoms which can act as catalytic centers.

4.5 Acknowledgments

Chapter 5

Pentacene molecules on inert surfaces

5.1 Overview

As we mentioned in the previous chapters, silicon is the material that builds up the semiconducting industry. Although silicon is abundant on this planet, it usually exits in an amorphous state. The price of making high efficient devices with silicon in its crystalline form is very high. Research has been conducted in applications of nanotubes, nanowires, and thin-films in the industry. Organic materials have been considered for use in solar cells and transistors. One of them that has been found to demonstrate promising properties is pentacene thin-film transistor.

Pentancene is a type of organic semiconductor. People first noticed that the best performed pentacene films have charge mobilities close to amorphous silicon. Further experiments showed that monolayer crystalline pentacene thin-film has similar performance. Compared to traditional silicon based transistors, the pentacene thin-film transistors are much cheaper to manufacture. Also, these organic transistors are more flexible and thus could be used in various conditions when bending or twisting occur. Similar to the silicon case, the transistor performs the most efficiently when the pentancene film is crystalline. Amazingly, although pentacene molecule consists of 36 atoms and are about 15 Å by 5 Å in size, the self-assembled pentacene thin-film demonstrates a crystalline structure in an area up to order of 1 μm^2. To further improve the performance of the pentacene thin-film transistors, understanding of the energetics, diffusion, island formation and evolution are critical.

In this chapter, we study the energetics and dynamics of pentacene molecules in vacuum and saturated diamond (111) surface and silica surfaces. Force field simulations are applied to capture the van der Waals type interactions among the pentacene molecules and the substrates. The herringbone arrangement of the molecules is found

to be optimal both in vacuum and on various surfaces. A 90 degree rotation of the entire structure relative to that experimentally reported is identified on the silica surfaces.

5.2   Introduction

There has been an increase interest in organic semiconductors for applications in electronic devices as light-emitting diodes, photovoltaic devices, and thin-film transistors. Pentacene in particular has been the focus of much attention. The charge mobility and injection in the pentacene crystals are known to depend strongly on molecular orientation and packing [172]. Various experiments have been conducted on pentacene thin-films on silica surfaces [173, 174, 175, 176, 177]. To improve the performance of the pentacene thin-films, understanding, monitoring and controlling the structural growth process is crucial. Unfortunately, until today, basic questions like the pentacene molecule surface diffusion barriers, island structures etc. are not experimentally answered.

A pentacene molecule is composed of five benzene rings linearly arranged (Fig. 5.1) and has the molecular formula $C_{22}H_{14}$. For convenience, we refer to the sides along the long axis of the molecule as long ends, and the other two sides along the short axis as short ends. The three-dimensional(3D) crystalline structure of pentacene was experimentally reported triclinic[178]. Each unit cell is made up of two molecules. The experimentally claimed two-dimensional(2D) structure is similar to one layer in the a-b plane of the 3D structure. Pentacene monolayer was found to be 15 - 16 Åthick, which indicates that the long axis (c) of the molecules is out of the surface plane. Different experimental conditions, like deposition rate,

surface temperature, etc. introduce more complications to the structures. Various monolayer heights, island structures and densities have been observed, which call for better theoretical understandings of the systems. On the other hand, because of the large size of the systems and the ineligible van der Waals interactions involved, first-principles simulations are not applicable and systematic study is in lack.

In this chapter, we study pentacene molecule at a fundamental level to understand the experimental facts. We first focus on the flexibility of a single pentacene molecule, pentacene pentacene pair interactions with different configurations in vacuum, and pentacene monolayer structure and dynamics in vacuum. Next we introduce three substrate, the H-terminated diamond (111) surface, the H-terminated silica surface, and the OH-terminated silica surface. Molecular dynamics(MD) force field simulations within CHARMM are performed at room temperature and around 60° C. We find that pentacene molecules form herringbone structure both in vacuum and on surfaces. However, the pentacene monolayers on different surfaces have a 90 degree rotation relative to the experimentally reported structure. We analyzed in detail the effect of pentacene-substrate interaction on the island structure.

5.3 Results

The flexibility of a single pentacene molecule has been neglected. It is commonly assumed that the five rings are flat in the same plane (pentacene plane). Theory of diffusion limited aggregation has been applied to interpret the dendrite morphology of the pentacene islands, assuming the molecules are rigid. To check whether the assumption is valid in dynamics studies at an atomic level, we study the energy cost of bending the molecule, using both force-field and density-functional calculations.

The results are summarized in Fig. 5.1.
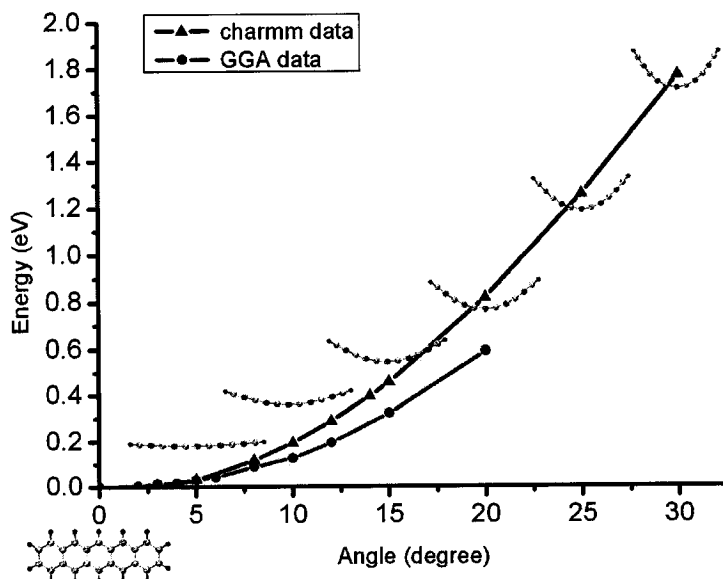
Fig. 5.1: The energy cost (vertical axis) of bending a pentacene molecule at different angles (horizontal axis). θ is the dihedral angle between every neighboring benzene rings. For each θ, the four C atoms at the two ends of the molecule are fixed, while all other atoms are subjected to relaxation. The total energy of a single flat pentacene is set to be zero.

From Fig. 5.1, pentacene molecule in a flat configuration indeed has the lowest energy. However, the energy cost of bending the molecule below 10 degrees is minimal. The pentacene molecule is actually very flexible, which is also observed in the dynamics. This flexibility assisted the molecules' kinetic search for optimal configurations. Notice that below 5 degrees, the two curves in Fig. 5.1 match perfectly, which indicates the reliability of the empirical calculation. This result informs us that it would be improper to treat the pentacene molecule as a rigid body in future simulations. The flexibility of the molecules facilitates the rotational motions during this process and thus assists the realization of the optimal island or film structure.

Next we consider the pentacene-pentacene interactions in vacuum. Four most

common configurations are pentacene face to face perfect with match, face to face with a shift along the long axis by half the ring size, face to face with a shift along both the long axis and the short axis, and two pentacenes in a unit cell of a periodic herringbone arrangement (Fig. 5.2).

	inter-molecule distance (Å)	interaction energy (eV/pair)
a	3.566	0.54
b	3.690	0.57
c	3.564	0.57
d	periodic herringbone structure	2.86

Table 5.1: The inter-molecule interaction between the two pentacenes in vacuum. The four configurations (a-d) are shown in Fig. 5.2.
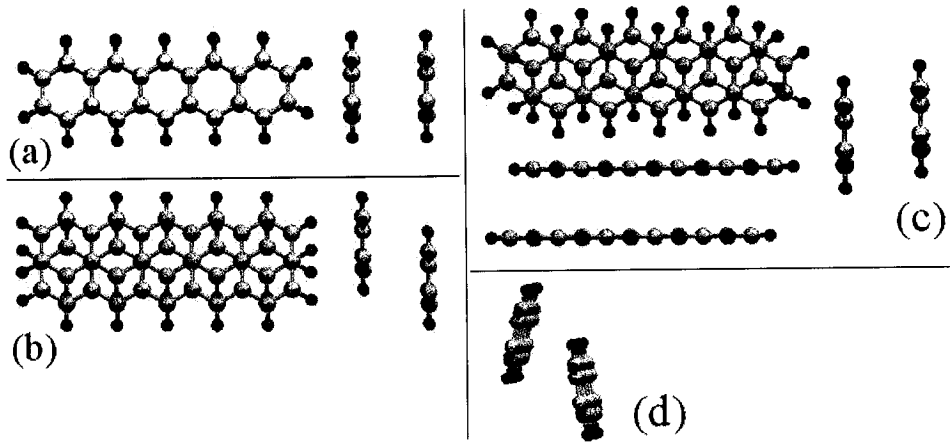
Fig. 5.2: Three configurations of two pentacenes in vacuum. (a) face to face perfect match; (b) face to face shift along long axis; (c) face to face with a shift along both long and short axes; and (d) the two pentacene molecules in a unit cell for periodic 2D structure in herringbone structure. Configurations (a), (b) and (d) are retained after minimization while configuration (c) collapses into configuration (a) after energy minimization.

The inter-molecule distances between the molecules in Fig.5.2 (a)-(c) are around 3.6 Å. By minimizing total energy, the size of the two-dimensional unit cell in Fig.5.2 (d) is 6.08 Å by 7.28 Å, which is slightly different from what is reported in Ref.[179]. The interaction energies in Table 5.1 clearly indicate that in vacuum periodic her-
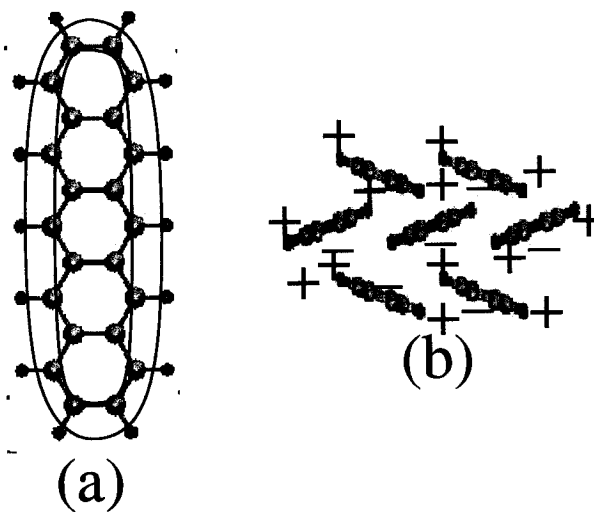
Fig. 5.3: (a): charge distributions on a pentacene molecule and (b): the resulted herringbone interactions among molecules. Blue represents accumulation of negative charges and red represents accumulation of positive charges.

ringbone structure is preferred. MD simulations are conducted at room temperature for 20 pentancene molecules lined in a row with 5 Å between nearest neighbors. The pentacene molecules split into two groups and each has the molecules stacked in the ideal herringbone structure. In reality, the herringbone structure is resulted from dipole-dipole interactions between the molecules. Because the C atoms are slightly more electronegative than the H atoms, more negative charges are accumulated near the C atoms. Correspondingly, more positive charges are accumulated near the H atoms.

Next we study the energetics and kinetics of the pentacene molecules on different surfaces. The three surfaces we consider are shown in Fig. 5.4. During simulations, the diamond substrate is frozen because of technical restrictions, while the two silica surfaces are free to relax. Since there are no formation of chemical bonds or charge transfer between the pentacene molecules and the surfaces, the study with frozen

H-terminated C(111) surface (gray-C; red-H)
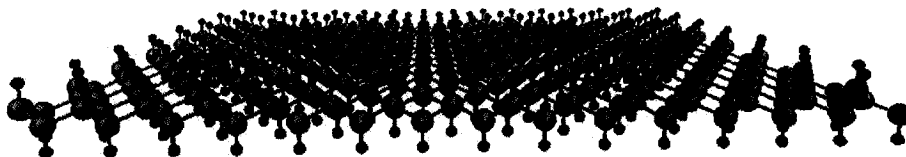
OH terminated side (red-H; blue-O; cyan-Si)
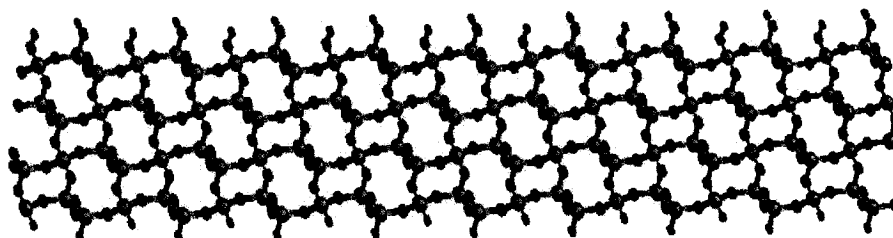
H-terminated side

Fig. 5.4: The three surfaces we consider. Top: bi-layer diamond (111) surfaces terminated with H; Bottom: upper surface, OH terminated silica surface, and lower surface, H terminated silica surface.

substrate would still catch the main characteristics of the system. The pentacene-surface interactions are calculated and summarized in Table 5.2.

The pentacene-H-diamond surface interaction is the weakest of the three. Notice that it is also smaller than the optimal pentacene-pentacene interaction in vacuum, based on which we can predict that pentacene molecules on the diamond surface may behave differently from on the other two surfaces, and that the pentacene-pentacene

surface	interaction (eV)
H-diamond	1.11
OH-silica	1.49
H-silica	1.75

Table 5.2: The interaction energy between a single flat pentacene molecule on top of three different surfaces. The distance between the molecule and the surfaces is about 3.5 Å.

interaction would be favored against the pentacene-diamond surface interaction. In MD simulations, we place one layer of pentacenes lying flat on the diamond surface, at both room temperature and 60 °C. Within one nanosecond, the molecules evolve into a more compact stacking, where they rest on their long end and the pentacene plane is tilted out of the surface plane by an angle of about 45 - 60 degrees.

For more realistic studies that are close to experimental facts, we next focus on the two surfaces of silica. To learn the structure of the pentacene island on these surfaces, the ideal approach would be let a number of pentacenes move under a certain temperature for very long time until they reach the equilibrium state. However, this approach is not applicable because of the cost of such computation is not affordable. In literature, most studies are done only with the energetics of a pre-assumed configuration[180]. With compromise to the resource restriction while at the same time to step ahead of the existing static studies, we examine the dynamics of three simple model systems.

The first system we study has four layers of pentacenes stacked on top of the silica surfaces, each layer with two flat molecules next to each other along the direction of the short axis. The second system has sixteen pentacene molecules standing on their long ends vertical to the surfaces. The last system contains seven molecules on their short ends on the surfaces. The corresponding configurations are shown in Fig. 5.5. Any possible configurations of the pentacene islands/molecules on the surfaces are combinations of those in the three models (with possible tilting angles). Thus the study of the three simple models should be illustrative for an understanding of more complicated situations.

MD simulations are performed for all three models at 330K. On both H-silica and OH-silica surfaces, the pentacene molecules are equilibrated to a herringbone
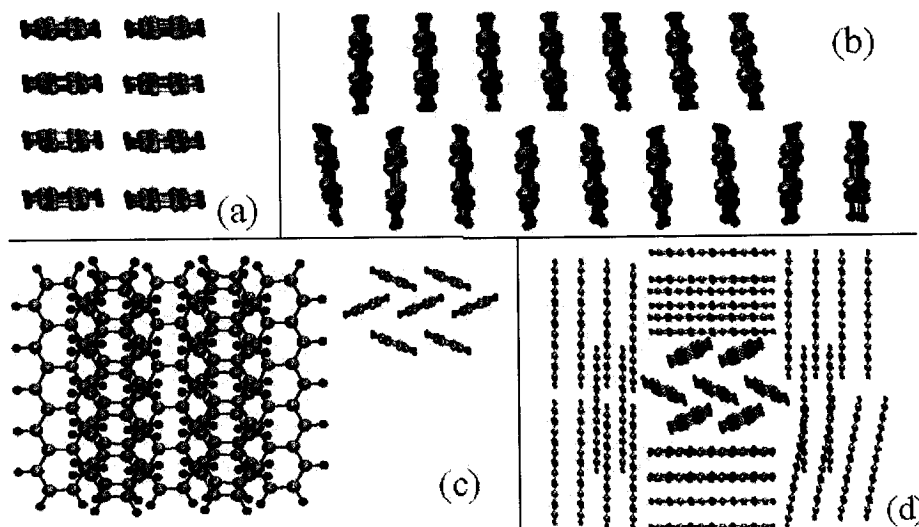
Fig. 5.5: Three model configurations of pentacenes on silica surfaces for MD simulations. (a), side view of eight molecules in four layers, each layer with two flat molecules; (b): side view of sixteen molecules in two layers, standing on their long ends with the pentacene surface vertical to the substrate surface; (c): seven molecules standing on their short ends in a herringbone strucrure, left: side view, right: top view. (d): thirty-nine molecules in a mixed phase, seven on their short ends in the center, thirty-two on their long ends in two layers surrounding the center.

structure with their long ends contacting with the surfaces. In the first model, the pentacene island has two layers on the OH-silica surface, but only one layer on the H-silica surface. We extend the model to sixteen molecules lying flat on the surface, four in each layer in total of four layers. MD simulations give similar results to the original model, except that the pentacene island on OH-silica has five layers while on H-silica there are four layers. Not only the molecules within the island are in an optimal herringbone structure, those along the edges of the island do their best to optimize the interactions as well. The second and third models result in similar island structure as the first model. All molecule choose to stand on their long ends and pack into a herringbone structure. The more important information from these three models is that the simulated pentacene island structure on the surface has a 90 degree

rotation compared to the one reported in some experiments. These results from dynamics are consistent with the previous study on energetics, where we find that the pentacene silica surface interaction is stronger than the optimal pentacene pentacene interaction. The pentacene molecules will choose to maximize their interaction with the surface. On the other hand, the pentacene-surface interaction on the H-silica surface is stronger than that on the OH-silica surface, which lead to a smoother growth on the H-silica surface than on the OH-silica surface.

However, the study of the three models may not be fully convincing since the length of the simulation is only about 1 ns, which is much shorter than experimental exposure time. The question whether at longer time the island structure would be further changed have most of the molecules stand on their short ends remains. We thus design a more complicated model assuming that this transition has taken place at a certain time that our first three models did not reach, and start our simulation at this moment to examine what happens next. A more detailed description is that we consider an island with thirty-nine molecules arranged in a mixed phase: seven standing on their short ends in herringbone structure in the center, thirty-two on their long ends in two layers surrounding the center. It covers an area of about 31.6 Å × 36.0 Å. MD simulations are conducted at 330K for 10ns. On both H-silica and OH-silica surfaces, no new molecules are found to change from their flat or long-end phase into the short-end standing phase. Instead, the seven short-end standing molecules all are changed into other phases. This study informs us that under the conditions we consider in these simulations, pentacene molecules in short-end phase would neither be created nor be maintained. The critical question is, is this the a systematic error from the simulation because of the empirical description of the potential applied and the experimental reports could be reasonably recon-
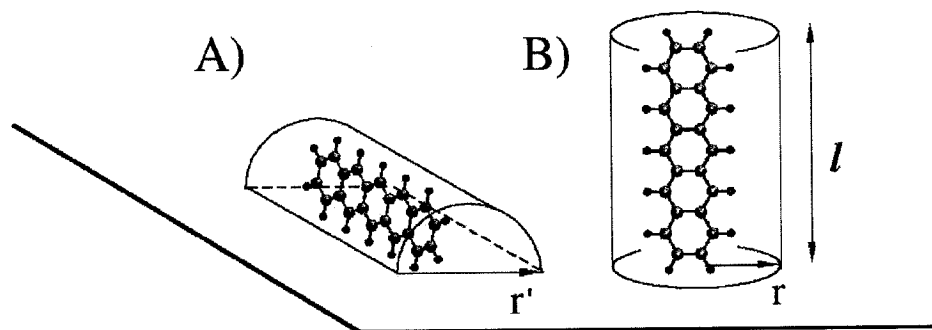
Fig. 5.6: Two possible pentacene island structures on inert surfaces. (a): pentacenes lying on their long ends, arranged in a herringbone structure and forming a half cylinder. (b): pentacenes lying on their short ends, arranged in a herringbond structure and forming a cylinder.

structed when the potential is properly adjusted. Further studies could certainly make clarifications. Most importantly, the island structures needs be investigated as the pentacene-substrate interaction changes and all other parameters fixed. We next show that this value governs the island structure on the surfaces.

5.4 Discussions

The simulation results can be analyzed by the following simple reasoning without knowledge of the specific values of various interaction energies. Three types of energies are contributing to the total energy of the pentacene system, the total pentacene-pentacene interaction E_{pp}, the total pentacene-surface interaction E_{ps}, and the total surface energy of the pentacene island E_s. When forming an island (before the first monolayer is formed), there are two island shapes corresponding to two phases of the pentacene molecules are in. Fig. 5.6 (a) shows an island in a half cylindrical shape lying on the surface; the radius of the cross section of the cylinder

is $\sqrt{2}r$ and the length of the cylinder is l, the length of a pentacene molecule. Fig. 5.6 (b) depicts an island in a full cylinder standing on the surface; the radius of the cross section is r and the length of the cylinder is l. Notice that the two islands have the same volume $\pi r^2 l$, in which we can assume the same number of pentacene molecules will fit. Suppose all molecules in both islands are in optimal herringbone structure, the surface energy density of the pentacene island is ε_s per unit area, and the pentacene-substrate interaction energy density is ε_{ps} per unit area, then the total energy of island (a) is

$$E_a = -E_{pp} + (\sqrt{2}r\pi l + 2rl) \times \varepsilon_s - 2rl \times \varepsilon_{ps}, \tag{5.1}$$

and the total energy of island (b) is

$$E_a = -E_{pp} + 2\pi r l \times \varepsilon_s. \tag{5.2}$$

ε_{ps} is close to zero in island (b) and thus E_{ps} is ignored in this case. The total energy difference of the two islands is

$$\Delta E_{ab} = E_a - E_b = (2 + \sqrt{2}\pi - 2\pi)rl \times \varepsilon_s - 2rl \times \varepsilon_{ps} \approx (0.166\varepsilon_s - 2\varepsilon_{ps})rl. \tag{5.3}$$

ΔE is larger than zero only when

$$(0.166\varepsilon_s - 2\varepsilon_{ps})rl > 0, \tag{5.4}$$

i.e.

$$\varepsilon_{ps} < 0.083\varepsilon_s. \tag{5.5}$$

Take the unit area as the flat surface area of one side of a pentacene molecule, we can estimate the ε_s to be 1.43 eV from the optimal pentacene-pentacene interaction energy in a periodic cell. Thus only when

$$\varepsilon_{ps} < 0.12eV, \qquad (5.6)$$

which means the pentacene-substrate interaction is smaller than 0.12 eV per molecule, island (b) has a lower energy than island (a). This can only happen when the substrate-pentacene interaction is smaller than 3 meV per atom. In our simulation, ε_{ps} is much larger than 0.12 eV and thus the islands are always in shape (a). When the deposition is close to cover the an infinite surface area, E_s is close to zero for island (b). In this situation,

$$\Delta E_{complete} = (\varepsilon_s - \varepsilon_{PS}) \times S \qquad (5.7)$$

where S is the area of the pentacene covered surface. If the condition in Eq. 5.5 is satisfied, $\Delta E_{complete}$ is always larger than zero and island (b) structure is consistently preferred from low coverage islands to monolayer thin film. Otherwise the pentacene islands and thin-film will be more complicated configurations.

Notice that although ε_{PS} is hard to calculate precisely in theory (using force field simulations, the results are questionable; using DFT, the Van der Waals forces are under estimated and also the calculation is very expensive with a large system), it should be a parameter that can be easily measured in experiments. Since ε_s can be well-estimated from the relatively reliable pentacene-pentacene interaction energy (will be addressed below), the combination of theory and experiments should provide a comprehensive understanding of pentacene molecules on various inert surfaces.
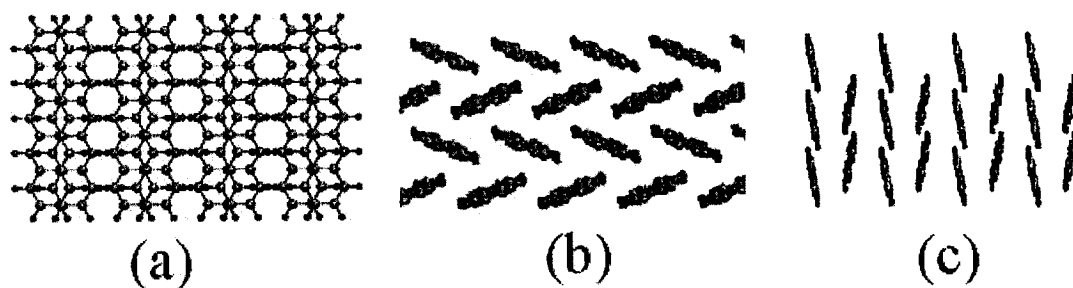
Fig. 5.7: Side view of three possible crystalline pentacene island structures on silica surfaces. (a): One layer of pentacene molecules on their short ends; (b): Four layers of pentacene molecules on their long ends, the surface benzene rings in has an angle of about 10 − 15 degrees to the substrate surface; (c) two and half layers of pentacene molecules on their long ends, the surface the benzene rings in has an angle of about 75 − 80 degrees to the substrate surface.

Before closing, let us take another look at the results from current simulations and experiments. We find that there are three possible structural configurations in 2D crystalline island or monolayer. The first one is as reported in the experiment (Fig. 5.7 (a)), the second configurations the one from our simulation (Fig. 5.7 (b)), the third configuration is the arrangement that takes place near the island edges from observation of the equilibrated state of the simulations (Fig. 5.7(c)). To reach the same height of 15 − 16 Å, and cover 1 μm^2, configuration (a) with pentacenes on their shortends requires 1 layer, and a total of 4.5 × 10^6 molecules; configuration (b) with pentacenes on their long-ends requires 4 layers, a total of 4.5 × 10^6 molecules; and configuration (c) with pentacenes on their long-ends but rotated 90 degrees compared to (b) requires 2.5 layers and a total of 4.5 × 10^6 molecules. These numbers imply that direct measurement from AFM to decide the island structure experimentally is not sufficient. With the same source, deposition rate, and exposure, the three possible configurations will give similar AFM morphologies and thin-film transistor properties.

Configuration	Force field results (eV)	DFT results (eV)
Fig. 5.2(a)	0.57	0.45
Fig. 5.2(b)	0.54	0.23
Fig. 5.2(d)	1.43	1.18

Table 5.3: Pentacene-pentacene interaction energies of three configurations in vacuum calculated with force field simulations and DFT simulations.

5.5 Reliability of the current simulation

Finally, let us compare some results from the DFT calculations with those from force field simulations. Pentacene-pentacene interaction in vacuum with configurations shown in Fig. 5.2 (a), (b), and (d). The VASP package is used for the DFT calculations. The supercells used in calculations for configurations Fig. 5.2(a) and Fig. 5.2(b) leave 10 Å vacuum in very direction around the molecules. A two dimensional periodic cell is used in calculation for configuration Fig. 5.2(d). $1 \times 1 \times 1$, $2 \times 2 \times 2$ and $3 \times 3 \times 3$ k point meshes are used in sampling the reciprocal space. In Table 5.3, converged results are listed.

The results in Table 5.3 show that the energies calculated with force field simulations are systematically larger than that with DFT simulations. This is reasonable since DFT is known to under-estimate the van der Waals interactions. Also notice that the relative magnitudes of the three energies are the same in both calculations. Furthermore, the interaction energy calculated in a 3D crystalline structure in Ref. [180] is 1.30 eV, which is larger than our 2D DFT value and reasonably close to our force field result. Overall, these results give us confidence in the reliability of the current force field simulations.

5.6   Conclusions

In conclusion, we studied the energetics and dynamics of pentacene molecules in vacuum and on three inert surfaces. We find that herringbone structure is energetically and dynamically favorable in pentacene island formation both in vacuum and on silica surfaces. From force field MD simulations and analysis, the pentacene island structures has a 90 degree rotation compared to the experimentally reported results. We analyzed in detail the key parameter ε_{ps}, the pentacene-substrate interaction energy, in detail and demonstrated how this value may effect the pentacene island and thin-film structures on inert surfaces. The reliability of the force field simulations applied in this study has also been examined. We hope this study can assist experimental results in understanding pentacene molecules on surfaces and further the performace of pentacene thin-film transistors.

5.7   Acknowledgments

Appendices

Appendix A

Notes on a tight binding calculation for $Pd(CN)_2$ planar structure

From our first-principles calculations, we plot out the band structure for $Pd(CN)_2$ sheet and, for each covalent band we find the corresponding bonding state. According to the partial charge density plots, the fourteen filled covalent bands are: 13-14, two σ bonds between C and N. 9-12, σ bonds between Pd and C, Pd and N. 8, the non-hybridized d orbital of Pd atom. 2-7, π interactions among d orbitals of Pd and p orbitals of C and N. 1, non-hybridized d orbital of Pd atom. The details can be seen in Fig. A.1.

Similar discussions on band structure of $Ni(CN)_2$ sheet have been presented in Chapter 4. Here we reproduce the results for $Pd(CN)_2$ to examine its band structure from a tight binding calculation based on the results of DFT calculations.

According to the orbitals we found that are participating in the bonding and

119
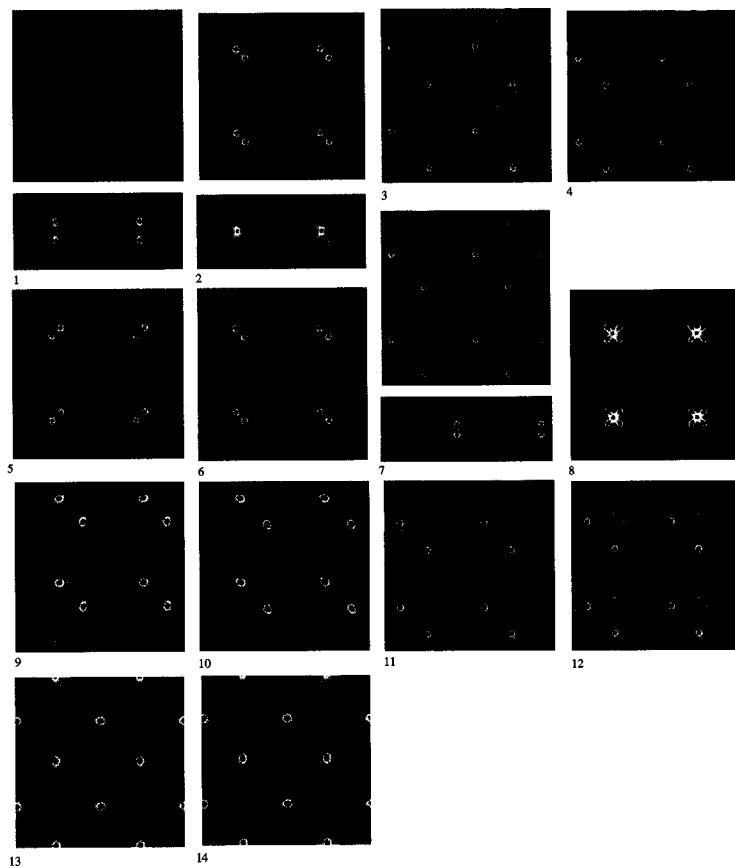
Fig. A.1: Partial charge densities of the Pd(CN)₂ sheet. From the first band below energy gap to the last, there are 14 in all.

antibonding states formation, we choose a limited number of orbitals of the Pd, C, and N atoms to represent these interactions (all other interactions are assumed to be zero) and build a tight binding model for the band structure calculations. By properly choosing reasonable values for these interactions, we find the states we choose are sufficient to describe the electronic properties of the Pd(CN)₂ sheets. The following is the notes for this tight-binding calculation.

First, the unit cell applied in tight-binding calculation is shown in Fig. A.2.

We neglect the unhybridized orbitals d_{xy} and $d_{3z^2-r^2}$ of Pd (they produce two
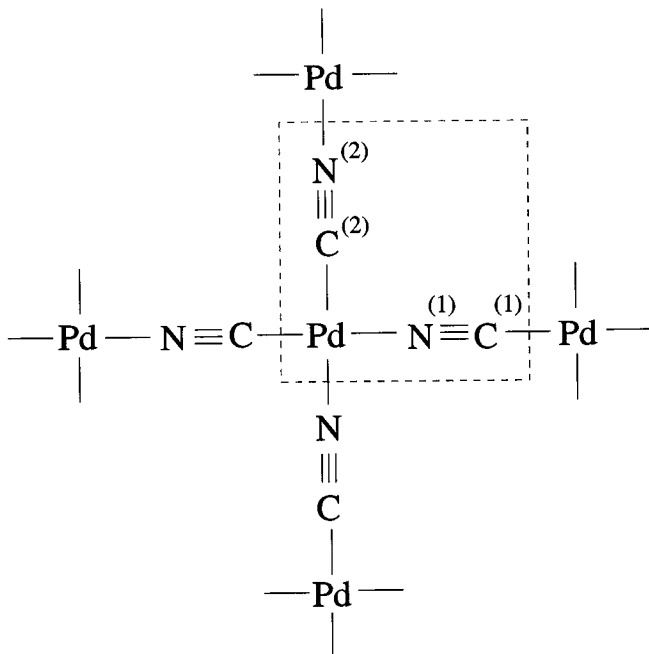
Fig. A.2: A schematic show of the two-dimensional structure of $Pd(CN)_2$ sheet. The region in the red dotted lines is the unit cell we choose for our tight binding model. There are one Pd atom, two C atoms and two N atoms in a unit cell. We label the C and N atoms along the x direction to be $C^{(1)}$ and $N^{(1)}$, and the others along the y direction to be $C^{(2)}$ and $N^{(2)}$.

nondispersed bands). The nineteen orbitals we use are shown in Table A.1. Our tight-binding wave functions are then built up using Bloch wave function basis set, which is constructed with localized atomic orbitals listed in Table A.1:

$$|\chi_1(\mathbf{r})\rangle = \sum e^{i\mathbf{k}\cdot\mathbf{R}}|d_{x^2-y^2}(\mathbf{r}+\mathbf{R})\rangle$$

$$|\chi_2(\mathbf{r})\rangle = \sum e^{i\mathbf{k}\cdot\mathbf{R}}|p_y(\mathbf{r}+\mathbf{R})\rangle_{N_1}$$

$$|\chi_3(\mathbf{r})\rangle = \sum e^{i\mathbf{k}\cdot\mathbf{R}}|p_z(\mathbf{r}+\mathbf{R})\rangle_{N_1}$$

$$|\chi_4(\mathbf{r})\rangle = \frac{1}{\sqrt{2}}\sum e^{i\mathbf{k}\cdot\mathbf{R}}|(s+p_x)(\mathbf{r}+\mathbf{R})\rangle_{N_1}$$

$$|\chi_5(\mathbf{r})\rangle \quad = \frac{1}{\sqrt{2}}\sum e^{i\mathbf{k}\cdot\mathbf{R}}|(s-p_x)(\mathbf{r}+\mathbf{R})\rangle_{N_1}$$

$$|\chi_6(\mathbf{r})\rangle \quad = \sum e^{i\mathbf{k}\cdot\mathbf{R}}|p_x(\mathbf{r}+\mathbf{R})\rangle_{N_2}$$

$$|\chi_7(\mathbf{r})\rangle \quad = \sum e^{i\mathbf{k}\cdot\mathbf{R}}|p_z(\mathbf{r}+\mathbf{R})\rangle_{N_2}$$

$$|\chi_8(\mathbf{r})\rangle \quad = \frac{1}{\sqrt{2}}\sum e^{i\mathbf{k}\cdot\mathbf{R}}|(s+p_y)(\mathbf{r}+\mathbf{R})\rangle_{N_2}$$

$$|\chi_9(\mathbf{r})\rangle \quad = \frac{1}{\sqrt{2}}\sum e^{i\mathbf{k}\cdot\mathbf{R}}|(s-p_y)(\mathbf{r}+\mathbf{R})\rangle_{N_2}$$

$$|\chi_{10}(\mathbf{r})\rangle \quad = \sum e^{i\mathbf{k}\cdot\mathbf{R}}|p_y(\mathbf{r}+\mathbf{R})\rangle_{C_1}$$

$$|\chi_{11}(\mathbf{r})\rangle \quad = \sum e^{i\mathbf{k}\cdot\mathbf{R}}|p_z(\mathbf{r}+\mathbf{R})\rangle_{C_1}$$

$$|\chi_{12}(\mathbf{r})\rangle \quad = \frac{1}{\sqrt{2}}\sum e^{i\mathbf{k}\cdot\mathbf{R}}|(s+p_x)(\mathbf{r}+\mathbf{R})\rangle_{C_1}$$

$$|\chi_{13}(\mathbf{r})\rangle \quad = \frac{1}{\sqrt{2}}\sum e^{i\mathbf{k}\cdot\mathbf{R}}|(s-p_x)(\mathbf{r}+\mathbf{R})\rangle_{C_1}$$

$$|\chi_{14}(\mathbf{r})\rangle \quad = \sum e^{i\mathbf{k}\cdot\mathbf{R}}|p_x(\mathbf{r}+\mathbf{R})\rangle_{C_2}$$

$$|\chi_{15}(\mathbf{r})\rangle \quad = \sum e^{i\mathbf{k}\cdot\mathbf{R}}|p_z(\mathbf{r}+\mathbf{R})\rangle_{C_2}$$

$$|\chi_{16}(\mathbf{r})\rangle \quad = \frac{1}{\sqrt{2}}\sum e^{i\mathbf{k}\cdot\mathbf{R}}|(s+p_y)(\mathbf{r}+\mathbf{R})\rangle_{C_2}$$

$$|\chi_{17}(\mathbf{r})\rangle \quad = \frac{1}{\sqrt{2}}\sum e^{i\mathbf{k}\cdot\mathbf{R}}|(s-p_y)(\mathbf{r}+\mathbf{R})\rangle_{C_2}$$

$$|\chi_{18}(\mathbf{r})\rangle \quad = \frac{1}{\sqrt{2}}\sum e^{i\mathbf{k}\cdot\mathbf{R}}|(d_{zx}+d_{yz})(\mathbf{r}+\mathbf{R})\rangle$$

$$|\chi_{19}(\mathbf{r})\rangle \quad = \frac{1}{\sqrt{2}}\sum e^{i\mathbf{k}\cdot\mathbf{R}}|(d_{zx}-d_{yz})(\mathbf{r}+\mathbf{R})\rangle$$

atom	orbitals
$C^{(1)}$	$s-p_x,\ s+p_x,\ p_y,\ p_z$
$C^{(2)}$	$s-p_y,\ s+p_y,\ p_x,\ p_z$
$N^{(1)}$	$s-p_x,\ s+p_x,\ p_y,\ p_z$
$N^{(2)}$	$s-p_y,\ s+p_y,\ p_x,\ p_z$
Pd	$d_{zx-yz},\ d_{zx+yz},\ d_{x^2-y^2}$

Table A.1: Orbitals used for the tight binding calculation (unnormalized).

Under the basis set $\{|\chi_1\rangle, \dots |\chi_{19}\rangle\}$, the Hamiltonian matrix elements are:

$$\langle\chi_2|\mathcal{H}|\chi_2\rangle = \langle\chi_3|\mathcal{H}|\chi_3\rangle = \langle\chi_6|\mathcal{H}|\chi_6\rangle = \langle\chi_7|\mathcal{H}|\chi_7\rangle = \epsilon_p^N$$

$$\langle\chi_{10}|\mathcal{H}|\chi_{10}\rangle = \langle\chi_{11}|\mathcal{H}|\chi_{11}\rangle = \langle\chi_{14}|\mathcal{H}|\chi_{14}\rangle = \langle\chi_{15}|\mathcal{H}|\chi_{15}\rangle = \epsilon_p^C$$

$$\langle\chi_1|\mathcal{H}|\chi_1\rangle = \epsilon_{d1}$$

$$\langle\chi_{18}|\mathcal{H}|\chi_{18}\rangle = \epsilon_{d2}$$

$$\langle\chi_{19}|\mathcal{H}|\chi_{19}\rangle = \epsilon_{d3}$$

$$\langle\chi_4|\mathcal{H}|\chi_4\rangle = \langle\chi_5|\mathcal{H}|\chi_5\rangle = \langle\chi_8|\mathcal{H}|\chi_8\rangle = \langle\chi_9|\mathcal{H}|\chi_9\rangle = \epsilon_{sp}^N$$

$$\langle\chi_{12}|\mathcal{H}|\chi_{12}\rangle = \langle\chi_{13}|\mathcal{H}|\chi_{13}\rangle = \langle\chi_{16}|\mathcal{H}|\chi_{16}\rangle = \langle\chi_{17}|\mathcal{H}|\chi_{17}\rangle = \epsilon_{sp}^C$$

$$\langle\chi_2|\mathcal{H}|\chi_{10}\rangle = \langle\chi_3|\mathcal{H}|\chi_{11}\rangle = \langle\chi_6|\mathcal{H}|\chi_{14}\rangle = \langle\chi_7|\mathcal{H}|\chi_{15}\rangle = V_\pi^{NC}$$

$$\langle\chi_4|\mathcal{H}|\chi_{13}\rangle = \langle\chi_9|\mathcal{H}|\chi_{16}\rangle = \epsilon_\sigma^{NC}$$

$$\langle\chi_5|\mathcal{H}|\chi_{12}\rangle = \langle\chi_8|\mathcal{H}|\chi_{17}\rangle = \epsilon_{int}^{NC}$$

$$\langle\chi_2|\mathcal{H}|\chi_6\rangle = e^{ik_ya}\epsilon_N^{12}$$

$$\langle\chi_{14}|\mathcal{H}|\chi_{10}\rangle = e^{ik_xa}\epsilon_C^{12}$$

$$\langle\chi_2|\mathcal{H}|\chi_{14}\rangle = \epsilon_{NC}^{12}$$

$$\langle\chi_{10}|\mathcal{H}|\chi_6\rangle = e^{-i(k_x-k_y)a}\epsilon_{NC}^{12}$$

$$\langle\chi_5|\mathcal{H}|\chi_8\rangle = e^{ik_ya}\epsilon_{N\sigma}^{12}$$

$$\langle\chi_{12}|\mathcal{H}|\chi_{17}\rangle = e^{-ik_xa}\epsilon_{C\sigma}^{12}$$

$$\langle\chi_1|\mathcal{H}|\chi_5\rangle = \epsilon_{dsn1}$$

$$\langle\chi_1|\mathcal{H}|\chi_8\rangle = e^{ik_ya}\epsilon_{dsn2}$$

$$\langle\chi_1|\mathcal{H}|\chi_{17}\rangle = \epsilon_{dsc2}$$

$$\langle\chi_1|\mathcal{H}|\chi_{12}\rangle = e^{ik_xa}\epsilon_{dsc1}$$

$$\langle\chi_{18}|\mathcal{H}|\chi_{15}\rangle = \epsilon_{d\pi2}^C$$

$$\langle \chi_{18}|\mathcal{H}|\chi_3\rangle = \epsilon_{d\pi 1}^N$$

$$\langle \chi_{18}|\mathcal{H}|\chi_{11}\rangle = e^{ik_x a}\epsilon_{d\pi 1}^C$$

$$\langle \chi_{18}|\mathcal{H}|\chi_7\rangle = e^{ik_y a}\epsilon_{d\pi 2}^N$$

Now we have a 19×19 Hamiltonian matrix. Based on the first-principles results (Fig. A.1), lots of elements in this matrix are zero. It is easy to find that to solve for the eigenvalues (energy bands) and the eigenvectors (wave functions), we can already split the original matrix into six. a is the lattice constant, which is 5.12 Åfrom DFT calculations.

Matrix one is constructed under the bases $|\chi_1\rangle$, $|\chi_5\rangle$, $|\chi_8\rangle$, $|\chi_{12}\rangle$, and $|\chi_{17}\rangle$, featuring the σ interaction between orbital $d_{x^2-y^2}$ of Pd atom with orbitals of neighboring N and C atoms.

$$\begin{pmatrix} \epsilon_{d1} & \epsilon_{dsn1} & e^{ik_y a}\epsilon_{dsn2} & e^{ik_x a}\epsilon_{dsc1} & \epsilon_{dsc2} \\ \epsilon_{dsn1} & \epsilon_{sp}^N & e^{ik_y a}\epsilon_{N\sigma}^{12} & \epsilon_{int}^{NC} & 0 \\ e^{-ik_y a}\epsilon_{dsn2} & e^{-ik_y a}\epsilon_{N\sigma}^{12} \; \epsilon_{sp}^N & \epsilon_{sp}^N & 0 & \epsilon_{int}^{NC} \\ e^{-ik_x a}\epsilon_{dsc1} & \epsilon_{int}^{NC} & 0 & \epsilon_{sp}^C & e^{-ik_x a}\epsilon_{C\sigma}^{12} \\ \epsilon_{dsc2} & 0 & \epsilon_{int}^{NC} & e^{ik_x a}\epsilon_{C\sigma}^{12} & \epsilon_{sp}^C \end{pmatrix}$$

Matrix two is constructed with the bases $|\chi_2\rangle$, $|\chi_6\rangle$, $|\chi_{10}\rangle$, $|\chi_{14}\rangle$, characterizing the Π interactions between N and C atoms.

$$\begin{pmatrix} \epsilon_p^N & e^{ik_y a}\epsilon_N^{12} & V_\pi^{NC} & \epsilon_{NC}^{12} \\ e^{-ik_y a}\epsilon_N^{12} & \epsilon_p^N & e^{i(k_x-k_y)a}\epsilon_{NC}^{12} & V_\pi^{NC} \\ V_\pi^{NC} & e^{-i(k_x-k_y)a}\epsilon_{NC}^{12} & \epsilon_p^C & e^{-ik_x a}\epsilon_C^{12} \\ \epsilon_{NC}^{12} & V_\pi^{NC} & e^{ik_x a}\epsilon_C^{12} & \epsilon_p^C \end{pmatrix}$$

Matrix three is built up with the bases $\chi_{18}\rangle$, $\chi_3\rangle$, $\chi_{11}\rangle$, and $\chi_7\rangle$, $\chi_{15}\rangle$, describing the π interactions among the d_{zx+yz} orbital of Pd and the orbitals of C and N atoms.

$$\begin{pmatrix} \epsilon_{d2} & \epsilon_{d\pi1}^N & e^{ik_x a}\epsilon_{d\pi1}^C & e^{ik_y a}\epsilon_{d\pi2}^N & \epsilon_{d\pi2}^C \\ \epsilon_{d\pi1}^N & \epsilon_p^N & V_\pi^{NC} & 0 & 0 \\ e^{ik_y a}\epsilon_{d\pi1}^C & V_\pi^{NC} & \epsilon_p^C & 0 & 0 \\ e^{-ik_y a}\epsilon_{d\pi2}^N & 0 & 0 & \epsilon_p^N & V_\pi^{NC} \\ \epsilon_{d\pi2}^C & 0 & 0 & V_\pi^{NC} & \epsilon_p^C \end{pmatrix}$$

Matrix four and five are both 2×2 and have the same matrix elements, although under two sets of bases: $\{ \chi_4, \chi_{13}\}$ and $\{ \chi_9, \chi_{16}\}$, describing the σ bond between each pair of the N and C atoms.

$$\begin{pmatrix} \epsilon_{sp}^N & \epsilon_{sp}^{NC} \\ \epsilon_{sp}^{NC} & \epsilon_{sp}^C \end{pmatrix}$$

The last matrix has only one element, which meas approximately we assume d_{zx-yz} does not interact with any other orbitals.

$$\begin{pmatrix} \epsilon_{d3} \end{pmatrix}$$

ϵ_p^N	6.157	ϵ_{d1}	37.511	ϵ_{sp}^N	-11.521	ϵ_{d2}	-6.888
ϵ_p^C	-3.843	ϵ_{dsn1}	-5.583	ϵ_{sp}^C	-11.673	$\epsilon_{d\pi1}^N$	2.186
ϵ_{NC}^{12}	0.788	ϵ_{dsn2}	5.583	ϵ_{int}^{NC}	-0.742	$\epsilon_{d\pi2}^N$	-0.915
V_π^{NC}	-7.762	ϵ_{dsc1}	4.871	$\epsilon_{N\sigma}^{12}$	-0.247	$\epsilon_{d\pi1}^C$	-0.852
ϵ_{d3}	-6.888	ϵ_{dsc2}	-4.871	$\epsilon_{N\sigma}^{12}$	-0.100	$\epsilon_{d\pi2}^C$	-0.351

Table A.2: Values of the matrix elements, in unit of eV.

With these 6 matrices, by sampling k points along high symmetry lines in k space, we can get 19 bands, 12 of which are filled and below the energy gap, 7 empty and above the energy gap. The 12 filled bands plus the other nonhybridized $d_{3z^2-r^2}$ and d_{xy} orbitals correspond to the fourteen valence bands we find from first-principles calculations.

Next we solve for the eigenvalues of all the matrices and try a best fit to the first-principles bands with carefully selected values for the interaction energies. The program Mathematica is used and the various interacting energies s are set as Table A.2.

The band structures of planar $Pd(CN)_2$ from DFT calculations and tight binding fittings are shown in Fig. A.3. On the bottom panel, ten valence bands from tight binding calculation are plotted. The neglected ones are the two N-C σ bands and the two non-dispersed bands from unhybridized d_{xy} and $d_{3z^2-r^2}$ orbitals. Comparing with the top panel results from DFT calculations, the bands are well reproduced from the nineteen orbitals we choose. Thus the interpretation of electronic states in Chapter 4, Table 4.1 is valid.
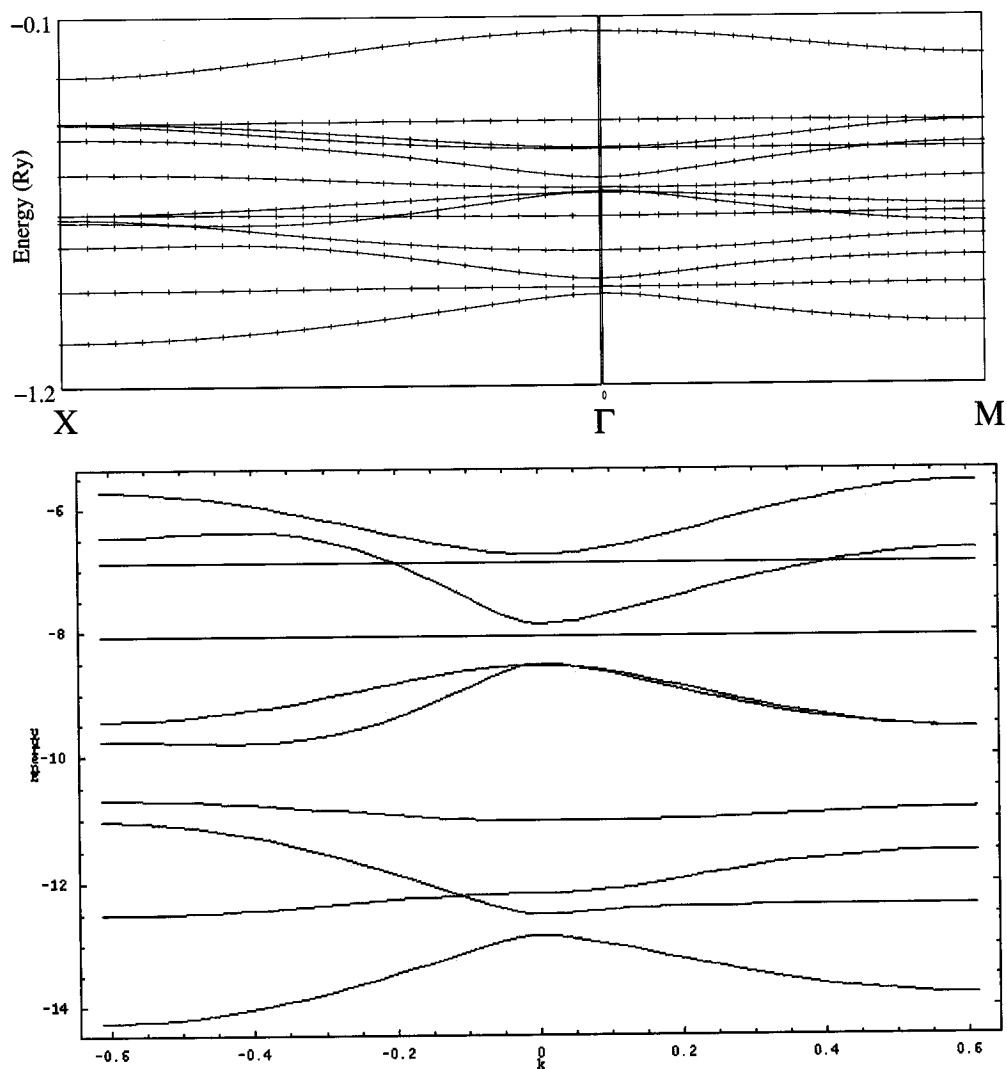
Fig. A.3: Top: band structure from first principle calculations for the $Pd(CN)_2$ sheet. Bottom: the band structure of $Pd(CN)_2$ sheet from a tight-binding calculation. Only ten valence bands are here (14 in all originally, here the last two N-C σ bands are not included, also neglected are the top two bands from the unhybridized d_{xy} and $d_{3z^2-r^2}$ orbitals.)

Appendix B

The Sn_2Se_6Pd mesostructure

Mesoporous inorganic solids (with pore diameters of 20-500 Å) have found great utility as catalysts and sorption media [182]. Mesostructured chalcogenide-based materials have been observed in experiment with long-range order and semiconducting properties [183, 184]. They can be prepared using suitable molecular building blocks, linkage metal ions and surfactant molecules. The size and arrangement of the pores are strongly dependent on the surfactant molecules. One of the well studied mesopores is composed of building blocks $[Sn_2Se_6]^{4-}$, linkage metal ion Pt^{2-} or Pd^{2-}, and has hexagonal symmetry when using the hydroxyl-functionalized surfactants. The diameter of the pores are adjustable by choosing surfactants with different sizes. The materials are semiconducting with band gaps of about 1.5 eV when Pt^{2-} is chosen as the linkage ion. Although a number of physical measurements, such as X-ray diffraction and NMR spectroscopy, have been made, knowledge of the atomic structure of these nanopores are not available yet.

In this appendix, I will present our ongoing work on exploration of the Sn_2Se_6Pd nanopore structures using DFT calculations. The stream of thoughts can be demon-

128

strated with Fig. B.1.
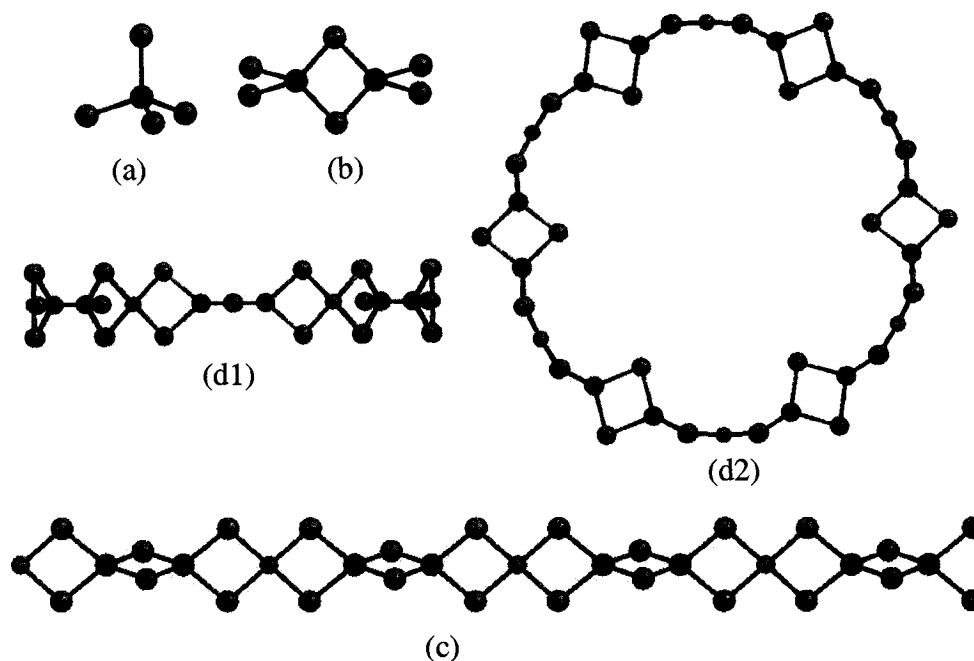
Fig. B.1: Various structures related to the Sn_2Se_6Pd nanopore. (a): the tetrahedral anion $[SnSe_4]^{4-}$; (b): the $[Sn_2Se_6]^{4-}$ anion; (c): the Sn_2Se_6Pd chain; (d1): side view of a Sn_2Se_6Pd ring; (d2): top view of a Sn_2Se_6Pd ring. The orange balls represent Se atoms, the purple balls represent Sn atoms, and the pink balls are Pd atoms.

The experiments were performed by employing $[SnSe_4]^{4-}$ as precursor, although from NMR measurement on the prepared samples found $[Sn_2Se_6]^{4-}$ building blocks. The $[SnSe_4]^{4-}$ anion has a tetrahedral structure shown in Fig. B.1(a). Under specific experimental conditions, two of such anions would undergo conversions to form a $[Sn_2Se_6]^{4-}$ anion, which is shown in Fig. B.1(b). Notice that the Se atom is located in the same column as the S atom in the periodic table and would prefer a two-fold coordination with the angle Sn-Se-Sn close to 90 degrees [33]. This would be hard to satisfy if the two Sn atoms and two Se atoms in the middle are in the same plane because of the tetrahedral angle Se-Sn-Se. Thus either one of these angles are distorted, or the four atoms are not in the same plane. From experimental

measurements, the Pt/Pd atoms are four-fold coordinated. The role it plays should resemble that in the cyanide–transition-metal sheets discussed in Chapter 4. The simple way of linking the $[Sn_2Se_6]^{4-}$ anions is to let the Pd atoms chain up 4 Se atoms, as is shown in Fig. B.1(c). To have the Pd atom work properly as a linkage, it has to be located at the center of a square to have the d orbitals interacting with the orbitals of the Se atoms, i.e., the Se-Pd-Se angle has to be 90 degrees. This cannot be satisfied simultaneously with with the Pd-Se bond length restrictions. Thus the chain structure is highly strained. Take one segment of the chain and bend it to form a ring. The side and top views of the structure are shown in Fig. B.1(d1) and (d2). If this circular structure could reasonably relieve the strain within the chain and produce a clean band gap, with slight modifications, it could make one possible nanopore structure.

DFT calculations have been performed using the VASP package. All structures are studied in vacuum. At this stage the hexagonal arrangement of the pores are not important elements to consider since the pore-pore interactions will be van der Waals type, as are in the CNT bundles and the periodic arrangement of the cyanide–transition-metal nanotubes. As is expected from the above discussion, the single chain structure (Fig. B.1(c)) is not electronically stable. There is no band gap found and some of the states near the Fermi level are partially occupied. This is due to the distortion to the atoms' preferred bonds and angles. We next performed calculations with a ring with 6 units of $[Sn_2Se_6]^{4-}$ (Fig. B.1(d2)). The diameter is about 20 Å, the size of the smallest nanopores studied in experiment. By bending the chain, the strain within is partially relieved. The structure has a clean band gap of about 0.2 eV. Considering that DFT calculations usually underestimate this value by no less than 50%, it is reasonable to believe that the band gap of this structure in

Pd-Se (Å)	2.46	Se-Pd-Se	92.42°; 87.44°
Sn-Se (Å)	2.56; 2.57; 2.59	Sn-Se-Pd	90.23°
ring diameter (Å)	20.02	Se-Sn-Se	79.47°; 97.64°; 121.51°; 110.34°
band gap (eV)	0.17	Sn-Se-Sn	82.93°; 82.80°

Table B.1: Structural and electronic properties of the $(6 \times Sn_2Se_6Pd)$ ring structure. The right half of the table shows the angles between nearest bonds within the structure.

experiment would be larger than 0.4 eV, which is close to some of the values reported from experiments. The related parameters of the relaxed ring structure is shown in Table B.1.

Notice that the Pd atoms are located very close to the center of a square and the angles between nearest bonds around the Se atom are close to 90 degrees. The Sn atoms are distorted from its original location at the center of a tetrahedron. The four Se-Sn-Se angles are different and varies from ideal tetrahedral angles. This result is consistent with the experimental measurements.

Based on the above study, future work could be done in the following aspects.

First, the question what the nanopores' atomic structure remain unanswered. From the ring structure shown in Fig. B.1(d2), there are two possible ways to build up a pore with similar diameter and electronic property. One is to stack these rings one after another along the wall direction. The nearest rings do not have to line up perfectly but can have relative rotations relative to the axis along the wall of the pore. Several basic things need to be clarified in this case: 1) what the optimal distance between the nearest rings is; 2) what the optimal relative orientations of the rings are; 3) considering together 1) and 2), how many rings it takes to complete one unit cell along the wall of the pore; 4) what the interactions between the neighboring rings are; and 5) what the electronic properties and mechanical properties of the

optimized pore structures built in this way are. The other way is to break the ring and make it an infinite helical structure (or finite with saturations at two ends). Again similar problems as 1), 2), 3), and 5) discussed above need to be solved for this design.

Second, Comparison of the two structures for the pores can be made. The stable one of two could be selected to study the hexagonal arrangement of these pores. The questions then will be 1) what the optimal inter-pore distance is; 2) how the hexagonal arrangement of the pores changes the structure of a single pore; and 3) how this arrangement changes the electronic and mechanical properties of the pores.

Once the above investigations are made, further studies of potential applications of these nanopores can be made.

Bibliography

[1] P. Hohenberg and W. Kohn, Phys. Rev. **136**, 864 (1964).

[2] M. Born and R. Oppenheimer, Annalen der Physik **84**, 457 (1927).

[3] N. W. Aschroft and N. D. Mermin, *Solid State Physics* (Holt Saunders, Philadelphia), 1976.

[4] W. Kohn and L. J. Sham, Phys. Rev. **140**, 1133A (1965).

[5] U. von Barth, in *Many Bosy Phenomena at Surfaces*, edited by D. Langreth and H. Suhl (Academic, New York), p.3 (1984).

[6] R. M. Dreizler and J. da Providencia, *Density Functional Methods in Physics* (Plenum, New York 1985).

[7] R. O. Jones and O. Gunnarsson, Rev. Mod. Phys. **61**, 689 (1989).

[8] E. S. Kryachko and E. V. Ludena, *Energy Density Functional Theory of Many Electron Systems* (Kluwer Academic, Boston 1990).

[9] M. C. Payne, M. P. Teter, D. C. Allan, T. A. Arias, and J. D. Joannopoulos, Rev. Mod. Phys. **64**, 1045 (1992).

[10] E. P. Wigner, Trans. Faraday Soc. **34**, 678 (1938).

[11] L. Hedin and B. Lundqvist, J. Phys. C **4**, 2064 (1971).

[12] S. H. Vosko, L. Wilk, and M. Nusair, Can. J. Phys. **58**, 1200 (1980).

[13] J. P. Perdew and A. Zunger, Phys. Rev. B **23**, 5048 (1981).

[14] D. R. Hamann, Phys. Rev. Lett. **42**, 662 (1979).

[15] M. T. Yin and M. L. Cohen, Phys. Rev. B **26**, 5668 (1982).

[16] J. F. Janak, Phys. Rev. B **18**, 7165 (1978).

[17] J. P. Perdew, R. G. Parr, M. Levy, and J. L. Balduz Jr., Phys. Rev. Lett. **49**, 1961.

[18] F. Gygi and A. Baldereschi, Phys. Rev. Lett. **62**, 2160 (1989).

[19] L. J. Sham and M. Schlüter, Phys. Rev. Lett. **51**, 1888 (1983).

[20] L. J. Sham and M. Schlüter, Phys. Rev. B **32**, 3883 (1985).

[21] M. Lannoo, M. Schlüter, and L. J. Sham, Phys. Rev. B **32**, 3890 (1985).

[22] M. S. Hybertsen and S. G. Louie, Phys. Rev. Lett. **55**, 1418 (1985).

[23] M. S. Hybertsen and S. G. Louie, Phys. Rev. B **34**, 5390 (1986).

[24] R. W. Godby, M. Schlüter, and L. J. Sham, Phys. Rev. Lett. **56**, 2415 (1986); Phys. Rev. B **37**, 10159 (1988).

[25] L. Fritsche, Phys. Rev. B **33**, 3976 (1986); Physica B **172**, 7 (1991).

[26] J. Cordes and L. Fritsche, Z. Phys. D **13**, 345 (1989).

[27] L. Fritsche and Y. M. Gu, Phys. Rev. B **48**, 4250 (1993).

[28] L. Fritsche, *Excited States and Electron-atom Scattering*, in *Density Functional Theory*, edited by E. K. U. Gross and R. M. Dreizler (Plenum Press, New York, 1995).

[29] I. N. Remediakis and E. Kaxiras, Phys. Rev. B **59**, 5536 (1999).

[30] J. C. Phillips, Phys. Rev. **112**, 685 (1958).

[31] M. L. Cohen and V. Heine, Solid State Physics Vol. 24, p. 37 (1970).

[32] M. T. Yin and M. L. Cohen, Phys. Rev. B **25**, 7403 (1982).

[33] E. Kaxiras, *Atomic and Electronic Structure of Solids* (Cambridge University Press, United Kindom, 2003).

[34] D. J. Chadi and M. L. Cohen, Phys. Rev. B **8**, 5747 (1973).

[35] J. D. Joannopoulos and M. L. Cohen, J. Phys. C **6**, 1572 (1973).

[36] H. J. Monkhorst and J. D. Pack, Phys. Rev. B **13**, 5188 (1976).

[37] R. A. Evarestov and V. P. Smirnov, Phys. Status Solidi **119**, 9 (1983).

[38] R. Car, M. Parrinello, M. C. Payne, J. Phys.: Condens. Matter **3**, 9539 (1991).

[39] G. Kresse and J. Hafner, Phys. Rev. B **47**, 558 (1993); **49**, 14251 (1994); G. Kresse and J. Furthmüller, Comput. Mater. Sci. **6**, 15 (1996); Phys. Rev. B **54**, 11169 (1996).

[40] J. M. Soler, E. Artacho, J. D. Gale, A. Gareía, J. Junquera, P. Ordejón, and D. Sánchez-Portal, J. Phys. Condens. Matt. **14**, 2745 (2002).

[41] X. Gonze, J.-M. Beuken, R. Caracas, F. Detraux, M. Fuchs, G.-M. Rignanese, L. Sindic, M. Verstraete, G. Zerah, F. Jollet, M. Torrent, A. Roy, M. Mikami,Ph. Ghosez, J.-Y. Raty, and D.C. Allan, Comput. Mat. Sci. **25**, 478 (2002).

[42] N. Sergueev, D. Roubtsov, and Hong Guo, Phys. Rev. Lett. **95**, 146803 (2005).

[43] R. D. King-Smith and D. Vanderbilt, Phys. Rev. B **47**, 1651 (1993).

[44] D. Vanderbilt and R. D. King-Smith, Phys. Rev. B **48**, 4442 (1993).

[45] R. Resta, Rev. Mod. Phys. **66**, 899 (1994).

[46] G. Lu, E. Tadmor, and E. Kaxiras, Phys. Rev. B **73**, 024108 (2005).

[47] G. Lu and E. Kaxiras, *Overview of multiscale simulations of materials* in *Handbook of theoretical and computational nanotechnology*, edited by M. Rieth and W. Schommers (American Scientific Publishers, 2005).

[48] C. Wu, C. H. Crouch, L. Zhao, J. E. Carey, R. Younkin, J. A. Levinson, E. Mazur, R. M. Farrel, P. Gothoskar and A. Karger, Appl. Phys. Lett. **78**, 1850 (2001).

[49] J. E. Carey and E. Mazur, manuscript in preparation.

[50] C. H. Crouch, J. E. Carey, M. Y. Shen, E. Mazur and F. Génin, submitted to Appl. Phys. A.

[51] C. H. Crouch, J. E. Carey, J. M. Warrender, M. J. Aziz and E. Mazur, manuscript in preparation.

[52] T. G. Kim, J. M. Warrender, and M. J. Aziz, Appl. Phys. Lett. **88**, 241902 (2006).

[53] J. Shen, R. Skomski, M. Klaua, H. Jenniches, S. Sundar Manoharan, and J. Kirschner, Phys. Rev. B **56**, 2340 (1997).

[54] J. Coutinho, R. Jones, P. R. Briddon and S. Öberg, Phys. Rev. B **62**, 10824 (2000).

[55] M. Pesola, J. von Boehm, T. Mattila and R. M. Nieminen, Phys. Rev. B **60**, 11449 (1999).

[56] A. B. Filonov, S. Ossicini, E. Bassani and F. A. d'Avitaya, Phys. Rev. B **65**, 195317 (2002).

[57] S. Öberg, C. P. Ewels, R. Jones, T. Hallberg, J. L. Lindström, L. I. Murin and P. R. Briddon, Phys. Rev. Lett. **81** 2930 (1998).

[58] G. Kim and J. D. Dow, Phys. Rev. B **40**, 7888 (1989).

[59] H. Overhof, M. Scheffler and C. M. Weinert, Phys. Rev. B, 12494 (1991).

[60] J. Coutinho, V. J. B. Torres, R. Jones and P. R. Briddon, Phys. Rev. B **67**, 035205 (2003).

[61] S. T. Pantelides, Phys. Rev. Lett. **57**, 2979 (1986); **58**, 1344 (1987).

[62] M. Durandurdu, D. A. Drabold and N. Mousseau, Phys. Rev. B **62**, 15307 (2000).

[63] J. Dong and D. A. Drabold, Phys. Rev. Lett. **80**, 1928 (1998).

[64] J. H. Stathis and S. T. Pantelides, Phys. Rev. B **37**,6579 (1988).

[65] D. Redfield and R. H. Bube, Phys. Rev. Lett. **65**, 464 (1990).

[66] R. Biswas, C. Z. Wang, C. T. Chan, K. M. Ho and C. M. Soukoulis, Phys. Rev. Lett. **63**, 1491 (1989).

[67] F. Valiquette and N. Mousseau, Phys. Rev. B **68**, 125209 (2003).

[68] B. Tuttle and J. B. Adams, Phys. Rev. B **57**, 12859 (1998).

[69] T. H. Her, R. J. Finlay, C. Wu, S. Deliwala and E. Mazur, Appl. Phys. Phys. Lett. **73**, 1673 (1998).

[70] A. J. Pedraza, J. D. Fowlkes and D. H. Lowndes, Appl. Phys. Lett. **74**, 2322 (1999).

[71] O. Gunnarsson and B. I. Lundqvist, Phys. Rev. B **13** 4247 (1976).

[72] J. P. Perdew, D. C. Langreth and V. Shahni, Phys. Rev. Lett. **38** 1030 (1977).

[73] D. Vanderbilt, Phys. Rev. B **41**, 7892 (1990); A. Pasquarello, K. Laasonen, R. Car, C. Lee and D. Vanderbilt, Phys. Rev. Lett. **69**, 1982 (1992); K. Lassonen, A. Pasquarello, R. Car, C. Lee and D. Vanderbilt,Phys. Rev. B **47**, 10142 (1993); G. Kresse and J. Hafner, J. Phys. Condens. Matter **6**, 8245 (1994).

[74] I. Stich, R. Car and M. Parrinello, Phys. Rev. B **44**, 11092 (1991).

[75] H. Balamane, T. Halicioglu and W. A. Tiller, Phys. Rev. B **46**, 2250 (1992) and references therein.

[76] W. D. Luedtke and U. Landman, Phys. Rev. B **37**, 4656 (1988).

[77] W. D. Luedtke and U. Landman, Phys. Rev. B **40**, 1164 (1989).

[78] F. H. Stillinger and T. A. Weber, Phys. Rev. B **31**, 5262 (1985).

[79] M. Ishimaru, Shinji and T. Motooka, Phys. Rev. B **56**, 15133 (1997).

[80] J. Tersoff, Phys. Rev. B **38**, 9902 (1988); *ibid* **39**, 5566 (1989).

[81] F. Wooden, K. Winer and D. Weaire, Phys. Rev. Lett. **54**, 1392 (1985).

[82] F. Wooten and D. Weaire, Solid State Physics **40**, 1 (1987); B. R. Djordjević, M. F. Thorpe and F. Wooden, Phys. Rev. B **52**, 5685 (1995); G. T. Barkema and N. Mousseau, Phys. Rev. B **62**, 4985 (2000).

[83] J. Fortner and J. S. Lannin, Phys. Rev. B **39**,5527 (1989).

[84] S. Kugler, G. Molnár, G. Petö, E. Zsoldos, L. Rosta, A. Menelle and R. Bellissent, Phys. Rev. B **40**, 8030 (1989).

[85] W. A. Kamitakahara, H. R. Shank, J. F. McClelland, U. Buchenau, F. Compf and L. Pintschovons, Phys. Rev. Lett. **52**, 644 (1984).

[86] M. Z. Bazant, E. Kaxiras and J. F. Justo, Phys. Rev. B **56**, 8542 (1997); M. Z. Bazant and E. Kaxiras, Phys. Rev. Lett. **77**, 4370 (1996); M. Z. Bazant and E. Kaxiras, Mater. Res. Soc. Symp. Proc. **408**, 79 (1996).

[87] J. F. Justo, M. Z. Bazant, E. Kaxiras, V. V. Bulatov and S. Yip, Phys. Rev. B **58**, 2539 (1998); M. Z. Bazant, E. Kaxiras and J. F. Justo, Mat. Res. Soc. Symp. Proc. **491**, 339 (1998).

[88] L. Brambilla, L. Colombo, V. Rosato and F. Cleri, Appl. Phys. Lett. **77**, 2337 (2000).

[89] P. Keblinski, M. Z. Bazant, R. K. Dash and M. M. Treacy, Phys. Rev. B **66**, 064104 (2002).

[90] C. L. Allred, M. Z. Bazant and L. Hobbs (unpublished).

[91] M. O. Thompson, J. W. Mayer, A. G. Cullis, H. C. Weber, N. G. Chew, J. M. Poate and D. C. Jackson, Phys. Rev. Lett. **50**, 896 (1983); A. G. Cullis, N. G. Chew, H. C. Weber and D. J. Smith, J. Cryst. Growth **68**, 624 (1984).

[92] S. Roorda, W. C. Sinke, J. M. Poate, D. C. Jacobson, S. Dierker, B. S. Dennis, D. J. Eaglesham, F. Spaepen and P. Fuoss, Phys. Rev. B **44**, 3702 (1991).

[93] N. Fukata, A. Kasuya and M. Suezawa, Physca. B **308**, 1125 (2001).

[94] R. A. Street, Phys. Rev. Lett. **49**, 1187 (1982).

[95] S. Roorda and W. C. Sinke, Phys. Rev. B **44**, 3702 (1991).

[96] P. Segovia, D. Purdie, M. Hengsberger, and Y. Baer, Nature **402**, 504 (1999).

[97] R. Losio *et al.*, Phys. Rev. Lett. **86**, 4632 (2001).

[98] H. Ishil *et al.*, Nature **426**, 540 (2003).

[99] F. J. Himpsel, J. E. Ortega, G. J. Mankey, and R. F. Willis, Advances in Phys. **47**, 511 (1998).

[100] J.-L. Lin *et al.*, Appl. Phys. Lett. **78**, 829 (2001).

[101] J. R. Ahn, H. W. Yeom, E. S. Cho, and C. Y. Park, Phys. Rev. B **69**, 233311 (2004).

[102] Z. Gai, G. A. Farnan, J. P. Pierce, and J. Shen, Appl. Phys. Lett. **81**, 742 (2002).

[103] V. Repain, J. M. Berroir, S. Rousset, and J. Lecoeur, Surf. Sci. **447**, L152 (2000).

[104] P. Gambardella, M. Blanc, L. Bürgi, K. Kuhnke, and K. Kern, Surf. Sci. **449**, 93 (2000).

[105] H. J. Elmers *et al.*, Phys. Rev. Lett. **73**, 898 (1994).

[106] J. Figuera *et al.*, Appl. Phys. Lett. **66**, 1006 (1995).

[107] D. Spišák and J. Hafner, Phys. Rev. B **65**, 235405 (2002).

[108] D. Spišák and J. Hafner, Phys. Rev. B **67**, 134434 (2003).

[109] M. Eisenbach, B. L. Györffy, G. M. Stocks, and B. Újfalussy, Phy. Rev. B **65**, 144424 (2002).

[110] J. P. Perdew and Y. Wang, Phys. Rev. B **45**, 13244 (1992).

[111] H. Jonsson, G. Mills, and K. W. Jacobsen, in *Classical and Quantum Dynamics in Condensed Phase Simulations*, edited by B. J. Berne, G. Ciccotti, and D. F. Coker (World Scientific Singapore, 1998).

[112] D. C. Schlößer, L. K. Verheij, G. Rosenfeld, and G. Comsa, Phys. Rev. Lett. **82**, 3843 (1999).

[113] Private correspondence with J. Shen.

[114] R. Stumpf and M. Scheffler, Phys. Rev. B **53**, 4958 (1996).

[115] Z. Zhang, X. Chen, and M. G. Lagally, Phys. Rev. Lett. **73**, 1829 (1994).

[116] P. E. Blöchl, Phys. Rev. B **50**, 17953 (1994); G. Kresse and D. Joubert, *ibid.* **59**,1758 (1999).

[117] J. N. Crain, J. L. McChesney, Fan Zheng, M. C. Gallagher, P. C. Snijders, M. Bissen, C. Gundelach, S. C. Erwin, and F. J. Himpsel, Phys. Rev. B **69**, 125401 (2004).

[118] J. R. Ahn, H. W. Yeom, E. S. Cho, and C. Y. Park, Phys. Rev. B **69**, 233311 (2004).

[119] H. W. Yeom, S. Takeda, E. Rotenberg, I. Matsuda, K. Horikoshi, J. Schaefer, C. M. Lee, S. D. Kevan, T. Ohta, T. Nagao, and S. Hasegawa, Phys. Rev. Lett. **82**, 4898 (1999).

[120] J. Guo, G. Lee, and E. W. Plummer, Phys. Rev. Lett. **95**, 046102 (2005).

[121] C. González, P. C. Snijders, J. Ortega, R. Pérez, F. Flores, S. Rogge, and H. H. Weitering, Phys. Rev. Lett. **93**, 126106 (2004).

[122] P. Gambardella, A. Dallmeyer, K. Maiti, M. C. Malagoli, W. Eberhardt, K. Kern, and C. Carbone, Nature **416**, 301 (2002).

[123] J. de la Figuera, M. A. Huerta-Garnica, J. E. Prieto, C. Ocal, and R. Miranda, Appl. Phys. Lett. **66**, 1006 (1995).

[124] J. Shen, M. Klaua, P. Ohresser, H. Jenniches, J. Barthel, Ch. V. Mohan, and J. Kirschner, Phys. Rev. B **56**, 11134 (1997).

[125] M. Eisenbach, B. L. Györffy, G. M. Stocks, and B. Újfalussy, Phys. Rev. B **65**, 144424 (2002).

[126] B. Lazarovits, L. Szunyogh, P. Weinberger, and B. Újfalussy, Phys. Rev. B **68**, 024433 (2003).

[127] Y. Mo, K. Varga, E. Kaxiras, and Z. Zhang, Phys. Rev. Lett. **94**, 155503 (2005).

[128] Step edges of metal surface normally appear ragged at relatively high temperatures in STM due to the active kink motions. For detail discussions, see for example, L. Kuipers, M. S. Hoogeman, and J. W. M. Frenken, Phys. Rev. B **52**, 11387 (1995).

[129] A. Biedermann, R. Tscheliessnig, M. Schmid, and P. Varga, Appl. Phys. A **78**, 807 (2004).

[130] The height of the protrusion in STM image depends on the tip conditions. We varied the tip bias and feedback current in broad ranges and found that the protrusion height falls in the range of ~0.2 - 0.5 Å.

[131] J. Tersoff, and D. R. Hamann, Phys. Rev. Lett. **50** 1998 (1983); J. Tersoff, and D. R. Hamann, Phys. Rev. B **31**, 805 (1985).

[132] A. K. Schmid, D. Atlan, H. Itoh, B. Heinrich, T. Ichinokawa, and J. Kirschner, Phys. Rev. B **48**, 2855 (1993).

[133] J. Shen, J. Giergiel, A. K. Schmid, and J. Kirschner, Surf. Sci. **328**, 32 (1995).

[134] K. E. Johnson, D. D. Chambliss, R. J. Wilson, and S. Chiang, J. Vac. Sci. Technol. A **11**, 1654 (1993).

[135] Z. Zhang, and M. G. Lagally, Science **276**, 377 (1997).

[136] H. Brune, Sur. Sci. Rep. **31**, 121 (1998).

[137] O. Pietzsch, A. Kubetzka, M. Bode, and R. Wiesendanger, Phys. Rev. Letts. **92**, 057202 (2004).

[138] R. L. Schwoebel and E. J. Shipsey, J. Appl. Phys. **37**, 3682 (1966).

[139] G. Ehrlich and F. G. Hudda, J. Chem. Phys. **44**, 1039 (1966).

[140] J.W. Evans, P.A. Thiel, M.C. Bartelt, Surf. Sci. Reports **61**, 1 (2006).

[141] J. W. Evans, D. E. Sanders, P. A. Thiel, and A. E. DePristo, Phys. Rev. B **41**, 5310 (1990).

[142] M. Villarba, and H. Jónsson, Phys. Rev. B **49**, 2208 (1994).

[143] J. Guo, Y. Mo, E. Kaxiras, Z. Zhang, and H. Weitering, Phys. Rev. B.

[144] The plane wave expansions are determined by the default energy cutoffs. The slabs used contain six layers and a total of 96 Cu or Pd atoms in the periodic supercell, separated by a vacuum region equivalent to 11.5 Å. The bottom three layers are fixed at their respective bulk positions during the relaxation.

Optimized atomic geometries are achieved when forces on all the unconstrained atoms are smaller in magnitude than 0.01 eV/Å. A 2×2×1 mesh in the Brillouin Zone of the supercell is used to sample the reciprocal space. We checked convergence by repeating the calculations for Fe adatoms on the stepped Cu(111) surfaces with a nine-layer slab and a 3 × 3 × 1 reciprocal space mesh; the results are well converged already in the six-layer slab calculations.

[145] J. Friedel, Nuovo Cimento, Suppl. **7**, 287 (1958).

[146] M. Schroeder, P. Smilauer, and D. E. Wolf, Phy. Rev. B **55**, 10814 (1997).

[147] A. U. Nilekar, J. Greeley, and M. Marvrikakis, Angrew. Chem. Int. Ed. **45**, 7046 (2006).

[148] S. Iijima, *Nature* **1991**, *354*, 56 - 58; S. Iijima and T. Ichihashi, *ibid.* **1993**, *363*, 603 - 605.

[149] D. H. Cobden, M. Bockrath, P. L. McEuen, A. G. Rinzler, R. E. Smalley, *Phys. Rev. Lett.* **1998**, *81*, 681 - 684.

[150] S. Frank, P. Poncharal, Z. L. Wang, W. A. de Heer, *Science* **1998**, *280*, 1744 - 1746.

[151] A. Rubio, J. L. Corkill, and M. L. Cohen, *Phys. Rev. B* **1994**, *49*, 5081 - 5084.

[152] N. G. Chopra, R. J. Luyken, K. Cherrey, V. H. Crespi, M. L. Cohen, S. G. Louie, and A. Zettl, *Science* **1995**, *269*, 966 - 967.

[153] N. A. W. Holzwarth, G. E. Matthews, A. R. Tackett, and R. B. Dunning, *Phys. Rev. B* **1998** *57*, 11827 - 11830.

[154] J. P. Perdew, K. Burke, and M. Ernzerhof, *Phys. Rev. Lett.* **1996** *77*, 3865 - 3868; J. P. Perdew, K. Burke, and M. Ernzerhof, *ibid.* **1997**, *78*, 1396 - 1399.

[155] The default plane-wave cutoffs for the different elements are adopted. Gaussian smearing is applied to the electronic states near the Fermi level, with a width of 0.2 eV. Optimized atomic geometries are achieved when the forces on all unconstrained atoms are smaller in magnitude than 0.01 eV/Å. A mesh in reciprocal space of 8 × 8 × 1 k-points is used for sampling in the planar structure I, and commensurate meshes for the tube structures.

[156] L. Pauling, *The Nature of the Chemical Bond* (Cornell University Press, Ithaca, NY, 1960), page 170.

[157] K. A. Hoffmann, and F. Küspert, *Z. anorg. Chem.* **1897**, *15*, 204.

[158] J. H. Rayner, and H. M. Powell, *J. Chem. Soc.* **1952**, 319; *J. Chem. Soc* **1958**, 3412.

[159] G. Seifert, H. Terrones, M. Terrones, G. Jungnickel, and T. Frauenheim, *Phys. Rev. Lett.* **2000**, *85*, 146-149.

[160] J. P. Lu, *Phys. Rev. Lett.* **1997**, *79*, 1297 - 1300.

[161] E. Hernández, C. Goze, P. Bernier, and A. Rubio, *Phys. Rev. Lett.* **1998**, *80*, 4502 -4505.

[162] D. Sánchez-Portal, E. Artacho, J. M. Soler, A. Rubio, and P. Ordejón, *Phys. Rev. B* **1999**, *59*, 12678 - 12688.

[163] M. M. J. Treacy, T. W. Ebbesen, and J. M. Gibson, *Nature* **1996**, *381*, 678 - 680.

[164] A. Krishnan, E. Dujardin, T. W. Ebbesen, P. N. Yianilos, and M. M. J. Treacy, *Phys. Rev. B* **1998**, *58*, 14013 - 14019.

[165] J.-P. Salvetat, G. A. D. Briggs, J.-M. Bonard, R. R. Bacsa, A. J. Kulik, T. Stöcklin, N. A. Burnham, and L. Forró, *Phys. Rev. Lett.* **1999**, *82*, 944 - 947.

[166] N. G. Chopra and A. Zettl, *Solid State Commun.* **1998**, *105*, 297 - 300.

[167] B. Akdim, R. Pachter, X. Duan, and W. W. Adams, *Phys. Rev. B* **2003**, *67*, 245404.

[168] M. Yu, B. S. Files, S. Arepalli, and R. S. Ruoff, *Phys. Rev. Lett.* **2000**, *84*, 5552 - 5555.

[169] M. Yu, O. Luorie, M. J. Dyer, K. Moloni, T. F. Kelly, and R. S. Rouff, *Science* **2000**, *287*, 637 - 640.

[170] I. Kaplan-Ashiri *et. al.*, *Proceedings of National Academy of Sciences* **2006**, *103*, 523 - 528.

[171] S. F. Nelson, Y.-Y Lin, D. J. Gundlach, and T. N. Jackson, Appl. Phys. Lett. **84**, 296 (2004).

[172] C. D. Dimitrakopoulos and D. J. Mascaro, IBM J. Res. Dev. **45**, 11 (2001).

[173] F.-J. M. z. Heringdort, M. C. Reuter, and R. M. Tromp, Nature **412**, 517 (2001).

[174] N. J. Watkins, and Y. Gao, J. Appl. Phys. **94**, 5782 (2003).

[175] R. Ruitz, B. Nickel, N. Koch, L. C. Feldman, R. F. Haglund, A. Kahn, and G. Scoles, Phys. Rev. B **67**, 125406 (2003).

[176] S. Pratontep, and M. Brinkmann, Phys. Rev. B **69**, 165201 (2004).

[177] S. Pratontep, F. Nüesch, L. Zuppiroli, and M. Brinkmann, Phys. Rev. B **72**, 085211 (2005).

[178] R. B. Campbell, J. M. Robertson, and J. Trotter, Acta Cryst. **14**, 705 (1961).

[179] S. E. Fritz, S. M. Martin, C. D. Frisbie, M. D. Ward, and M. F. Toney, J. Am. Chem. Soc. **126**, 4084 (2004).

[180] J. E. Northrup, M. L. Tiago, and S. G. Louie, Phys. Rev. B **66**, 121404 (2002).

[181] S. Verlaak, S. Steudel, P. Heremans, D. Janssen, and M. S. Deleuze, Phys. Rev. B **68**, 195409 (2003).

[182] C. T. Kresge, M. E. Leonowicz, W. J. Roth, J. C. Vartuli, and J. S. Beck, Nature **359**, 710 (1992).

[183] K. K. Rangan, P. N. Trikalitis, C. Canlas, T. Bakas, D. P. Weliky, and M. G. Kanatzidis, Nano Lett. **2**, 513 (2002).

[184] P. N. Trikalitis, T. Bakas, and M. G. Kanatzidis, J. Am. Chem. Soc. **127**, 3910 (2005).